Studies in rotating convection

by

Antonio M. Rubio

A Dissertation Presented in Partial Fulfillment
of the Requirements for the Degree
Doctor of Philosophy

ARIZONA STATE UNIVERSITY

August 2009

Studies in rotating convection

by

Antonio M. Rubio

has been approved

July 2009

Graduate Supervisory Committee:

J.M. Lopez, Chair
F. Marques
H.J.S. Fernando
W.B. Tang
M. Herrmann

ACCEPTED BY THE GRADUATE COLLEGE

I dedicate this work to my mother and father, who have always supported me in everything I've done.

TABLE OF CONTENTS

LIST OF FIGURES

Chapter 1

Introduction

In this thesis the problem of thermal convection in a thin fluid layer driven by maintained differential thermal boundary conditions at the top and bottom of the layer is considered. The colder fluid at the top contracts and is more dense than the warmer, expanding fluid at the bottom. Thus, with imbalanced buoyant forces acting on the fluid layer, at some critical temperature difference the unbalanced gravitational acceleration overcomes viscous drag and fluid motion is observed as the cold fluid at the top falls and the warm fluid at the bottom rises. When the fluid layer is subject to rotation a host of complications arise due to the addition of the Coriolis and centrifugal forces to the existing balance between gravitational buoyancy and viscous drag. How these competing forces find a dynamical balance over different regimes of parameter space is a matter of much importance. Major astrophysical and geophysical applications include turbulent motions in the convective layers of the Sun (Zurbuchen, 2007) and gaseous giant planets (Ingersoll & Pollard, 1982), deep ocean convection (Rhines, 1986) as well as engineering applications too numerous to list. Each of these fluid problems requires additional considerations ranging from compressibility, magnetic fields and ionization effects for solar convection to complex boundary conditions and the presence of a density changing scalar in the case of deep ocean convection. However, all these flows share the fundamental feature of rotating convection.

In addition to the above applications there has been much interest in exploring rotating convection as a pattern-forming system. Convection has long been a workhorse for problems in pattern formation and is perhaps the most studied such system. Rotating convection has the interesting property of being non-variational

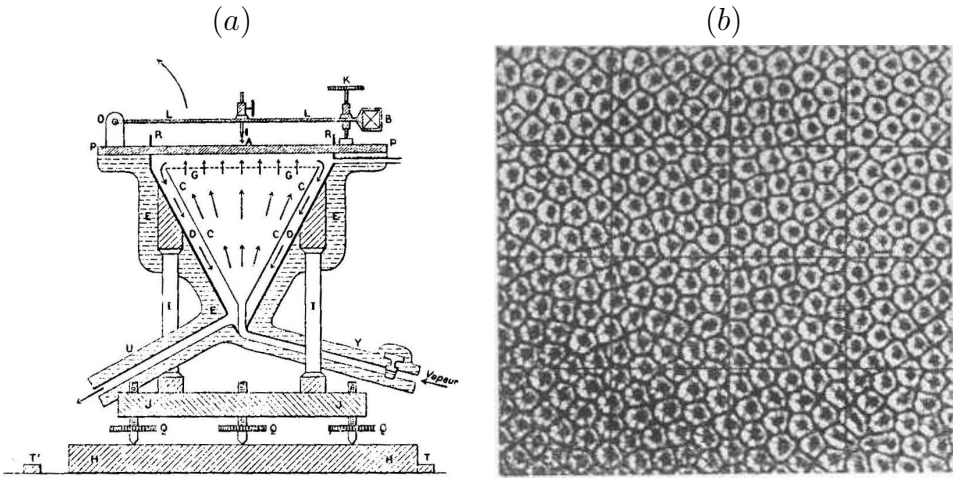

Figure 1.1: (a) Apparatus used by Bénard. (b) Snapshot of hexagonal cells. Both after Bénard (1900).

(i.e. it can not be described as a potential form) at onset with the implication that complicated behaviors can be observed directly at the onset of convection as opposed to the purely relaxational dynamics seen at the onset of convection without rotation. Chief among these complicated behaviors is the development of Küppers-Lortz-like spatio-temporal chaos which is described in detail in chapter 5 of this thesis.

Early work on Rayleigh-Bénard convection

The first systematic exploration of convective motion in a fluid layer was conducted by Bénard (1900, 1901). He studied a roughly 1 mm thick layer of whale spermaceti heated from below by steam from boiling water and cooled above by the ambient air. The apparatus used is shown in figure 1.1(a). After a period of adjustment he observed a steady array of polygons, shown in figure 1.1(b). While only later would it be realized that the effect of surface tension would be crucial to these hexagonal cells Bénards careful studies foreshadowed many features that would be confirmed in later theoretical analysis particularly in relating how cell size varied with tempera-

ture applied and the discovery of a minimum cell size. The first theoretical treatment was conducted by Lord Rayleigh (1916) in which he considered the growth rates of perturbations of the form of 2D rolls in a horizontally infinite layer of quiescent fluid. He explored the mathematically straight-forward but experimentally difficult case of stress-free boundaries at the top and bottom. He used Boussinesq's approximation, that all fluid properties remain the same except for a linear variation of density with respect to temperature in the buoyancy terms, to render the problem essentially incompressible. His linear stability analysis, which found the critical thermal driving for each wavelength of 2D rolls to achieve marginal stability, set the path for a number of further analyses (Jeffreys, 1926, 1928; Low, 1929; Pellew & Southwell, 1940) well-summarized in chapter one of Chandrasekhar (1961). Later these theoretical results would be confirmed experimentally by Schmidt & Milverton (1935) who took measurements of the variation of heat transport through the fluid layer with changing thermal driving to estimate the onset of convection in good agreement with the theoretical estimates of the same.

The Taylor-Proudman theorem

In rotating fluids a number of strange phenomena arise that are not seen in the non-rotating case (e.g. circularly polarized waves, secondary motions driven by viscous boundary layers). The most interesting and important of these is a tendency of fluid in almost rigid rotation to be vertically unchanging in nature is explained by the Taylor-Proudman theorem (Proudman, 1916; Taylor, 1917, 1922, 1923). For an incompressible fluid, with viscosity ν, rotating at a dimensional rotation rate ω and with a characteristic length scale L, if $\omega L^2/\nu$ is large then the incompressible Navier-Stokes equations in the rotating reference frame can be well-approximated by

$$\nabla P = -2\omega \times \mathbf{v}, \nabla \cdot \mathbf{v} = 0, \tag{1.1}$$

where P is the pressure and $\mathbf{v}$ is the velocity. Using a Cartesian coordinate frame this equation can be written in terms of the individual velocity components as,

$$\partial_x P = 2\omega v, \partial_y P = -2\omega u, \partial_z P = 0. \tag{1.2}$$

Differentiating the equations for the horizontal velocity in the vertical direction, z, and using the fact that $\partial_z P = 0$ the following equations are obtained,

$$\partial_x u = \partial_y v = 0. \tag{1.3}$$

Since the fluid is incompressible it must be that $\partial_z w = 0$ as well. With all three velocity components invariant in the $z-$direction the striking result that motion in the interior of a rapidly rotating fluid must be two-dimensional is obtained.

Recent developments in Rayleigh-Bénard convection with and without rotation

Rotating convection was first treated theoretically by Chandrasekhar, who devoted the third chapter of his book to the phenomena (Chandrasekhar, 1961), in which he extended Rayleigh's analysis to the rotating case. He considered a laterally infinite layer rotating at a constant rate, including the Coriolis force but neglecting centrifugal acceleration due to buoyancy differences. This is a necessary simplification when considering an infinite layer as centrifugal force distinguishes the axis of rotation and varies radially, preventing the use of harmonic functions in the lateral directions. In convection without rotation additional viscosity has the effect of increasing the stability of fluid layer to larger adverse temperature differences. Chandrasekhar found that when rotation is introduced viscosity plays an inverted role and decreasing viscosity acts to stabilize the fluid layer due to the Taylor-Proudman effect described above. A further result of the linear stability anaylsis is an increase in the wave number of convective features at onset with increasing rates of rotation.

Rossby conducted a thorough experimental study of the onset of convection with and without rotation (Rossby, 1969), in good agreement with Chandrasekhar's linear stability analysis at lower rotation rates. At higher rotation rates he noted the onset of weak convection at much lower thermal driving than that given by the linear stability estimate. This is due to an important difference in the nature of convection with and without rotation. For laboratory experiments without rotation the sidewalls of the convective cell play little role in the onset of convection aside from selecting the pattern. In rotating convection the viscous layer at the sidewall avoids the rotationally-induced stabilization owing to the Proudman-Taylor effect and for fast enough rotation the fluid layer is susceptible to instability at the sidewall for thermal driving much less than that required for convection throughout the bulk of the fluid. This premature onset of convection due to wall-localized convection corresponds to the so-called wall-modes described theoretically and numerically by Goldstein *et al.* (1993) and experimentally by Zhong *et al.* (1991).

At the same time as Rossby was carrying out his experiments two German researchers considered the stability of patterns of infinite straight rolls in rotating convection against similar rolls oriented at different angles (Küppers & Lortz, 1969). The found that for a sufficiently large rotation rate, depending on the ratio of kinematic viscosity to thermal diffusivity of the fluid, any pattern of straight rolls was unstable to another set of rolls oriented at roughly a 59 degree angle. They conjectured that above that critical rotation rate the onset of convection must necessarily be time-dependent. A number of laboratory studies confirmed that the onset of convection is indeed time-dependent (Heikes & Busse, 1980*b*; Niemela & Donnelly, 1986) although the mechanism for time-dependence is different than that put forth by Küppers and Lortz. Instead of straight roll patterns fading in amplitude to be replaced by a new set of differently oriented rolls the time-dependence emerges as a type of domain

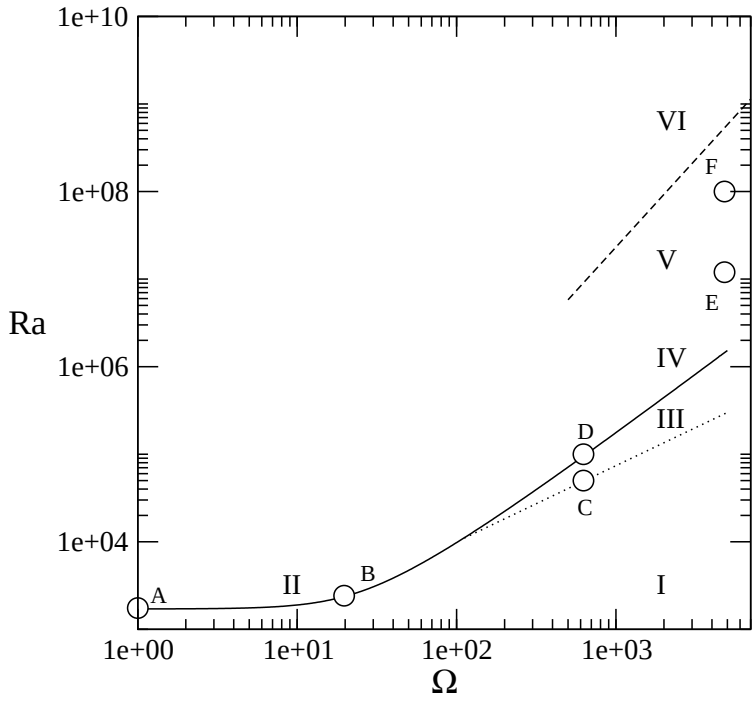

Figure 1.2: Regime diagram for rotating Rayleigh-Bénard convection. Chandrasekhar's estimate for the onset of convection is given by the solid line, the onset of wall-localized convection is shown as a dotted line following Rossby (1969), $\sqrt{Ra/\sigma Ta} = 1$ for $\sigma = 5.81$ is shown as a dashed line. The labeled circles correspond to states shown in figure 1.3. The symbol labeled with an A was translated to the right by one.

chaos in which patches of rolls are overtaken by gliding defects propogating from the sidewalls (Hu *et al.*, 1997).

Parameter regimes in rotating convection

For rotating convection in a finite cylinder there are five independent non-dimensional parameters:

Rayleigh number:	$Ra = \alpha g d^3 \Delta T / \kappa\nu$,
Coriolis number:	$\Omega = \omega d^2/\nu$,
Prandtl number:	$\sigma = \nu/\kappa$,
aspect ratio:	$\gamma = r_0/d$,
Froude number:	$Fr = \omega^2 r_0/g$,

where α is the coefficient of volume expansion, κ is the thermal diffusivity, g is the acceleration due to gravity, d is the depth of the fluid layer and r_0 is the radius of the cylinder.

Figure 1.2 shows an overview of parameter space in terms of Ra and Ω. In the region marked I there is insufficient thermal driving for convective fluid movement. When $Fr = 0$ this region is characterized by a quiscent fluid layer, when $Fr > 0$ a weak large scale meridional overturning is observed. Region II corresponds to bulk convection immediately at onset. When $\Omega = 0$ onset is to steady patterns of rolls confined by the geometry of the container. Figure 1.3(a) shows an example of such a pattern in a container with $\gamma = 11.8$. For Ω greater than about 14 spatial temporal chaos in the guise of Küppers-Lortz-like domain chaos is observed directly at the onset of bulk convection, an example of which is shown as figure 1.3(b) with $\gamma = 11.8$. For $\Omega > 0$ but smaller than 14 there exist slowly rotating fixed s-shaped patterns of rolls at onset. In region III the onset of convection is to wall-localized convection, the so-called wall modes of Goldstein *et al.* (1993) and Zhong *et al.* (1991), shown as figure 1.3(c). Region IV corresponds to coexisting wall and bulk modes, an

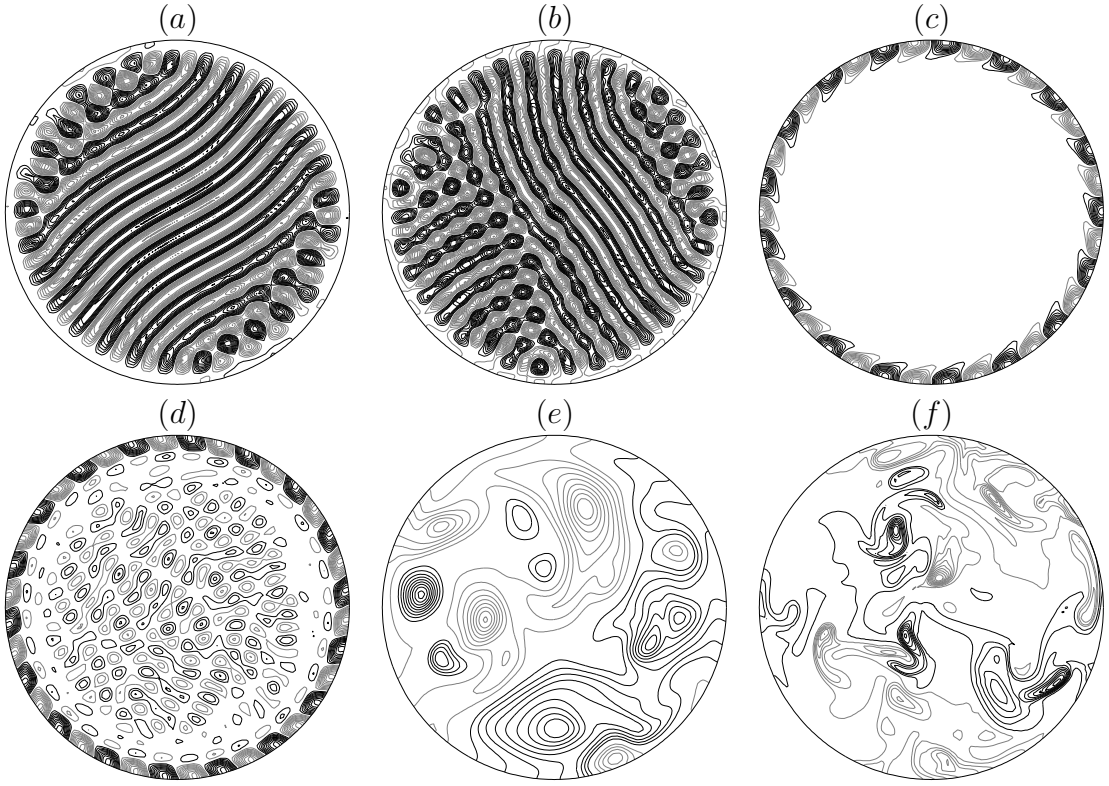

Figure 1.3: Isotherms at mid-height of the cylinder for a variety of cases. (a): Steady Rayleigh-Bénard convection without rotation, $Ra = 1750$, $\Omega = 0$, $\sigma = 4.5$, $\gamma = 11.8$, $Fr = 0$. (b): Küppers-Lortz-like dynamics at $Ra = 2420$, $\Omega = 19.7$, $\sigma = 4.5$, $\gamma = 11.8$, $Fr = 8.82 \times 10^{-3}$. (c): Pure wall mode at $Ra = 5 \times 10^4$, $\Omega = 625$, $\sigma = 7$, $\gamma = 4$, $Fr = 0$. (d): Mixed wall and bulk modes at $Ra = 1 \times 10^5$, $\Omega = 625$, $\sigma = 7$, $\gamma = 4$, $Fr = 0$. (e): Plume dominated convection at $Ra = 1.2 \times 10^7$, $\Omega = 4800$, $\sigma = 5.81$, $\gamma = 0.5$, $Fr = 0$. (f): Quasi-geostropic turbulence at $Ra = 1 \times 10^8$, $\Omega = 4800$, $\sigma = 5.81$, $\gamma = 0.5$, $Fr = 0$.

example of which is shown as figure 1.3(d). Coherent plume structures are observed in region V (figure 1.3(e)) and in region VI thermal turbulence not dissimilar from the non-rotating case is observed. Between these two regions are states described by Boubnov & Golitsyn (1995) as irregular quasi-geostrophic turbulence which are observed when $Ro = \sqrt{Ra/(\sigma 4\Omega^2)} \sim 1$, or when the acceleration due to buoyancy is roughly balanced by that of the Coriolis force, an example of which is shown as figure 1.3(f).

Thesis plan

The remainder of the thesis is structured as follows. The governing equations, symmetries and numerical method are described in chapter 2. The numerical scheme is a pseudo-spectral Fourier-Galerkin method with a 2nd order predictor-corrector temporal scheme using an improved pressure predictor which is used to project the predicted velocity field into a divergence-free space. In chapter 3 we discuss the bifurcation scenario that results in inwardly travelling waves in convection with modulation rotation in a parameter regime for which spatio-temporal complexity is observed directly at the onset of convection. The material in chapter 3 is published as Rubio *et al.* (2008). Chapter 4 continues the exploration of convection subject to modulated rotation but with a much higher background rotation for which the onset of convection is to a wall-mode. Here the effects of different modulation frequencies are considered and the quenching of wall-localised convection is described in terms of a nonlinear interaction between convection and the oscillatory boundary layers that result from modulating the rotation rate. This work as published as Rubio *et al.* (2009a). Chapter 5 concerns the development of spatio-temporal complexity at onset in rotating convection, laying out two different scenarios depending on whether or not centrifugal force is included. Comparisons are drawn to existing laboratory experiments and

the presence of a centrifugally-driven large scale circulation is noted. This material has been submitted as Rubio *et al.* (2009*b*). Finally, general conclusions and future work are given in chapter 6.

Chapter 2

Governing equations, symmetries and numerical method

In this chapter aspects of the governing equations, symmetries and numerical method common to the three chapters that follow are discussed. An overview as well as details that are omitted in the individual chapters are given.

Governing equations

Consider the flow in a circular cylinder, with no-slip boundary conditions, of radius r_0 and depth d, rotating with an angular frequency ω. The endwalls are maintained at constant temperatures, $T_0 - \Delta T/2$ at the top and $T_0 + \Delta T/2$ at the bottom, with an insulating sidewall. The system is non-dimensionalized using d as the length scale, d^2/ν as the time scale (ν is the kinematic viscosity), $\nu^2\rho_0/d^2$ as the pressure scale (ρ_0 is the density at mean temperature T_0), and ΔT (the difference in temperature between the top and bottom) as the temperature scale. In formulating the governing equations it is worth noting that for many fluids of interest the variation in density with small changes of temperature is quite small, less than 1% for $\Delta T = 10^oC$, say. Variations in other fluid properties are necessarily on the same order as that of density and these small changes in fluid properties can safely be neglected except for a linear variation of density with respect to temperature in the body forces term. The primary advantage of this simplification, the Boussinesq approximation, is that the problem can then be treated as incompressible. In a frame of reference rotating at rate ω, the non-dimensional governing equations are

$$(\partial_t + \mathbf{u}\cdot\nabla)\mathbf{u} = -\nabla p + \nabla^2\mathbf{u} + \frac{Ra}{\sigma}(\Theta - z)\mathbf{z} + 2\Omega\mathbf{u}\times\mathbf{z} - \frac{RaFr}{\sigma\gamma}(\Theta - z)\mathbf{r}, \qquad (2.1)$$

$$(\partial_t + \mathbf{u}\cdot\nabla)\Theta = w + \sigma^{-1}\nabla^2\Theta, \qquad \nabla\cdot\mathbf{u} = 0, \qquad (2.2)$$

where $\mathbf{u} = (u, v, w)$ is the velocity in cylindrical coordinates (r, θ, z), P is the dynamic pressure, $\mathbf{r}$ is the radial unit vector in the r-direction, $\mathbf{z}$ is the vertical unit vector in the z-direction and Θ is the temperature deviation with respect to the conductive linear temperature profile; the relationship between Θ and the non-dimensional temperature T is given by

$$T = T_0/\Delta T - z + \Theta, \tag{2.3}$$

where $T_0/\Delta T - z$ is the conductive temperature profile.

There are five independent non-dimensional parameters:

Rayleigh number:	$Ra = \alpha g d^3 \Delta T/\kappa\nu$,
Coriolis number:	$\Omega = \omega d^2/\nu$,
Prandtl number:	$\sigma = \nu/\kappa$,
aspect ratio:	$\gamma = r_0/d$,
Froude number:	$Fr = \omega^2 r_0/g$,

where α is the coefficient of volume expansion, κ is the thermal diffusivity and g is the acceleration due to gravity. The boundary conditions (in a frame of reference rotating at rate ω) are:

$$\begin{aligned} r = \gamma: &\qquad \Theta_r = u = v = w = 0 \\ z = \pm 0.5: &\qquad \Theta = 0,\ u = v = w = 0. \end{aligned}$$

Symmetries

The governing equations and boundary conditions are invariant under arbitrary rotations about the axis, R_α, whose action is

$$R_\alpha(u, v, w, \Theta)(r, \theta, z, t) = (u, v, w, \Theta)(r, \theta + \alpha, z, t). \tag{2.4}$$

The basic state is always invariant to rotations and when $Ra > 0$ and $Fr > 0$ this state is a large scale circulation in which the colder, denser fluid near the top lid is centrifuged away from the axis of rotation and the warmer, lighter fluid near the bottom lid is drawn towards the axis of rotation. When $Fr = 0$ the governing equations and boundary conditions are also reflection-symmetric about the cylinder half-height. The action K_z of this so-called Boussinesq symmetry is

$$K_z(u, v, w, \Theta)(r, \theta, z, t) = (u, v, -w, -\Theta)(r, \theta, -z, t). \tag{2.5}$$

The symmetry group of the system without the centrifugal body force is $G = SO(2) \times Z_2$, with $SO(2)$ generated by R_α and Z_2 by K_z, with a G-invariant basic state, a quiescent layer of fluid with no temperature perturbation, $(u, v, w, \Theta) = (0, 0, 0, 0)$.

Nonlinear solver

The governing equations have been solved using the second order time-splitting method proposed in Hughes & Randriamampianina (1998) in which a predictor providing for a time variation of the pressure gradient at the boundaries consistent with a divergence-free velocity field is calculated at each time step. The permitted variation of pressure allows a time accuracy of the method of the same order as that of the 2nd order Adams-Bashforth backwards difference formula temporal scheme used, where the linear terms are treated implicitly and the nonlinear term along with certain body forces are treated explicitly. The temporal scheme is given by:

$$(\frac{3}{2\Delta t} - \frac{1}{\sigma}\Delta)\Theta^{n+1} = \frac{1}{2\Delta t}(4\Theta^n - \Theta^{n-1}) - 2\mathbf{u}^n \cdot \nabla\Theta^n + \mathbf{u}^{n-1} \cdot \nabla\Theta^{n-1} + \frac{1}{d}(2w^n - w^{n-1}), \tag{2.6}$$

$$\frac{1}{2\Delta t}(3\mathbf{u}^{n+1} - 4\mathbf{u}^n + \mathbf{u}^{n-1}) + 2\mathbf{N}(\mathbf{u}^n) - \mathbf{N}(\mathbf{u}^{n-1}) = -\nabla p^{n+1} + \Delta\mathbf{u}^{n+1} + \mathbf{F}^{n+1}, \tag{2.7}$$

where $\mathbf{N}(\mathbf{u}) = (\mathbf{u} \cdot \nabla)\mathbf{u}$ and $\mathbf{F}^{n+1}$ denotes the Coriolis and buoyancy body forces in the momentum equation at the $(n+1)$-th timestep. The Coriolis term depends on $\mathbf{u}$ and is treated explicitly ($\mathbf{F}^{n+1}$ is replaced by $2\mathbf{F}^n - \mathbf{F}^{n-1}$) while the centrifugal and gravitational buoyancy terms depend on Θ only and are updated before they are used in the momentum equation. The velocity and pressure are updated in the following four steps. The pressure predictor, p^*, is computed using a consistent boundary condition suggested by Gresho & Sani (1987) resulting in the following Poisson problem,

$$\Delta p^* = \nabla \cdot \mathbf{E}^{n+1} \in D, \tag{2.8}$$

$$\frac{\partial p^*}{\partial n} = \mathbf{n} \cdot (\frac{1}{2\Delta t}(-3\mathbf{w}^{n+1} + 4\mathbf{u}^n - \mathbf{u}^{n-1}) + (2\mathbf{L}(\mathbf{u}^n) - \mathbf{L}(\mathbf{u}^{n-1})) + \mathbf{E}^{n+1})) \in \partial D, \tag{2.9}$$

where $\mathbf{E}^{n+1} = -2\mathbf{N}(\mathbf{u}^n) - \mathbf{N}(\mathbf{u}^{n-1}) + \mathbf{F}^{n+1}$, D denotes the interior of domain, ∂D the boundary of the domain, $\mathbf{w}^n$ is the correct velocity given by the boundary conditions (since $\mathbf{u}^n$ satisfies the no-slip condition on ∂D to $O(\Delta t^3)$) and $\mathbf{L}(\mathbf{u}) = \nabla \times (\nabla \times \mathbf{u})$ is the solenoidal part of $\Delta \mathbf{u}$ where the irrotational part, $\nabla(\nabla \cdot \mathbf{u})$, is assumed to be zero. The velocity corrector is computed as the following Helmholtz problem,

$$(\Delta - \frac{3}{2\Delta t})\mathbf{u}^* = -\frac{1}{2\Delta t}(4\mathbf{u}^n - \mathbf{u}^{n-1}) + (\nabla p^* - \mathbf{E}^{n+1}) \in D, \tag{2.10}$$

$$\mathbf{u}^* = \mathbf{w}^{n+1} \in \partial D. \tag{2.11}$$

The next step is an explicit evaluation of the final divergence-free velocity field, computed via the pressure-like intermediate variable $\phi = \frac{2\Delta t}{3}(p^{n+1} - p^{*n+1})$, as a Poisson

problem,

$$\Delta\phi = \nabla \cdot \mathbf{u}^* \in D, \tag{2.12}$$

$$\frac{\partial \phi}{\partial n} = 0 \in \partial D. \tag{2.13}$$

Finally, the pressure and velocity fields are corrected,

$$p^{n+1} = p^* + \frac{3}{2\Delta t}\phi, \mathbf{u}^{n+1} = \mathbf{u}^* - \nabla\phi. \tag{2.14}$$

A pseudo-spectral method is used for the spatial discretization, with a Galerkin–Fourier expansion in the azimuthal coordinate θ and Chebyshev collocation in r and z. In order to handle the coordinate singularity at the axis due to the use of polar coordinates, and avoid unnecessary clustering of grid points near the axis, the prescription in Fornberg (1998) has been followed. An added benefit is the desirable clustering of grid points near the boundaries, enhancing resolution of the boundary layers. The expansion for the thermal perturbation is given by

$$\Theta(r,\theta,z) = \Re \sum_{m=0}^{2n_r+1} \sum_{n=0}^{n_z} \sum_{k=-n_\theta/2}^{n_\theta/2-1} \Theta_{mnk} T_m(r/\gamma) T_n(2z) e^{ik\theta}. \tag{2.15}$$

The expansions for the velocity components u, v and w are analogous. Fornberg's prescription is that $\Theta_{mnk} = w_{mnk} = 0$ when $k+m$ is odd, and $u_{mnk} = v_{mnk} = 0$ when $k+m$ is even; there are precisely $n_r + 1$ non-zero coefficients for fixed n and k in (3.11). Due to the expansion (3.11) the origin is never a collocation point, and the equations are solved in the physical domain $(r,\theta,z) = (0,\gamma] \times (0,2\pi] \times [-1/2,1/2]$. Following Orszag & Patera (1983), we have used the combinations $u_+ = u + iv$ and $u_- = u - iv$ in order to decouple the linear diffusion terms in the momentum equations. For each Fourier mode, the resulting Helmholtz equations for Θ, w, u_+ and u_- have been solved using a diagonalization technique in the two coordinates r and z. Fornberg's prescription guarantees the regularity conditions at the origin

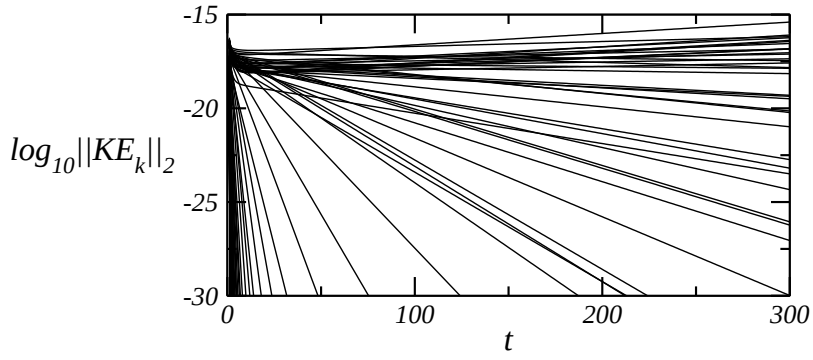

Figure 2.1: Time series of kinetic energies of different modal energies for a linear stability analysis at $Ra = 2370$, $\Omega = 19.7$, $\sigma = 4.5$, $\gamma = 11.8$ and $Fr = 0$. Here the basic state $(u, v, w, \Theta)(r, \theta, z) = (0, 0, 0, 0)$.

needed to solve the Helmholtz equations (Mercader, Net & Falqués, 1991) by ensuring that the expansion is well-defined and infinitely differentiable at $r = 0$. The spatial and temporal resolution requirements for each problem are given in the individual chapters that follow.

Generalized linear stability analysis

The linear stability analysis was performed via direct numerical stability analysis. First, a steady axisymmetric basic state is computed at some point in parameter space, and its stability is determined by introducing small random perturbations into all azimuthal Fourier modes resulting in an initial condition of the form,

$$\mathbf{u}(r, \theta, z, 0) = \mathbf{u}_b(r, z) + \sum_{k=-n_\theta/2}^{n_\theta/2-1} \mathbf{u}_k(r, z, 0) e^{ik\theta}, \tag{2.16}$$

$$\Theta(r, \theta, z, 0) = \Theta_b(r, z) + \sum_{k=-n_\theta/2}^{n_\theta/2-1} \Theta_k(r, z, 0) e^{ik\theta}, \tag{2.17}$$

$$p(r, \theta, z, 0) = p_b(r, z) + \sum_{k=-n_\theta/2}^{n_\theta/2-1} p_k(r, z, 0) e^{ik\theta}, \tag{2.18}$$

where $\mathbf{u}_b$, Θ_b and p_b are the velocity, thermal perturbation and pressure fields of the basic state. For each k the initial condition $(\mathbf{u}_k, \Theta_k, p_k)(r, z, 0)$ is a random disturbance of order 10^{-10}. Instead of solving the resulting linear system the action of the Jacobian is computed via time evolution of the Navier-Stokes-Boussinesq equations, resulting in a matrix-free power method. For sufficiently small perturbations, the nonlinear couplings between Fourier modes are negligible (below round-off numerical noise) and the growth rates (real parts of the eigenvalues) and structure of the eigenfunctions corresponding to the fastest growing perturbation at each Fourier mode emerge from time evolution. Figure 2.1 shows the initial transient and exponential growth of the small amplitude perturbations described above for $Ra = 2370$, $\Omega = 19.7$, $\sigma = 4.5$, $\gamma = 11.8$ and $Fr = 0$. For this case the initial transients decay in roughly 100 viscous times and the growth rate of the amplitude of each eigenfunction, corresponding to a single Fourier mode, is easily measured as the slope of the logarithm of the $L2-$norm of the kinetic energy. By computing the exponential growth and decay rates of the eigenfunctions corresponding to a range of Ra a linear interpolation to zero gives an accurate estimate for the onset of marginal stability for eigenfunctions corresponding to each Fourier mode. Using this method, a direct comparison between stability analyses of $Fr = 0$ cases (with a trivial basic state) and $Fr > 0$ cases whose nontrivial basic states must be computed in the axisymmetric subspace, can be made.

Chapter 3

Modulated rotating convection: Radially traveling concentric rolls

The Author's earliest research into the nature of rotating convection was a numerical survey of the axisymmetric subspace over a range of Ra and Fr for a parameter regime for which the onset of convection occurs as a wall mode (Lopez *et al.*, 2006*b*). In this purely theoretical study the dynamics of different branches of axisymmetric solutions of the Navier-Stokes equations, including two branches of inwardly travelling waves that emerged via infinite-period bifurcations, were discussed in order to understand the effect of centrifugal force on the simplest fully nonlinear case of rotating convection. Although the solutions mentioned above are unstable to 3D perturbations there are recent experiments in rotating convection showing that the spatio-temporal bulk convective state with Küppers–Lortz dynamics can be suppressed by small amplitude modulations of the rotation rate (Thompson *et al.*, 2002). The resultant axisymmetric pulsed target patterns were observed to develop into axisymmetric traveling target patterns as the modulation amplitude and Rayleigh number were increased. Using the Navier–Stokes–Boussinesq equations with physical boundary conditions, the experimental results were numerically reproduced and physical insight into the responsible mechanism was gained, relating the onset of the traveling target patterns to a symmetry-restoring saddle-node on an invariant circle bifurcation. This research was published as Rubio *et al.* (2008) and is a joint work with Juan M. Lopez[1] and Francisco Marques[2]. The media cited in this chapter can be found at $http://mathpost.la.asu.edu/\sim rubio/JFM\_RLM07\_media/jfm\_RLM07.html$.

[1]Department of Mathematics and Statistics, Arizona State University, lopez@asu.edu
[2]Departament de Física Aplicada, Universitat Politècnica de Catalunya, marques@fa.upc.edu

3.1 Introduction

It is well known that temporal forcing in dynamical systems can stabilize states that are otherwise unstable, as well as producing new phenomena not present in the unforced problem (Davis, 1976). Recent examples in fluid dynamics include Taylor–Couette flow with axial harmonic oscillations of the inner cylinder that substantially shift the transition to Taylor vortices to faster rotations rates of the inner cylinder (Weisberg, Kevrekidis & Smits, 1997; Marques & Lopez, 1997). In that problem, when the transition does occur, it takes place in a complex, catastrophic way (Sinha, Kevrekidis & Smits, 2006; Avila, Marques, Lopez & Meseguer, 2007*b*). Another striking example is vortex breakdown in a cylindrical container driven by the rotation of one endwall. In that case the oscillations of the vortex breakdown bubbles are quenched by a small amplitude harmonic modulation of the rotation (Lopez *et al.*, 2008). These are all examples of how the oscillatory Stokes layers produced by the harmonic modulations inhibit instabilities of the unmodulated state.

Rayleigh–Bénard convection has been, and continues to be, a very popular hydrodynamic system in which to study the effects of temporal forcing (Davis, 1976; Bodenschatz, Pesch & Ahlers, 2000). The early studies either modulated the vertical acceleration or the temperature applied at a horizontal boundary, and were primarily concerned with shifts in the threshold for the onset of convection due to the modulation. Both of these modes of modulation suffer from experimental limitations in their implementation (Bodenschatz *et al.*, 2000) as well as theoretical issues arising from the forced breaking of the mid-plane reflection symmetry, commonly referred to as the Boussinesq symmetry (Roppo, Davis & Rosenblat, 1984).

Rotating Rayleigh–Bénard convection (RRBC) in a cylinder, where the rotation rate is modulated, has been studied theoretically (Bhattacharjee, 1990) and experi-

mentally (Niemela, Smith & Donnelly, 1991) with regards to threshold shifts. More recently, Thompson, Bajaj & Ahlers (2002) experimentally observed synchronous spiral and axisymmetric pulsed target patterns (the observed type of pattern depending on experimental protocols) at low modulation amplitudes of the rotation rate in parameter regimes where the unmodulated state manifested spatio-temporal Küppers–Lortz (KL) dynamics (Küppers & Lortz, 1969). At larger modulation amplitudes, the axisymmetric pulsed target patterns undergo transition to a modulated traveling target pattern in which the innermost convective roll collapses in on itself and a new convective roll develops at larger radii as the entire pattern drifts radially inward. The target and spiral patterns have been qualitatively computed using a model based on the Swift–Hohenberg equation (Roxin & Riecke, 2002). The model essentially treated the problem as a two-dimensional pattern-forming system, neglecting its vertical structure. The qualitative nature of the model precluded quantitative comparisons with the experiments. Furthermore, the radially traveling target patterns could not be simulated using that model and the origin of the radial drift remained unidentified.

Similar radially traveling target patterns have been simulated using the Navier–Stokes–Boussinesq equations in axisymmetric subspaces of both non-rotating (Tuckerman & Barkley, 1988) and rotating (Lopez, Rubio & Marques, 2006*b*) Rayleigh–Bénard convection in cylinders. In both cases, the traveling target patterns were found to originate at a SNIC (saddle-node on an invariant circle) bifurcation. Here, we have simulated the conditions corresponding to the experiments of Thompson *et al.* (2002) using the Navier–Stokes–Boussinesq equations and have reproduced the various observed states, including the radially traveling target patterns. By considering how the period of the traveling target pattern varies with the forcing amplitude and the Rayleigh number, we show that the traveling target patterns in the modulated

rotation problem also arise via a SNIC bifurcation in which the Boussinesq symmetry plays a central role. Furthermore, it is apparent that it is not the modulated rotation that is responsible for the radial drift, but rather the restriction of the dynamics to an axisymmetric subspace in which the SNIC bifurcation of pulsed target patterns leads to the radially traveling circular rolls.

The nature of this problem captures the competition and non-linear interactions between thermal convective instabilities and the large scale circulation mechanically driven by the modulated rotation of the cylinder. In the absence of modulation, for large enough Rayleigh number, the base state consists of Küppers-Lortz spatio-temporal chaos. On the other hand, for small Rayleigh number, the base state consists of the oscillatory axisymmetric large scale circulation originating in the Stokes layers at the top and bottom boundaries. When both mechanisms are of comparable strength, the numerical simulations show that the Küppers-Lortz chaotic state is replaced by pulsed and travelling target patterns, in agreement with the aforementioned experimental results.

3.2 Governing equations, symmetries, and numerical technique

Governing equations

Consider the flow in a circular cylinder, with no-slip boundary conditions, of radius r_0 and depth d, with a modulated rotation $\omega(t^*) = \omega_0 + \omega_1 \sin(\omega_m t^*)$, where t^* is dimensional time in seconds. The endwalls are maintained at constant temperatures, $T_0 - \Delta T/2$ at the top and $T_0 + \Delta T/2$ at the bottom, and the sidewall is insulating. The Boussinesq approximation is implemented, treating all fluid properties as constant except for the density in the gravitational term, which varies linearly with temperature. The centrifugal buoyancy (Lopez *et al.*, 2006*b*; Marques *et al.*, 2007) is ignored in this paper since in the experiments (Thompson *et al.*, 2002), the Froude number was very small ($Fr = \omega_0^2 r_0/g < 0.016$, where r_0 is the cylinder radius, ω_0 is

the mean rotation rate and g is the gravitational acceleration). The system is non-dimensionalized using d as the length scale, d^2/ν as the time scale (ν is the kinematic viscosity), $\nu^2\rho_0/d^2$ as the pressure scale (ρ_0 is the density at mean temperature T_0), and ΔT (the difference in temperature between the top and bottom) as the temperature scale. In a frame of reference rotating at the mean rotation rate ω_0, the non-dimensional governing equations are

$$(\partial_t + \mathbf{u}\cdot\nabla)\mathbf{u} = -\nabla P + \nabla^2\mathbf{u} + \frac{Ra}{\sigma}(\Theta - z)\hat{z} + 2\Omega_0\mathbf{u}\times\hat{z} - \frac{RaFr}{\sigma\gamma}(\Theta - z)r, \quad (3.1)$$

$$(\partial_t + \mathbf{u}\cdot\nabla)\Theta = w + \sigma^{-1}\nabla^2\Theta, \qquad \nabla\cdot\mathbf{u} = 0, \quad (3.2)$$

where $\mathbf{u} = (u, v, w)$ is the velocity field in cylindrical coordinates (r, θ, z), P is the dynamic pressure, $\hat{z}$ is the vertical unit vector in the z-direction. As noted above, $Fr = 0$ in this study. Θ is the temperature deviation with respect to the conductive linear temperature profile; the relationship between Θ and the temperature T (both nondimensional) is given by

$$T = T_0/\Delta T - z + \Theta, \quad (3.3)$$

where $T_0/\Delta T - z$ is the conductive temperature profile.

There are six non-dimensional parameters:

Rayleigh number:	$Ra = \alpha g d^3 \Delta T/\kappa\nu$,
Coriolis number:	$\Omega_0 = \omega_0 d^2/\nu$,
Prandtl number:	$\sigma = \nu/\kappa$,
aspect ratio:	$\gamma = r_0/d$,
modulation amplitude:	$\Omega_1 = \omega_1 d^2/\nu$,
modulation frequency:	$\Omega_m = \omega_m d^2/\nu$,

where α is the coefficient of volume expansion, and κ is the thermal diffusivity. The boundary conditions (in a frame of reference rotating at the mean rotation rate ω_0) are:

$$\begin{aligned} r = \gamma : \qquad & \Theta_r = u = w = 0, v = \gamma\Omega(t) \\ z = \pm 0.5 : \qquad & \Theta = 0,\ u = w = 0, v = r\Omega(t), \end{aligned}$$

where $\Omega(t) = \Omega_1 \sin(\Omega_m t)$ is the angular velocity of the container in the reference frame rotating with the mean angular velocity Ω_0. To simplify the discussion, we introduce the relative modulation amplitude $A = \Omega_1/\Omega_0$ to allow for comparison between states with differing Ω_0. A will be used instead of Ω_1, except in the particular case when $\Omega_0 = 0$, as then A is not defined.

Symmetries

The governing equations and boundary conditions are invariant under arbitrary rotations about the axis, R_α, whose action is

$$R_\alpha(u, v, w, \Theta)(r, \theta, z, t) = (u, v, w, \Theta)(r, \theta + \alpha, z, t). \tag{3.4}$$

They are also reflection-symmetric about the cylinder half-height. The action K_z of this so-called Boussinesq symmetry is

$$K_z(u, v, w, \Theta)(r, \theta, z, t) = (u, v, -w, -\Theta)(r, \theta, -z, t). \tag{3.5}$$

The symmetry group of the system is $G = SO(2) \times Z_2$, with $SO(2)$ generated by R_α and Z_2 by K_z. The basic state is G-invariant and τ_m-periodic, where $\tau_m = 2\pi/\Omega_m$.

In the absence of any rotation ($\Omega_0 = \Omega_1 = 0$), the system is also invariant under reflections on meridional planes (θ constant), that together with the invariance to rotations about the axis generate the $O(2) = SO(2) \rtimes Z_2$ symmetry group; the Z_2

component is generated by the reflection (angle flip) symmetry

$$K_\theta(u, v, w, \Theta)(r, \theta, z, t) = (u, -v, w, \Theta)(r, -\theta, z, t). \tag{3.6}$$

The symbol $\rtimes$ indicates the semidirect product of the symmetry groups; it is not the direct product ($\times$) because the flip symmetry K_θ does not commute with axial rotations R_α: $K_\theta R_\alpha = R_{-\alpha} K_\theta$. The symmetry group of the system in the absence of any rotation is $G = O(2) \times Z_2$. Note further that when the modulated rotation has zero mean ($\Omega_0 = 0$, but $\Omega_1 \neq 0$), the angle flip K_θ is no longer a symmetry of the problem, but the system is still invariant under a space-time symmetry H, whose action is the composition of K_θ with an evolution of half the modulation period:

$$H(u, v, w, \Theta)(r, \theta, z, t) = (u, -v, w, \Theta)(r, -\theta, z, t + \tau_m/2). \tag{3.7}$$

In particular, when restricting the $\Omega_0 = 0$ problem to the axisymmetric subspace, the symmetry group of the system in the zero mean modulation case is $Z_2 \times Z_2$, generated by H and K_z. Although in this paper we only consider non-zero mean rotations, $\Omega_0 \neq 0$, some of the solutions obtained exhibit characteristics of the symmetry H being slightly broken, since the values of Ω_0 considered are relatively small. Finally, it is useful to introduce a global Poincaré map which is the stroboscopic map of the periodically forced system

$$P(u, v, w, \Theta)(r, \theta, z, t_0) \mapsto (u, v, w, \Theta)(r, \theta, z, t_0 + \tau_m). \tag{3.8}$$

For any function of time $f(t)$, we can analogously define the action of P on it as $(Pf)(t_0) = f(t_0 + \tau_m)$; the time phase t_0 can be chosen arbitrarily, resulting in different Poincaré maps, all of them equivalent. To be specific, in this paper we will use the phase $t_0 = 0$. For any variable $f(t)$, the discrete orbit generated by P, starting at $f(0)$, is given by $P^n f = f(n\tau_m)$; it is obtained by strobing $f(t)$ at the beginning of each forcing period.

To describe the heat transfer properties of a solution we use the Nusselt number, the ratio between the heat transfer of the solution considered, and the heat transfer of the conductive state, both through the top lid. It is given by the negative average of the derivative of the temperature field at the top lid,

$$Nu = - < \partial T/\partial z > |_{z=0.5} =< 1 - \partial\Theta/\partial z > |_{z=0.5} . \tag{3.9}$$

One could also compute the heat transfer at the bottom lid, $Nu^b =< \partial T/\partial z > |_{z=-0.5}$. The K_z reflection relates Nu and Nu^b; the relationship depends on how the solution considered transforms under K_z. The breaking of K_z-symmetry will be one of the focuses of this paper, resulting in pairs of K_z-symmetry related states. Integrating the temperature equation (5.2) in the fluid domain and using the divergence theorem and the boundary conditions of the problem, the following relationship between both Nusselt numbers is obtained,

$$Nu^b - Nu = \sigma \frac{d}{dt} < T >_V , \tag{3.10}$$

where $< >_V$ means the volume average in the fluid domain. For steady solutions, the time derivative is zero, and the Nusselt numbers coincide: $Nu = Nu^b$; therefore, K_z-related steady solutions must have the same Nusselt number value. For periodic solutions, both Nusselt numbers are time dependent; their instantaneous values are not necessarily the same, but their time-averaged values are still identical (because the average of the time derivative in (3.10) is zero). Therefore, K_z-related periodic solutions have different instantaneous Nusselt number values, and so different $P^n(Nu)$ values. However, their time-averaged values are the same. For periodically forced flows, as in the present problem, it is very convenient to use the Nusselt number averaged over a forcing period, $\overline{Nu}$.

Numerical technique

The governing equations have been solved using the second order time-splitting method proposed in Hughes & Randriamampianina (1998) combined with a pseudo-spectral method for the spatial discretization, utilizing a Galerkin–Fourier expansion in the azimuthal coordinate θ and Chebyshev collocation in r and z. In order to handle the coordinate singularity at the axis due to the use of polar coordinates, and avoid unnecessary clustering of grid points near the axis, the prescription in Fornberg (1998) has been followed. The expansion for the thermal perturbation is given by

$$\Theta(r,\theta,z) = \Re \sum_{m=0}^{2n_r+1} \sum_{n=0}^{n_z} \sum_{k=-n_\theta/2}^{n_\theta/2-1} \Theta_{mnk} T_m(r/\gamma) T_n(2z) e^{ik\theta}. \tag{3.11}$$

The expansions for the velocity components u, v and w are analogous. Fornberg's prescription is that $\Theta_{mnk} = w_{mnk} = 0$ when $k+m$ is odd, and $u_{mnk} = v_{mnk} = 0$ when $k+m$ is even; there are precisely n_r+1 non-zero coefficients for fixed n and k in (3.11). Due to the expansion (3.11) the origin is never a collocation point, and the equations are solved in the physical domain $(r,\theta,z) = (0,\gamma] \times (0,2\pi] \times [-1/2,1/2]$. Following Orszag & Patera (1983), we have used the combinations $u_+ = u + iv$ and $u_- = u - iv$ in order to decouple the linear diffusion terms in the momentum equations. For each Fourier mode, the resulting Helmholtz equations for Θ, w, u_+ and u_- have been solved using a diagonalization technique in the two coordinates r and z. Fornberg's prescription guarantees the regularity conditions at the origin needed to solve the Helmholtz equations (Mercader, Net & Falqués, 1991).

We have tested the code on a number of convection problems in rotating cylinders (Lopez *et al.*, 2006*b*; Marques *et al.*, 2007; Lopez *et al.*, 2007), establishing resolution requirements over a wide range of parameter regimes. For the problems considered in this paper, we have used $n_r = 64$ and $n_z = 24$ Chebyshev modes. For cases where

the solution is non-axisymmetric, we have used up to $n_\theta = 184$ Fourier modes. We have used time-steps $\delta t \leq 10^{-3}$ viscous time units (depending on the modulation frequency). We have fixed the aspect ratio $\gamma = 11.8$ and Prandtl number $\sigma = 4.5$ to correspond to those in the experiments of Thompson *et al.* (2002), and consider variations in A and Ω_m for selected values of Ra and Ω_0 in the range considered in the experiments. To simulate the experimentally observed axisymmetric patterns, we restrict our computations to the axisymmetric subspace. This restriction affords a detailed exploration of the dynamics over an extensive range of parameter space.

3.3 Results

We begin by briefly describing the unmodulated RRBC state which is being quenched by the modulated rotation. It is a state of spatio-temporal complexity which arises essentially directly from the conduction state as Ra is increased (for the rotation rates considered here).

Unmodulated RRBC: Küpper–Lortz state

In the absence of modulation ($A = 0$), for Ra less than a critical value Ra_c that depends on Ω_0, γ and σ, the system is in a state of solid body rotation with a linear temperature profile in z, i.e. the trivial conduction state. For $Ra > Ra_c$, KL spatio-temporal chaos is observed. This consists of patterns of convection rolls that break up into domains of various orientations with propagating fronts between the domains, and defects that nucleate at the cylinder wall evolving into growing patches of rolls oriented at angles different from the rolls nearby in the interior, all occurring with temporal irregularity. Figure 3.1 shows computed isotherms at mid-height of a KL state at $Ra = 2868.8$ and $\Omega_0 = 23.6$, corresponding to the experimental conditions of the KL state in figure $1(a)$ of Thompson *et al.* (2002). Movie 1, available in the online version, shows the spatio-temporal characteristics of the isotherms at mid-height of

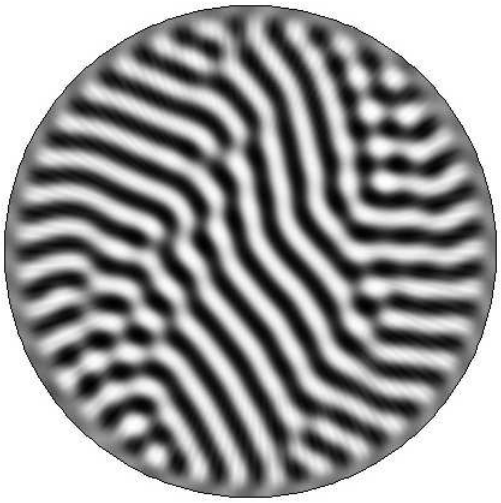

Figure 3.1: Snap-shot of isotherms at mid-height of a Küppers–Lortz state at $Ra = 2868.8$, $\Omega_0 = 23.6$, $\gamma = 11.8$ and $A = 0$. Movie 1, available in the online version, shows the spatio-temporal characteristics of the isotherms at mid-height of this state over 450 viscous times at a rate of 20 frames per second, with each frame being 0.45 viscous times apart.

this state over 450 viscous times at a rate of 20 frames per second, with each frame being 0.45 viscous times apart. This state is typical for the range of Ra and Ω_0 considered in this paper when $A = 0$. The associated spatio-temporal chaos has been the subject of extensive experimental and amplitude equations investigations (see the review articles of Knobloch, 1998; Bodenschatz *et al.*, 2000, and references therein), and more recently it has also been studied numerically using the Navier–Stokes–Boussinesq equations with no-slip boundary conditions (Scheel & Cross, 2005; Sánchez-Álvarez, Serre, Crespo del Arco & Busse, 2005; Becker, Scheel, Cross & Ahlers, 2006).

Modulated basic state

In the modulated problem ($A \neq 0$), there is no trivial conduction state for any $Ra \neq 0$ as the modulated rotation induces a mechanically driven large scale flow.

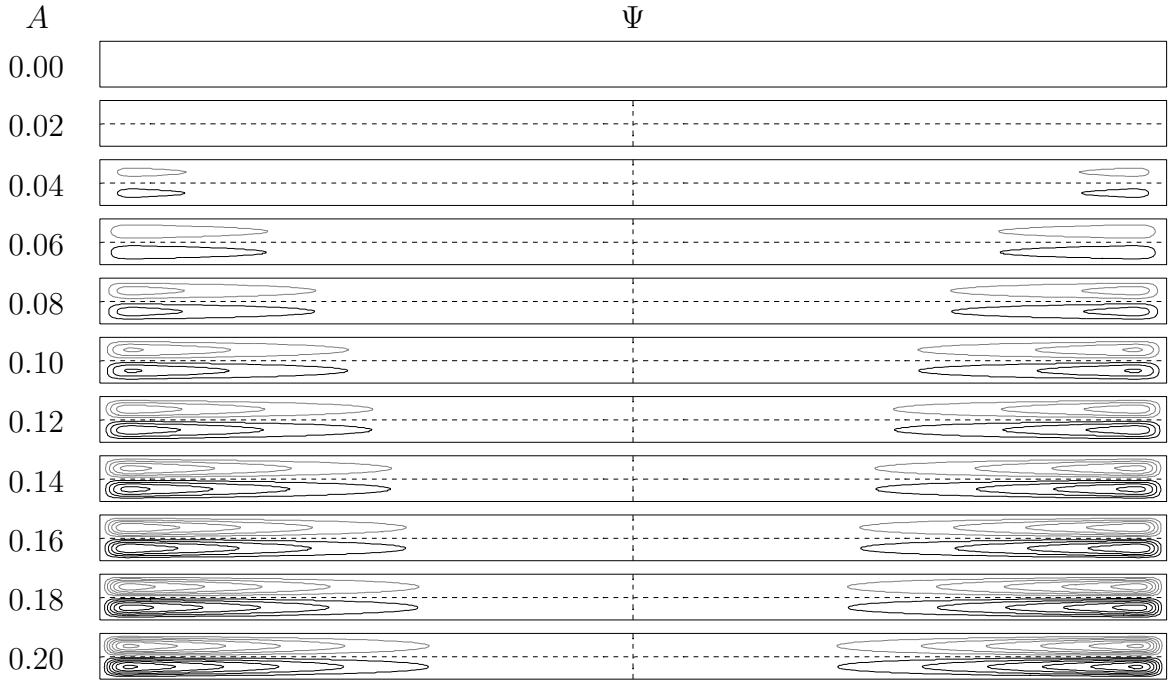

Figure 3.2: Snap-shots in a meridional plane ($r \in [-\gamma, \gamma], z \in [-0.5, 0.5]$) of the stream function of basic states, all at the same phase of the imposed modulation, at $Ra = 2600$, $\Omega_0 = \Omega_m = 23.6$ and indicated A. Five contours are spaced linearly with $\Psi \in [-5, 5]$; black (grey) contours are negative (positive) and the zero contour is dashed.

Without modulation, for $Ra < Ra_c(\Omega_0, \gamma, \sigma)$, the flow is in a state of solid body rotation with a linear temperature profile vertically across the layer ($\Theta = 0$). For any modulation, $A \neq 0$, Stokes layers (analogues of the boundary layer on a plate oscillating in its own plane; see Stokes, 1851; Batchelor, 1967; Kerczek & Davis, 1974; Davis, 1976; Yih, 1977) form on the top and bottom boundaries, whose thickness scale with $1/\sqrt{\Omega_m}$. These Stokes layers arise as the vortex lines, which for $A = 0$ are parallel to the rotation axis, are displaced in the layers radially outward (inward) during the acceleration (deceleration) phase of the modulation. This bending of the vortex lines in the Stokes layers gives rise to a secondary flow which centrifuges fluid in the layers radially outward (inward) with the acceleration (deceleration) of the

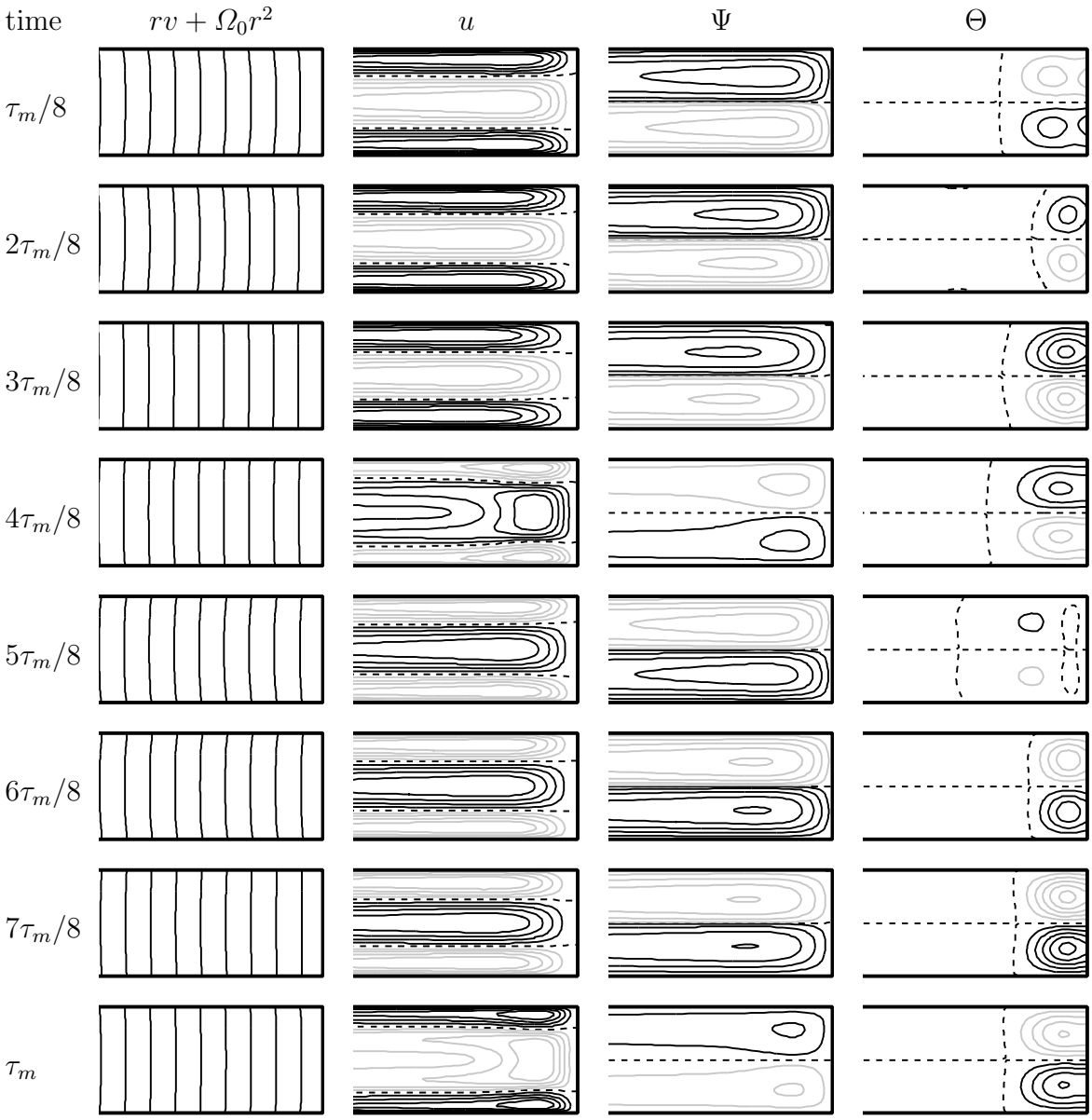

Figure 3.3: Contours of the angular momentum $rv + \Omega_0 r^2$, radial velocity u, stream function Ψ, and the temperature deviation Θ in a part of a meridional plane near the sidewall ($r \in [0.8\gamma, \gamma], z \in [-0.5, 0.5]$) over one forcing period $\tau_m = 2\pi/\Omega_m$, for a modulated basic state at $Ra = 2600$, $\Omega_0 = \Omega_m = 23.6$ and $A = 0.05$. Five contour levels are linearly spaced for $\Theta \in [-0.025, 0.025]$ and $u \in [-10, 10]$, and five contour levels are quadratically spaced for $\Psi \in [-1.25, 1.25]$ and ten contours are quadratically spaced for $rv + \Omega_0 r^2 \in [9500, 14250]$.

rotation of the cylinder. The modulated rotation also drives fluid into and out of the Stokes layers from the interior (the associated Ekman pumping phenomenon). However, the major impact on the interior flow comes from the fluid in the top and bottom Stokes layers being deflected into the sidewall layer and forming a radial jet at mid-height ($z = 0$). This radial jet injects fluid with high angular momentum (acquired in the Stokes layers) into the interior at mid-height during the acceleration phase. During the deceleration phase, the fluid flows in the opposite direction: fluid from the interior is sucked into the sidewall layer and transported into the top and bottom Stokes layers. In figure 3.2 we show the development of the Stokes layers and sidewall jet with increasing A at $Ra = 2600$ with $\Omega_0 = \Omega_m = 23.6$, at a fixed phase of the modulation (during the acceleration phase, when the radial outflow in the Stokes layer is greatest). For small A, the actions of the Stokes layers and sidewall jet are restricted to the vicinity of the sidewall. As A is increased, this action extends deeper in toward the axis, roughly as $\sqrt{A}$. The flow in the center of the cell remains essentially in solid body rotation out to a radius that depends on both A and Ω_m.

Figure 3.3 illustrates the hydrodynamics of the modulated basic state in the neighborhood of the sidewall, $r \in [0.8\gamma, \gamma]$, for $Ra = 2600$, $\Omega_0 = \Omega_m = 23.6$ and $A = 0.05$ (under these conditions, the basic state is stable). Shown in the first column of the figure is the just-mentioned vortex line bending driving the secondary flow and sidewall jet (illustrated by the radial velocity in the second column, and instantaneous streamlines in the third column), which drive a time-dependent temperature perturbation (shown in the fourth column). This temperature deviation, consisting of relatively hot and cold axisymmetric rolls at the lower and upper corners of the sidewall, alternating synchronously with the forcing, exists for all Ra when $A \neq 0$. Their presence leads to a heat flux across the layer enhanced from that due purely to conduction, i.e. for any $Ra > 0$ and $A > 0$, the Nusselt number is $Nu > 1$.

The modulated basic state is both axisymmetric and K_z-reflection symmetric about $z = 0$, i.e. the symmetry group of the basic state is $SO(2) \times Z_2$, and it is synchronous with the modulation frequency. The usual $Nu > 1$ criterion for the onset of thermal convection cannot be used to determine the instability of the basic state. Instead, we detect the onset of axisymmetric thermal convection by monitoring the temperature on the axis at mid-height $\Theta_m(t) = \Theta(r = 0, \theta = 0, z = 0, t)$. For the basic state, $\Theta_m = 0$, and the onset of axisymmetric convection breaks the Boussinesq reflection symmetry K_z, giving states with $\Theta_m \neq 0$.

Onset of thermal convection: Axisymmetric pulsed target patterns

For a given $A \neq 0$, on increasing Ra beyond $Ra_c = 2627$, the modulated basic state loses stability via a pitchfork bifurcation that breaks the Boussinesq reflection symmetry K_z. At this bifurcation, a pair of states synchronous with the modulation period emerge. Near the sidewall, the hydrodynamics of these bifurcating pulsed target patterns is very similar to that of the modulated basic state (illustrated in figure 3.3), although the symmetry K_z has been broken by the onset of convection, as can be seen in figure 3.4. This symmetry breaking is characterized by the development of a thermal plume at the axis, which comes in two varieties: one is a hot plume rising and the other is a cold plume descending on the axis. These plumes can be seen in figures 3.5 and 3.6, which show snap-shots at increasing Ra of Θ-isotherms in a meridional plane, at a fixed phase of the modulation, for $\Omega_0 = \Omega_m = 23.6$ and $A = 0.18$ and 0.05 respectively, illustrating the development of the pulsed target patterns. With increasing Ra, concentric rolls develop growing out from the axis; The sidewall jet displaces the nearby rolls alternately closer to and further from the axis of rotation with no net movement over the course of a forcing period as can be seen in figure 3.4. The isotherms corresponding to the symmetrically-related branch

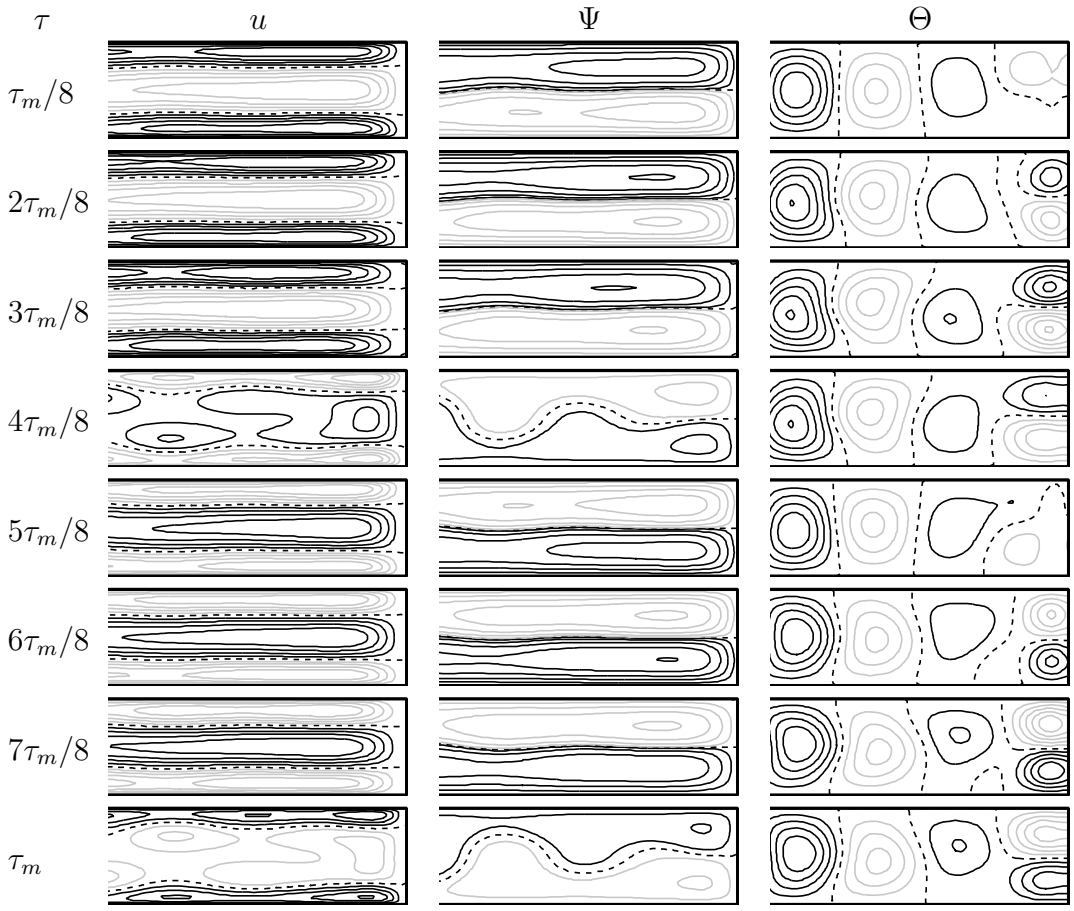

Figure 3.4: Contours of the radial velocity u, stream function Ψ and temperature deviation Θ in a meridional plane ($r \in [0.74\gamma, \gamma], z \in [-0.5, 0.5]$) over one forcing period of the pulsed target pattern at $Ra = 2700$, $\Omega_0 = \Omega_m = 23.6$, and $A = 0.05$. Five contours are quadratically spaced for $\Psi \in [-1.25, 1.25]$ and are linearly spaced for $\Theta \in [-0.025, 0.025]$ and $u \in [-10, 10]$.

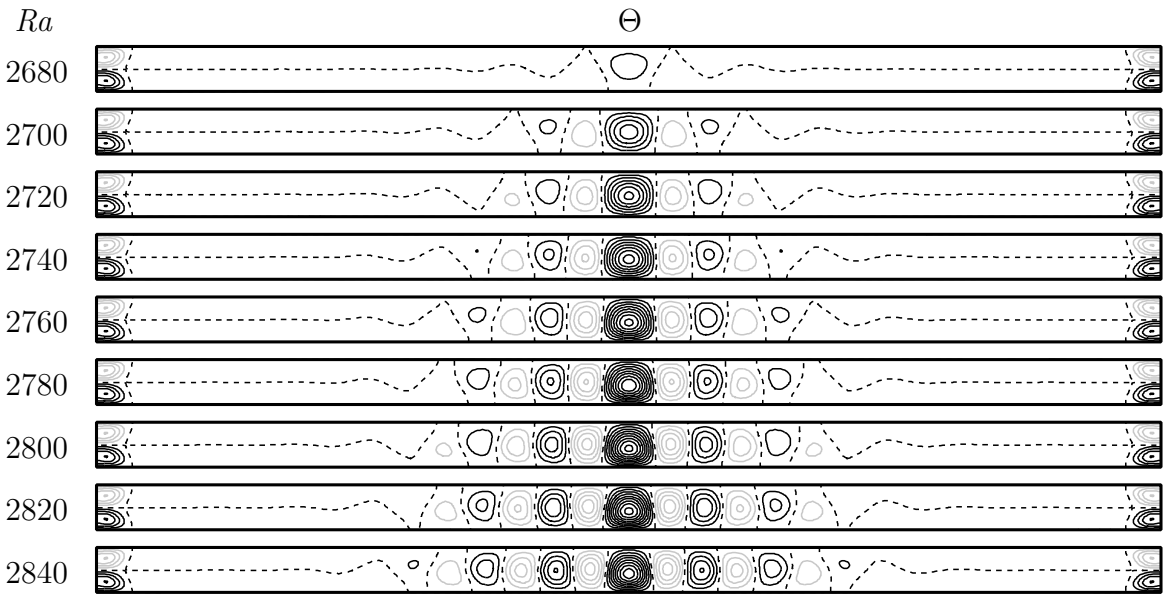

Figure 3.5: Snap-shots in a meridional plane of Θ for pulsed target states, all at the same phase of the imposed modulation, at $A = 0.18$ and $\Omega_0 = \Omega_m = 23.6$ for Ra as indicated. Ten contours are evenly spaced with $\Theta \in [-0.5, 0.5]$.

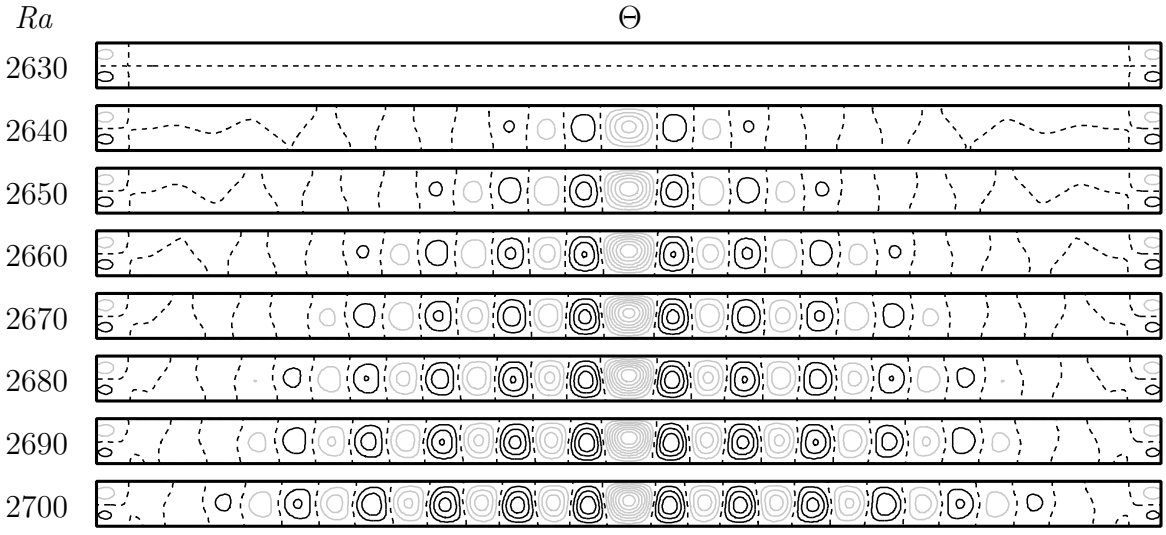

Figure 3.6: Snap-shots in a meridional plane of Θ for pulsed target states, all at the same phase of the imposed modulation, at $A = 0.05$ and $\Omega_0 = \Omega_m = 23.6$ for Ra as indicated. Ten contours are evenly spaced with $\Theta \in [-0.5, 0.5]$.

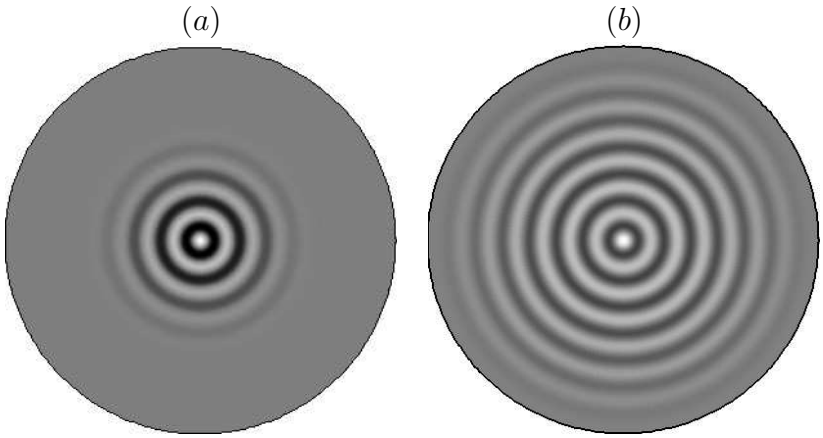

Figure 3.7: Snap-shots of isotherms at mid-height for axisymmetric pulsed target patterns at (a) $Ra = 2840$ and $A = 0.18$, and at (b) $Ra = 2700$ and $A = 0.05$, both with $\Omega_0 = \Omega_m = 23.6$ (ten forcing periods of the $Ra = 2700$ pattern are shown in movie 2 in the online version).

correspond to reflecting those in figures 3.5 and 3.6 about the mid-height $z = 0$ and changing the sign of Θ, i.e. applying the action of K_z. Figure 3.7 shows snap-shots of the isotherms at the mid-plane $z = 0$ of two target states with warm cores at $\Omega_0 = \Omega_m = 23.6$, and $Ra = 2840$, $A = 0.18$ and $Ra = 2700$, $A = 0.05$. The synchronous pulsation and lack of net radial movement is illustrated in movie 2 in the online version, which shows the pulsed target pattern state from figure 3.7(b) over ten modulation periods.

The development with A of the radial velocity of pulsed target patterns at $\Omega_0 = \Omega_m = 23.6$ and $Ra = 2680$ is illustrated in figure 3.8. The state at $A = 0$ is the steady target pattern of the axisymmetric subspace of the unmodulated problem (which is unstable to the KL state). It is evident that the action of the oscillatory Stokes layers is stronger for larger r and that the Stokes layers tend to quench the convective rolls from the sidewall to smaller and smaller radii as A increases. For large enough A, the pulsed target patterns are completely quenched at the pitchfork bifurcation and the

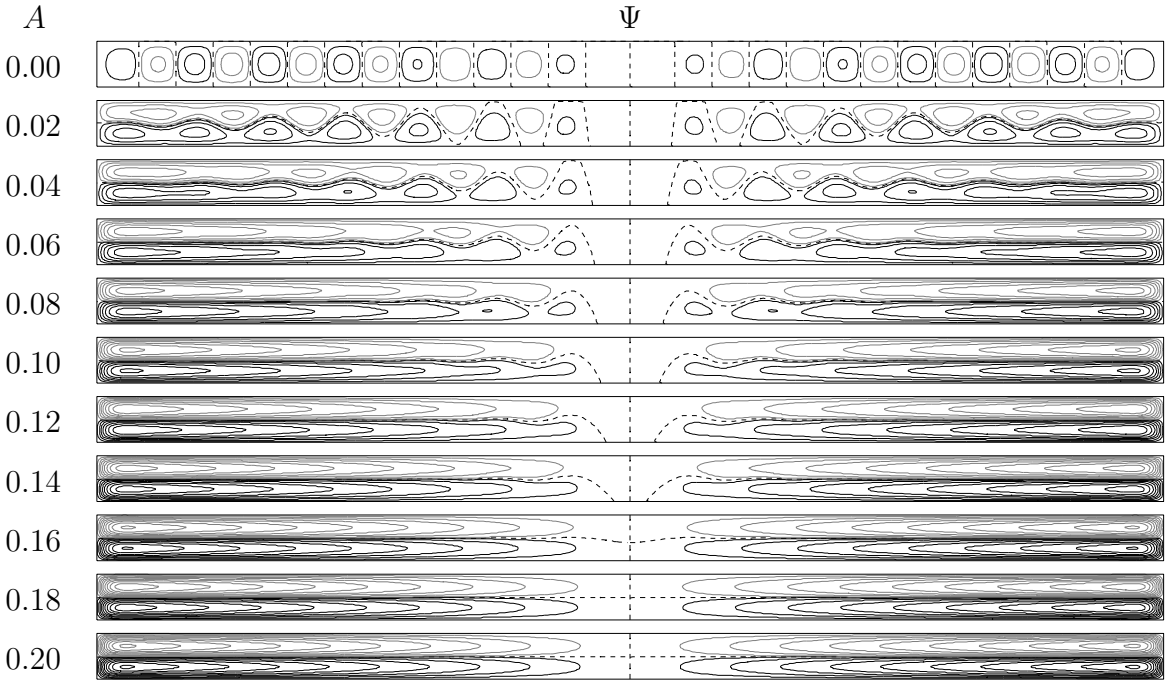

Figure 3.8: Snap-shots in a meridional plane of stream function for pulsed target states, all at the same phase of the imposed modulation, at $Ra = 2680$, $\Omega_0 = \Omega_m = 23.6$ and A as indicated. Ten contours are spaced quadratically with $\Psi \in [-5, 5]$.

basic state is stabilized. In figure 3.8, this stabilized basic state is shown at $A = 0.2$.

The pitchfork bifurcation (using Ra as the bifurcation parameter) is illustrated in figure 3.9(a) for $\Omega_0 = \Omega_m = 23.6$ at two values of A: (a) $A = 0.05$ and (b) $A = 0.18$. The measure of the flow state used in these bifurcation diagrams is $\Theta_m(0)$, the mid-point temperature strobed at a particular phase in the modulation (corresponding to $t = 0$). For $Ra < Ra_c(A, \Omega_0, \Omega_m)$, the basic state (dashed line at $\Theta_m(0) = 0$) is stable, and for $Ra > Ra_c$ it is unstable. At $Ra = Ra_c$, two branches of pulsed target patterns emerge at the pitchfork bifurcation as the K_z symmetry is broken, one with a hot plume rising at the axis ($\Theta_m(0) > 0$) and the other with a cold plume descending at the axis ($\Theta_m(0) < 0$). For these states, $\Theta_m(t)$ has a small amplitude oscillation synchronous with the imposed modulation, as illustrated in figure 3.10.

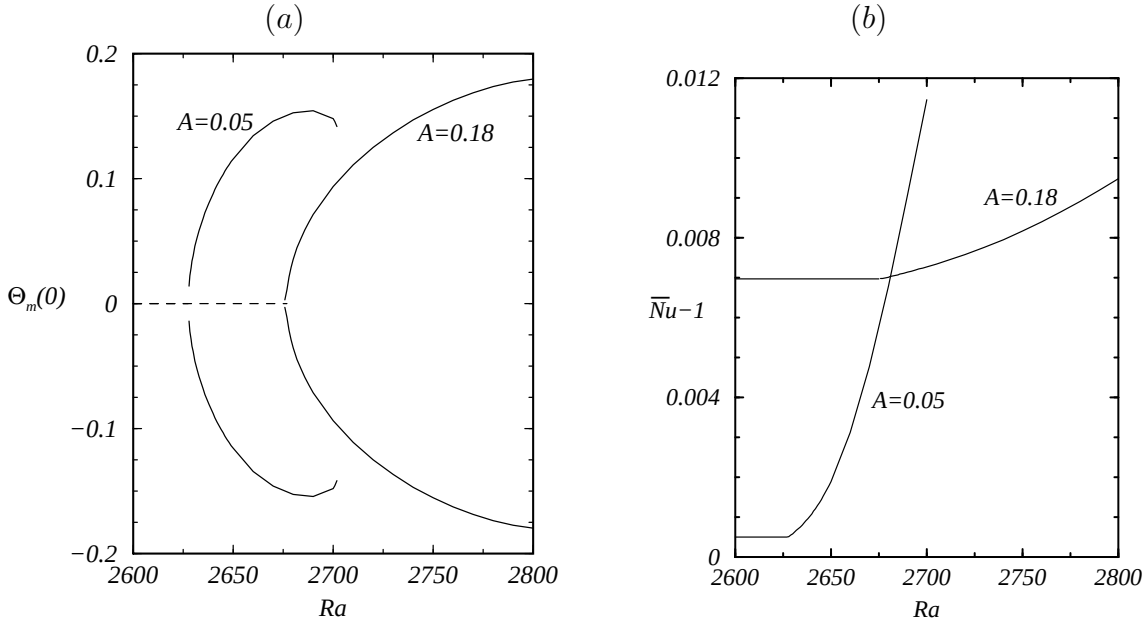

Figure 3.9: (a) Bifurcation diagrams at $\Omega_0 = \Omega_m = 23.6$ for $A = 0.05$ and $A = 0.18$, together with (b) the corresponding variations of $\overline{Nu} - 1$ with Ra.

The close-up in figure 3.10(b) details this oscillation and shows the phase at which the solution is strobed, $P^n(\Theta_m)$, used in figure 3.9 and in subsequent analyses. The heat transfer properties of these states can be seen in figure 3.9(b), showing the time-averaged Nusselt number values, $\overline{Nu}$, corresponding to figure 3.9(a). Notice that the $\overline{Nu}$ curve changes slope (it increases discontinuously) at the bifurcation point, so the slope of the $\overline{Nu}(Ra)$ curve can also be used for the determination of the bifurcation point.

Traveling target pattern: The SNIC bifurcation

With increasing Ra for $A \geq 0.04$ or increasing A for $Ra \geq 2700$, the pulsed target patterns give way to the traveling target patterns which are distinguished by being quasiperiodic. Figure 3.10 shows $\Theta_m(t)$ for the two K_z-conjugate pulsed target patterns at $\Omega_0 = \Omega_m = 23.6$, $A = 0.05$ and $Ra = 2700$ (approximately straight lines at

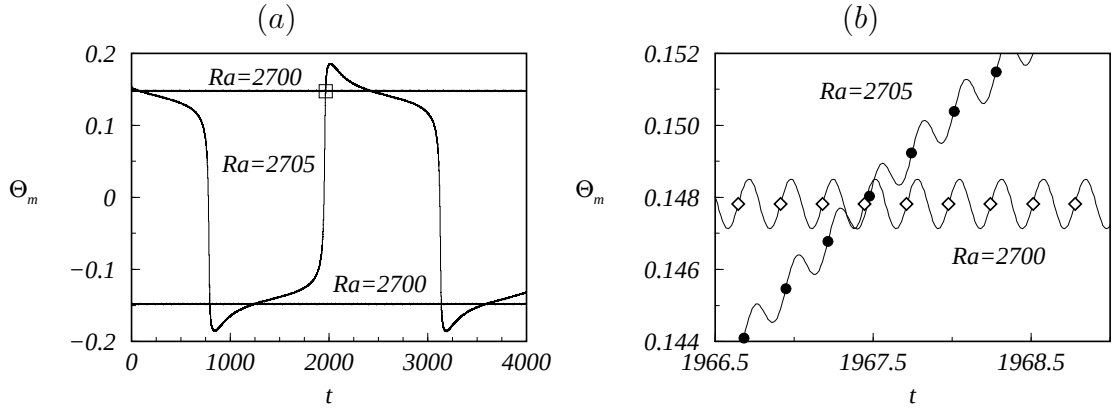

Figure 3.10: Time series of Θ_m at $\Omega_0 = \Omega_m = 23.6$, $A = 0.05$ and $Ra = 2700$ and 2705. The solutions at $Ra = 2700$ are K_z-conjugate pulsed target patterns and the solution at 2705 is a traveling target pattern. The box where the two curves cross at about $t = 1967$ is the close-up in (b) which includes a Poincaré strobing $P^n(\Theta_m) = \Theta_m(n\tau_m)$, n integer, of these solutions shown as symbols superimposed on the continuous $\Theta_m(t)$.

$\Theta_m \pm 0.15$) and the traveling target pattern state at the same Ω_0, Ω_m and A but at slightly larger $Ra = 2705$ (curved line). The traveling target pattern has a very low frequency Ω_w in addition to the imposed modulation frequency Ω_m. The ratio of the corresponding periods for the traveling target pattern state shown in figure 3.10(a) is $\tau_w : \tau_m \approx 8800$. The periods of these traveling wave states diverge as onset is approached from above, making it clear that the traveling target pattern solutions emerge at an infinite period bifurcation.

Strobing the traveling target patterns with the Poincaré map P reveals the new second period, which corresponds to the time, τ_w, for the target pattern to repeat itself as the rolls recede in towards the axis. Figure 3.11(a) shows reconstructed phase portraits using delays, $\big(P^n(\Theta_m), P^{n+100}(\Theta_m)\big)$, of states at $\Omega_0 = \Omega_m = 23.6$ and $A = 0.18$ at various Ra. The basic state is a fixed point at the origin and the pulsed target patterns are symmetrically-related fixed points along the diagonal (since

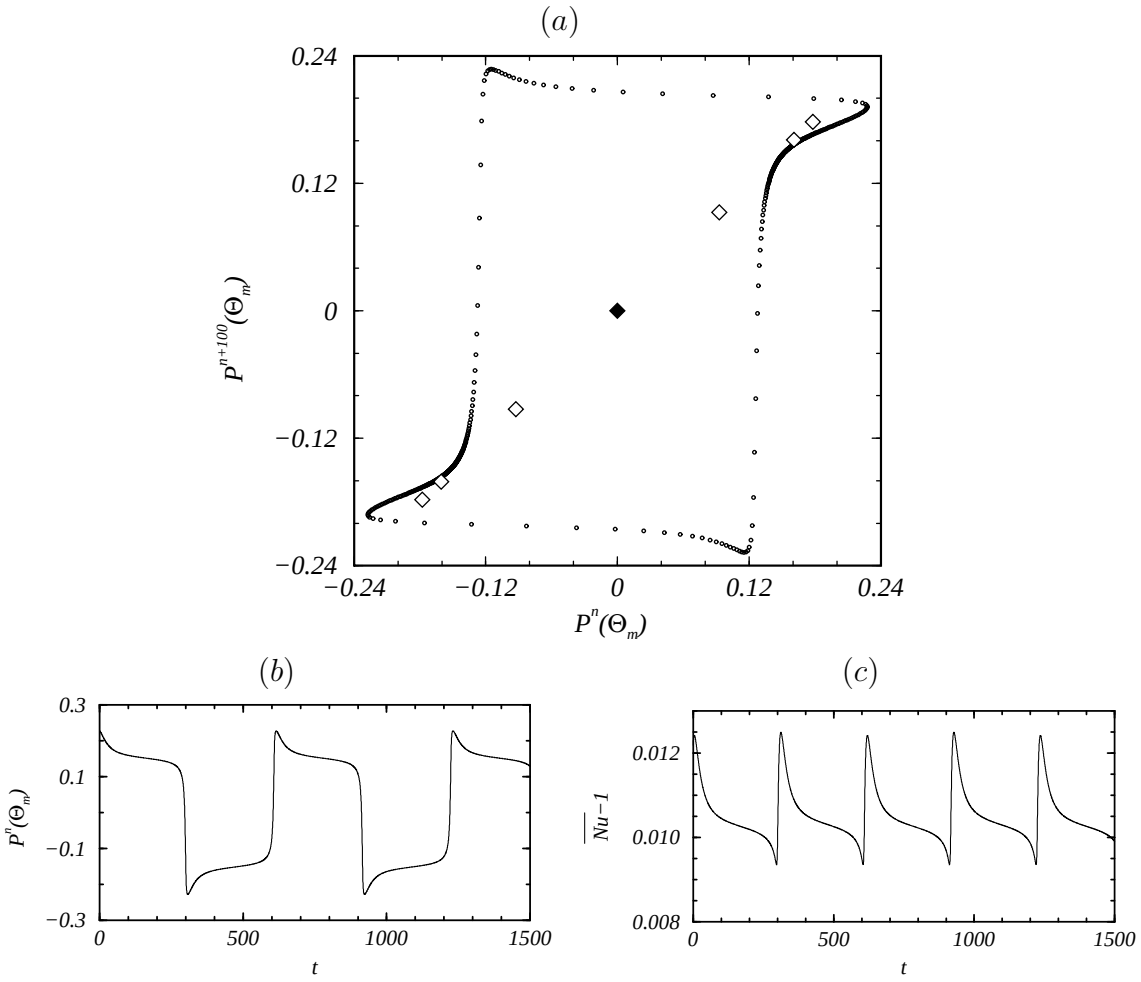

Figure 3.11: (a) Reconstructed phase portraits using delays, $\left(P^n(\Theta_m), P^{n+100}(\Theta_m)\right)$, of the basic state (filled diamond at the origin), pulsed target patterns (open diamonds) for $Ra = 2700$, 2760 and 2820, and one traveling target pattern (dots) at $Ra = 2844$, all for $\Omega_0 = \Omega_m = 23.6$ and $A = 0.18$. For visual clarity only every fourth iterate of the Poincaré map over one period of the traveling target pattern is shown ($\tau_w = 2312\tau_m$ in this case). Time series of (b) $P^n(\Theta_m)$ and (c) $\overline{Nu} - 1$ for the traveling target pattern state in (a).

the pulsed target pattern is a fixed point of P). The phase portrait of the traveling target pattern at $Ra = 2844$ consists of open circles drawn every fourth iterate of P over one period τ_w. The τ_w-oscillation is of a slow-fast nature, where the oscillation slows significantly in the neighborhood of the ghosts of the pulsed target patterns that were present at slightly lower Ra. The traveling target pattern in figure 3.11(a) is symmetric to a half turn, indicating that the K_z-symmetry has been restored in the infinite period bifurcation (which the following results identify as a SNIC). Moreover, the traveling target pattern shows a weaker slowing down at two additional points in between the ghosts of the pulsed target patterns, and the traveling target pattern is close to being symmetric by a 90° rotation. This reflects the fact that the problem has an exact $Z_2 \times Z_2$ symmetry when the mean rotation is zero ($\Omega_0 = 0$).

Figure 3.11(b) shows the discrete Poincaré orbit $P^n(\Theta_m)$ (at the discrete times $t = n\tau_m$) for the traveling target pattern in figure 3.11(a), while (c) shows the corresponding $\overline{Nu} - 1$ time series. The period of $\overline{Nu} - 1$ is half the period of $P^n(\Theta_m)$. This is because the two halves of the period in $P^n(\Theta_m)$ correspond to K_z-symmetric states (see figure 3.13), and therefore have the same value of $\overline{Nu}$, as explained in §5.2.

Further away from onset, the secondary oscillations in the traveling target patterns (corresponding to their radial drift) take on more of a uniform oscillator character, but this drift is still very slow compared to the imposed modulation. The space-time diagrams in figure 4.12 show $P(\Theta)$ at the midplane over 2500 viscous time units corresponding to $9400\tau_m$; this is equivalent to almost 9 hours in the laboratory experiments conducted in (Thompson *et al.*, 2002). Very near the SNIC curve (case a), the traveling target pattern remains essentially unchanged for a long time (about $4500\tau_m$) resembling one of the pulsed target patterns, then rapidly evolves to a state resembling the corresponding K_z-conjugate state. In case b, the state is a little further removed from the SNIC curve so that the rolls drift radially inward faster, but the

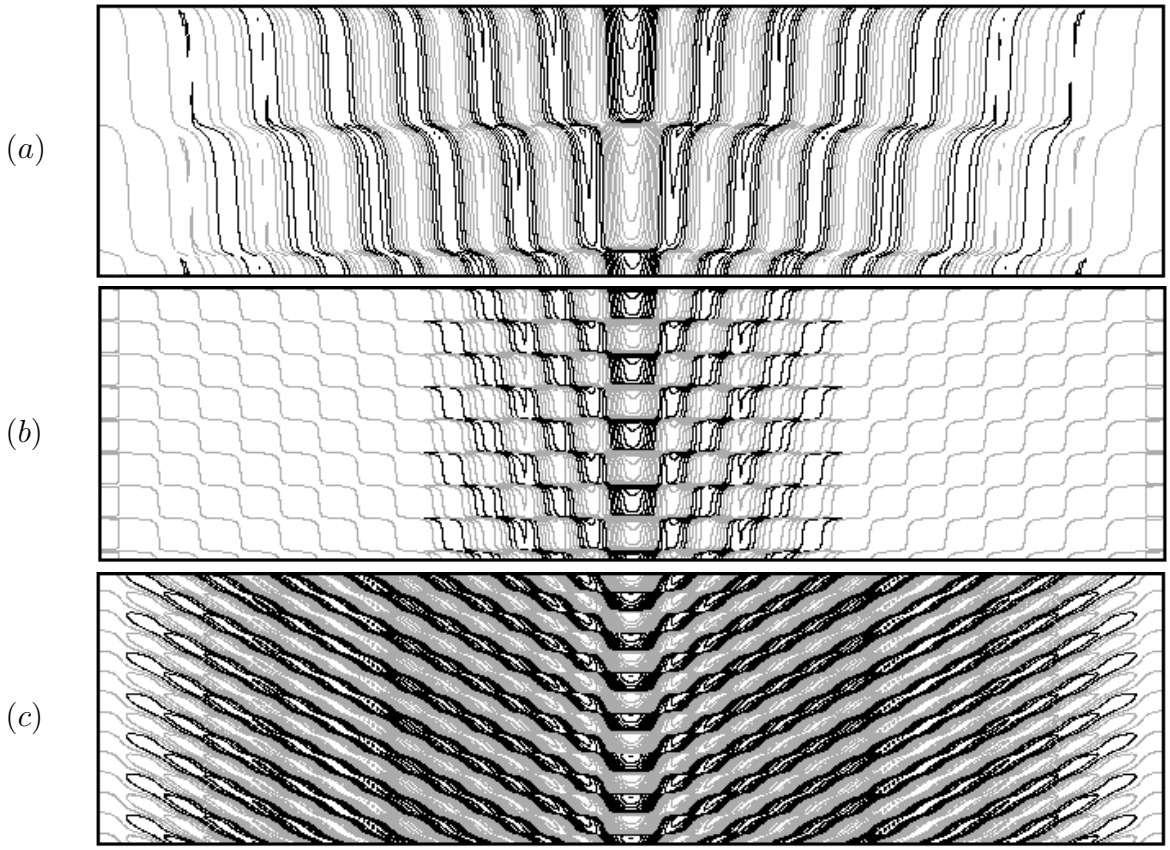

Figure 3.12: Space-time plot of traveling target states at $\Omega_0 = \Omega_m = 23.6$ for various Ra and A, showing Θ at $z = 0$ with time running from top to bottom over 2500 viscous times. In (a) $Ra = 2705$ and $A = 0.05$, (b) has $Ra = 2844$ and $A = 0.18$ and (c) has $Ra = 2840$ and $A = 0.06$. Movies 3, 4 and 5 in the online version show these three states over several τ_w periods strobed at τ_m.

slow-fast characteristics are still evident. In case c, the state is even further away from the SNIC curve and the τ_w oscillations are faster and more uniform. Note that case b is at relatively large Ra and A, and so the sidewall jet driven by the modulation quenches the rolls near the sidewall to a much greater extent than in case c at relatively smaller Ra and A. Movies 3, 4 and 5 in the online version show these three states over several τ_w periods strobed at τ_m.

Figures 3.13 and 3.14 show eight snapshots equally spaced over the traveling wave

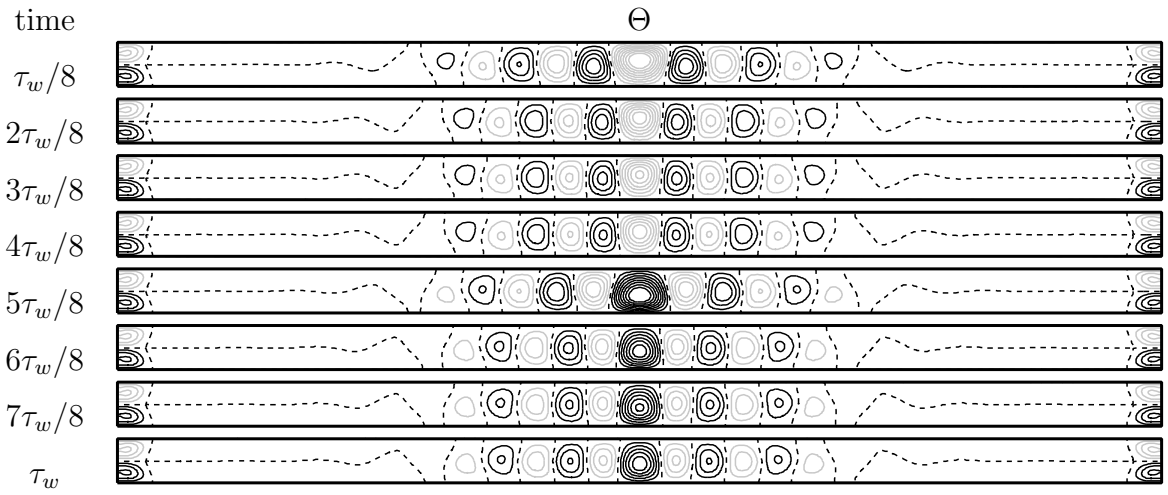

Figure 3.13: Contours of temperature deviation in a meridional plane ($r \in [-\gamma, \gamma], z \in [-0.5, 0.5]$) over one period of the traveling target pattern at $Ra = 2844$, $\Omega_0 = \Omega_m = 23.6$ and $A = 0.18$, the same solution as shown in figure 4.12(b). Five contours are shown linearly spaced between -0.2 and 0.2.

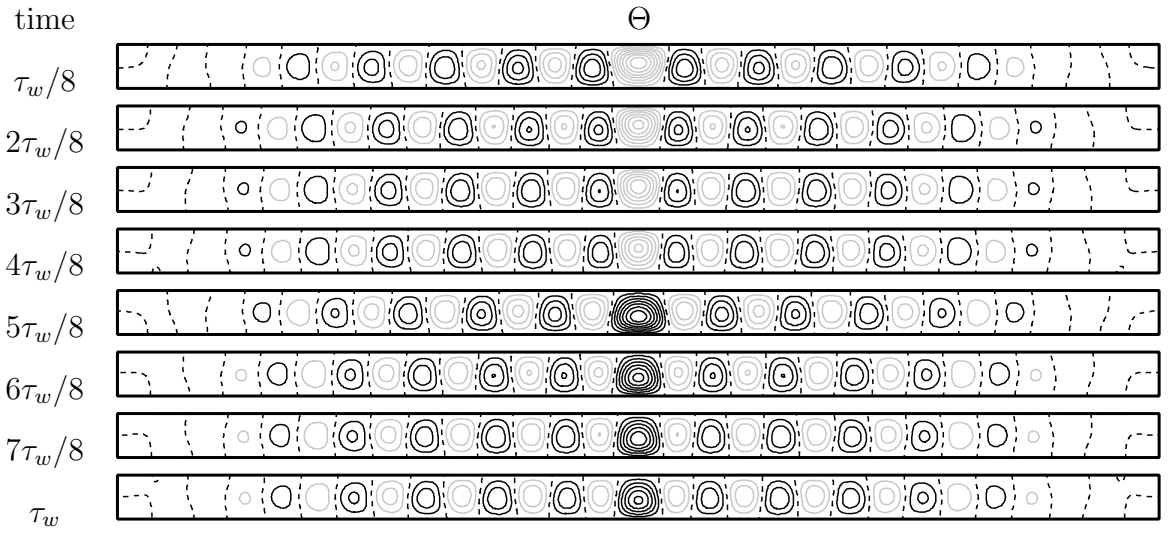

Figure 3.14: Contours of temperature deviation in a meridional plane ($r \in [-\gamma, \gamma], z \in [-0.5, 0.5]$) over one period of the traveling target pattern at $Ra = 2705$, $\Omega_0 = \Omega_m = 23.6$ and $A = 0.05$, the same solution as shown in figure 4.12(a). Eight contours are shown linearly spaced between -0.2 and 0.2.

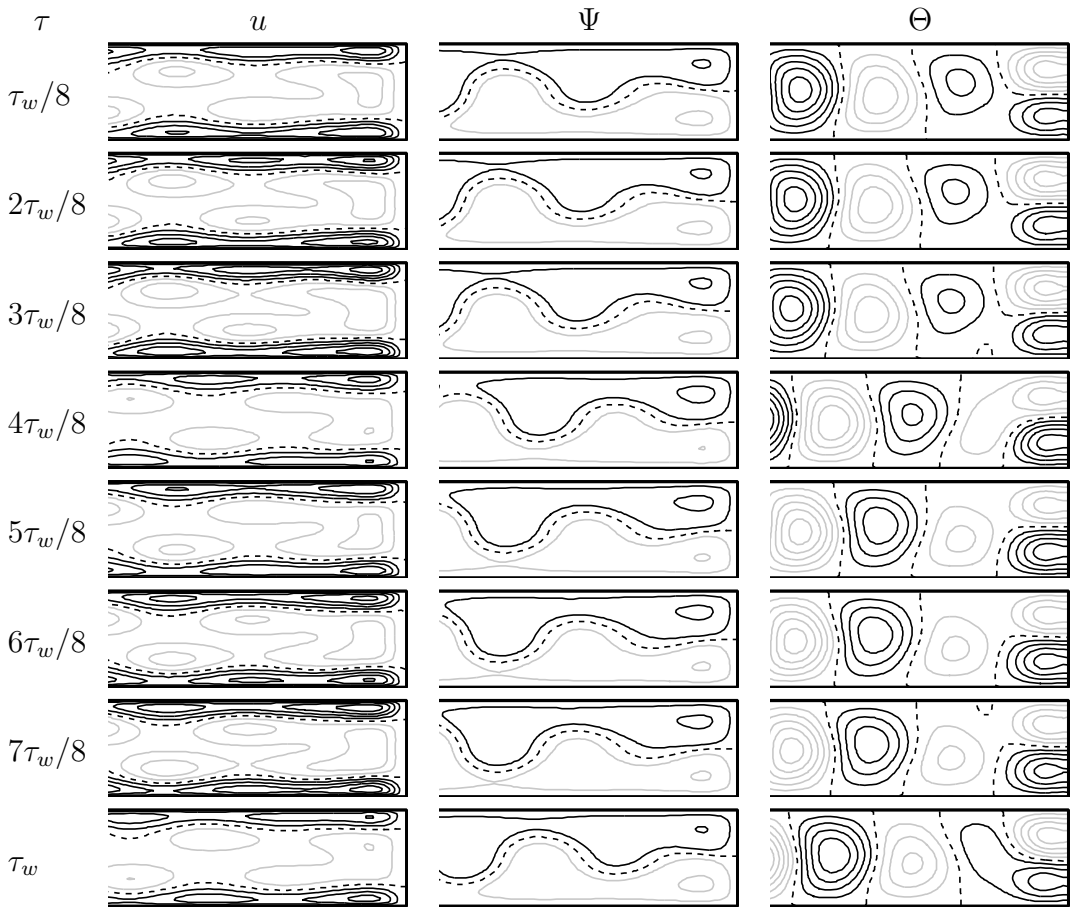

Figure 3.15: Snapshots of u, Ψ and Θ, all at the same phase of the imposed modulation in a meridional plane ($r \in [0.74\gamma, \gamma], z \in [-0.5, 0.5]$) over one period τ_w at $Ra = 2705$, $\Omega_0 = \Omega_m = 23.6$ and $A = 0.05$. Five contours are quadratically spaced for $\Psi \in [-0.25, 0.25]$ and linearly spaced for $\Theta \in [-0.025, 0.025]$ and $u \in [-10, 10]$.

period τ_w at the same phase in the imposed τ_m modulation. Figure 3.13 shows a large $A = 0.18$ case in which the strong Stokes layers have suppressed the convection rolls away from the axis region, and the modulation-driven cells at the corners provide nontrivial heat exchange at the sidewall. This is the same solution as shown in figure 4.12(b). Far from the axis there are weak concentric ring plumes that emerge up to several d from the sidewall, gaining strength as they drift toward the axis. At the axis, the innermost plume weakens and disappears entirely before being replaced

by the adjacent roll. Figure 3.14 shows an $A = 0.05$ case in which the traveling target pattern fills the whole cell. This is the same solution as shown in figure 4.12(a). The sidewall jet perturbs the nearby velocity and temperature fields, resulting in small inward and outward motions of the outermost cells as well as a mechanically driven heat transport. Both take place on the τ_m timescale, as do those in the nearby pulsed target pattern illustrated in figure 3.4. Close-ups of the radial velocity and Θ near the sidewall region for this case are shown in figure 3.15. The sequence shown in figure 3.15 is over the much slower τ_w time scale ($\tau_w \approx 8800\tau_m$), and each frame is taken at the same phase in the τ_m modulation. This is why the relatively hot (cold) cell is always at the top (bottom) corner in these figures. During the τ_w cycle, the concentric rolls making up the target pattern drift radially inward. A new roll is formed as the void left by the outermost receding roll is filled by relatively warm (cool) fluid seeping out from the bottom (top) corner cell each half τ_w period. The modulation-driven Stokes layers and the corresponding mid-plane jet (all characterized by the radial velocity) do not appear to play a significant role in the drift dynamics at the τ_w time scale, although their action on the τ_m time scale continues to be essentially the same as for the pulsed target patterns described earlier.

Figure 3.16(a) shows the variation of τ_w for different Ra with $A = 0.18$ and $\Omega_0 = \Omega_m = 23.6$. As $Ra \to Ra_{\mathrm{SNIC}}$ from above, $\tau_w \to \infty$ following the $1/\sqrt{(Ra - Ra_{\mathrm{SNIC}})}$ scaling associated with the saddle-node on an invariant circle (SNIC) bifurcation. Figure 3.16(b) shows the variation of τ_w with respect to A for $Ra = 2958$, $\Omega_0 = 19.7$ and various Ω_m.

In general, a SNIC bifurcation consists of a saddle-node bifurcation taking place on a limit cycle, as shown schematically in figure 3.17(a). Before the bifurcation (left diagram), the period of the limit cycle tends to infinity as the bifurcation is approached, and the periodic solution spends more and more time near the place where

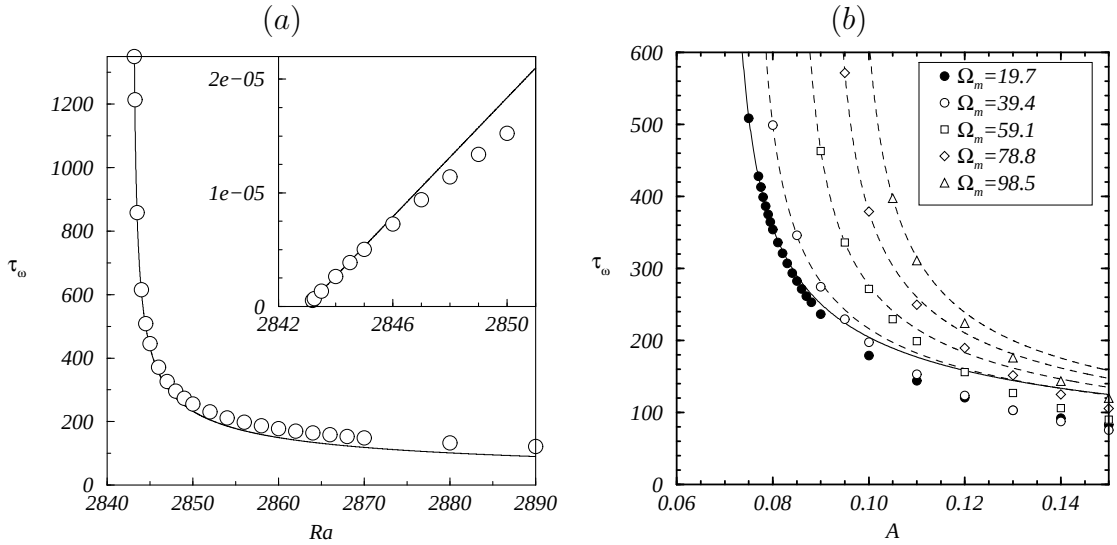

Figure 3.16: Variation of τ_w (a) with Ra for $A = 0.18$ and $\Omega_0 = \Omega_m = 23.6$, and (b) with A for $Ra = 2958$, $\Omega_0 = 19.7$ and Ω_m as indicated. The symbols are numerical estimates and the curves are fits to the first four data points for each Ω_m set of the form $\tau_w = a/\sqrt{(Ra - Ra_{\rm SNIC})}$. The inset in (a) is $\tau_w^{-2}(Ra)$.

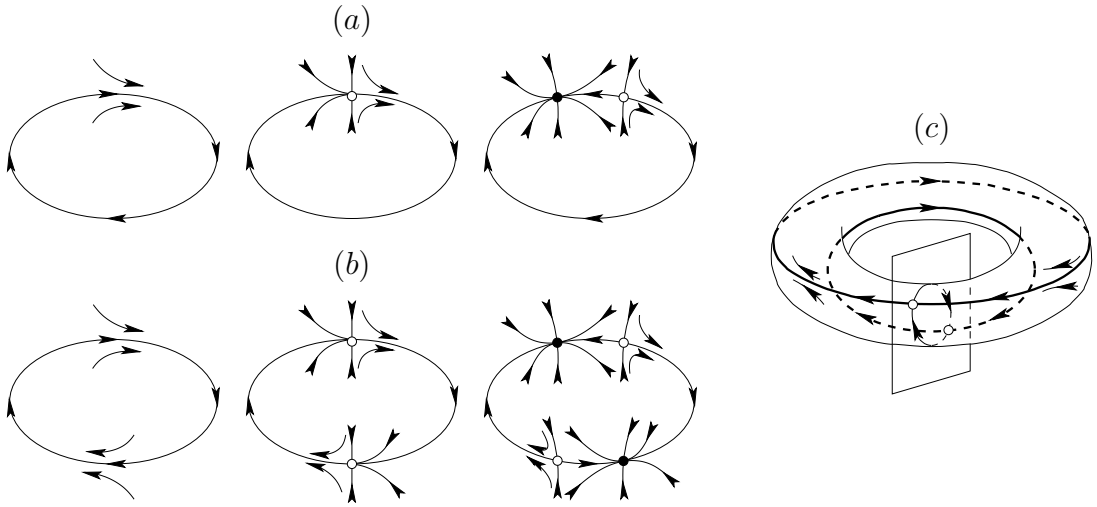

Figure 3.17: Schematic of the SNIC bifurcation on an invariant circle in (a) a generic system, and (b) a Z_2-symmetric system; left, central and right diagrams correspond to before, during and after the SNIC bifurcation. (c) Schematic of the SNIC bifurcation on an invariant two-torus; the planar section (a Poincaré section) corresponds to case (b) center.

the saddle-node will appear. The periodic solution becomes a homoclinic orbit at the bifurcation point (central diagram). After the bifurcation the periodic solution no longer exists and there remains a pair of fixed points, one a saddle (unstable, hollow in the figure) and the other a node (stable, solid in the figure), and stable and unstable manifolds connecting them. This is a codimension-one bifurcation (Kuznetsov, 2004). In the presence of a Z_2 symmetry, if the limit cycle is not pointwise Z_2-invariant, a pair of saddle-nodes appear simultaneously on the invariant circle, as shown schematically in figure 3.17(b). This is what happens in our problem, but instead of a limit cycle we have quasi-periodic solutions (a two-torus), as depicted schematically in figure 3.17(c). In this case the two saddle-nodes become saddle-nodes of limit cycles; the two Z_2-symmetric saddle-nodes at the bifurcation point are shown as thick lines. Analogous Z_2-symmetry breaking between rotating and modulated rotating waves in Taylor-Couette flow via a SNIC bifurcation has been computed and observed experimentally (Abshagen *et al.*, 2005a,b). In the Poincaré section of a quasiperiodic solution (the planar section of the two-torus in figure 3.17c), the bifurcation occurs as a Z_2-symmetric collision of saddle-nodes shown in figure 3.17(b). The invariant circle C on the Poincaré section is K_z invariant as a set; i.e. given a point $a \in C$, $Pa \in C$ although $a \neq Pa$. The continuous quasiperiodic solution starting at a becomes a discrete orbit on C made of the iterates of a under P $(a, Pa, P^2a, P^3a, \ldots)$. This discrete orbit densely fills C when τ_w/τ_m is not rational (the generic case) and in this case the K_z reflections of the iterates do not belong to the discrete orbit, i.e. the discrete orbit is not K_z invariant. This is clearly illustrated in figure 3.11(a), where we have plotted every fourth iterate of P over one period τ_w. These iterates are on the invariant circle C, and almost fill it near the ghosts of the saddle nodes. If we keep iterating P, the result would be the invariant circle C.

When $\tau_w/\tau_m = p/q$ is rational, the solution is strictly periodic, of period $q\tau_w =$

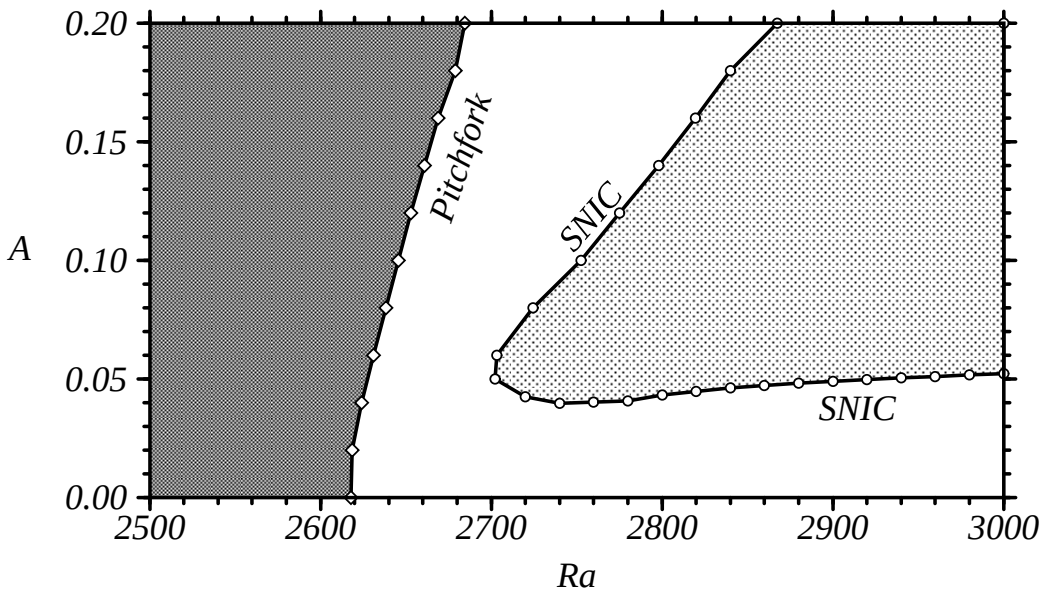

Figure 3.18: Regime diagram for $\Omega_0 = \Omega_m = 23.6$, showing the pitchfork and SNIC bifurcation curves. States in the different regions: modulated basic state (dark grey), pulsed target patterns (white), and traveling target patterns (light grey).

$p\tau_m$, and if p is even, the discrete orbit is K_z invariant, i.e. applying K_z is the same as advancing in time by the half period $\tau_w/2$. Therefore, in this case, the solution is invariant under a space-time symmetry consisting of applying K_z and advancing in time by half the travelling wave period. In the case illustrated in figure 3.11(a), there are approximately 6000 iterates of P in a traveling wave period τ_w, and so $K_z a$ plus a $\tau_w/2$ advance in time is very close to an iterate of P, and the space-time symmetry is very nearly satisfied, as can be seen in figures 4.12, 3.14 and 3.15.

In the continuous time system, the bifurcation occurs as a Z_2-symmetry-restoring SNIC on an invariant two-torus, as illustrated in figure 3.17(c). By measuring τ_w near onset for assorted values of (Ra, A) and applying the scaling law, the location of SNIC bifurcation curve shown in figure 3.18 was estimated. To the left of the pitchfork bifurcation curve (dark grey in the figure), the basic state is stable, to the

right (white in the figure) the pair of K_z-conjugate pulsed target patterns are stable, and beyond the SNIC bifurcation curve (light grey in the figure) the traveling target pattern is stable.

3.4 Discussion and conclusions

The spatio-temporal chaos associated with Küppers–Lortz instability in rotating convection can be greatly mitigated by small amplitude, high frequency modulations of the rotation rate, as observed experimentally by Thompson *et al.* (2002). In this paper, we have investigated the responsible mechanisms by employing simulations of the Navier–Stokes–Boussinesq equations with the corresponding physical boundary conditions, and analyzed the nonlinear solutions with the aid of equivariant bifurcation theory. The imposed modulation drives Stokes layers at the top and bottom endplates of the cylinder. The flow in these Stokes layers is fed into the interior by the presence of the cylinder sidewall, where a radial jet forms at mid-height. These oscillatory Stokes layers and jet tend to quench instabilities to three-dimensional flow, and as observed experimentally, axisymmetric target pattern states result. The main dynamic role of the modulation is to drive the system toward the axisymmetric subspace, but the subsequent dynamics of the axisymmetric states is apparently decoupled from the modulations. The use of a stroboscopic map restricts the analysis of the dynamics to a Poincaré section which is transverse to the modulations and provides a clearer picture of the dynamics. In the Poincaré section, the modulated basic state is a Z_2 reflection symmetric fixed point that first loses stability at a pitchfork bifurcation, breaking the Z_2 symmetry, where a pair of pulsed target pattern states are born. These are also fixed points in the Poincaré section and are Z_2 reflections of each other. They lose stability at a saddle-node on an invariant circle (SNIC) bifurcation, which results in the birth of the traveling target pattern state

that motivates this study. The new frequency introduced by this bifurcation goes to zero at onset and corresponds to the time scale associated with the slow drift of the concentric rolls radially inward. After the SNIC bifurcation, the quasiperiodic solution (traveling target pattern) lives on a two-torus, which is Z_2 reflection symmetric. The Poincaré section of the two-torus results in an invariant circle C, which is also Z_2 reflection symmetric. The traveling target pattern becomes a discrete orbit on the invariant circle, densely filling it (except when the two frequencies are commensurate). As the two-torus and the invariant circle C are K_z reflection symmetric, the SNIC bifurcation is a symmetry-restoring bifurcation. However, individual solutions are not K_z-symmetric, but in many cases, and in particular close to the SNIC bifurcation, the K_z-symmetry is very approximately satisfied, taking the form of a space-time symmetry: advancing half the traveling wave period and applying the K_z-symmetry leaves the solution invariant.

The mechanism for the onset of the traveling target patterns was not identified in the experimental study (Thompson *et al.*, 2002) and the Swift–Hohenberg (SH) amplitude equations model (Roxin & Riecke, 2002) was unable to reproduce such traveling target patterns. They surmised that their model equations lacked some non-variational terms to permit such persistent dynamics. This SH model is two dimensional in (r, θ), and since the z-coordinate is absent, the model lacks any vertical information. By solving the full problem described by the Navier–Stokes equations incorporating the Boussinesq approximation, we were able to reproduce the traveling target patterns in the parameter regimes where they were observed experimentally, and having the same spatio-temporal characteristics as those observed experimentally. Our analysis of these solutions indicates that the breaking of the so-called Boussinesq symmetry (a Z_2 reflection symmetry) plays a crucial role in the drift dynamics. Roxin & Riecke (2002) included odd terms in their SH model in order to impose a generic

Z_2 invariance in their amplitude equation, which they claimed mimicked the Boussinesq symmetry. However, the amplitude equations lack any vertical information (the spatial differential operators are only horizontal), and the Z_2 invariance imposed in the SH model cannot have any relationship with the vertical reflection K_z ($z \to -z$). Furthermore, we have found that the transition to the traveling target patterns is a symmetry-restoring SNIC bifurcation where the resultant traveling target pattern inherits a spatio-temporal Z_2 symmetry from the pair of Z_2-related asymmetric pulsed target patterns which are annihilated at the SNIC bifurcation. So even though it is tempting to think of these states as essentially two-dimensional (horizontal (r, θ) patterns), their structure in the vertical direction is crucial in determining their dynamics. In particular, the manner in which the Boussinesq symmetry is broken and then restored as a spatio-temporal symmetry holds the key to understanding the onset of the traveling target patterns.

In the physical experiments (Thompson *et al.*, 2002) and in the Swift–Hohenberg amplitude equations model (Roxin & Riecke, 2002) of the modulated rotating convection problem, when the initial condition before the modulation is imposed was a KL state, the modulations generically result in imperfect spiral patterns. In order to obtain axisymmetric target patterns, both the experiments and the SH model needed to generate these "with care," using convoluted initial conditions, etc. However, once a target pattern was obtained, it persisted for long times. Our results are consistent with these observations, in that if we start with a KL state and then start modulating the rotation, the flow evolves to an imperfect spiral state. When we computed in the axisymmetric subspace however, the target patterns are obtained. If we add a small non-axisymmetric perturbation to the target patterns it takes a long time (depending on the magnitude of the perturbation) for the perturbation to grow, but they do grow. Our preliminary indications are that the target patterns may not be stable to three-

dimensional perturbations. In fact, in the limit of vanishing modulation ($A \to 0$), the stable state is the three-dimensional KL state. Therefore if the target patterns are stable when $A \neq 0$, there must be a critical A below which the target patterns are unstable. To address the stability of the target patterns to three-dimensional perturbations is not trivial. One needs to compute the time-periodic axisymmetric target pattern state (which we have done in this paper) and then perform a Floquet stability analysis to general three-dimensional perturbations, which is beyond the scope of this paper. Very closely related is also the question of whether the spiral patterns or the target patterns bifurcate first from the modulated basic state as Ra is increased, for a given modulation $A \neq 0$.

In summary, the effects of harmonic modulations on rotating convection have been investigated numerically, and the numerical solutions have been analyzed using bifurcation-theoretical techniques and in particular equivariant dynamical systems theory. The role of symmetry-breaking in the SNIC bifurcation is central to understanding the onset of the traveling target patterns, a phenomenon which had remained completely unexplained up to now.

Chapter 4

Interacting oscillatory boundary layers and wall modes in modulated rotating convection

In the previous chapter concerned a case in which a nontrivial interaction between the oscillatory boundary layers arising from modulating the rotation rate interacted with the thermally driven convective flow to stabilized the axisymmetric subspace resulting in solutions with inwardly travelling axisymmetric rolls. While the previous work shed much light on the nature of the interaction between bulk modes in rotating convection and oscillatory boundary layers it was clear that flow driven by the oscillatory boundary layers was strongest near the sidewall. In order to focus on the flow near the sidewall a study was conducted of a region in parameter space for which the onset of convection occurs as a wall-localized rotating wave, subjecting the flow to small amplitude harmonic modulations of the rotation rate over a wide range of frequencies. This research was published as Rubio *et al.* (2009a) and is a joint work with Juan M. Lopez[1] and Francisco Marques[2]. The media cited in this chapter can be found at $http://mathpost.la.asu.edu/\sim rubio/JFM\_RLM07b\_media/jfm\_RLM07b.html$.

4.1 Introduction

Rayleigh-Bénard convection has long been a popular nonlinear system in which to study the effects of temporal forcing of the control parameters. Recently, there has been specific interest in how the system responds to a modulated rotation (Bhattacharjee, 1990; Niemela, Smith & Donnelly, 1991; Thompson, Bajaj & Ahlers, 2002). In the laboratory experiments of Thompson *et al.* (2002), the mean rotation rates were restricted to being small enough to ensure that in the unmodulated case the

[1]Department of Mathematics and Statistics, Arizona State University, lopez@asu.edu
[2]Departament de Física Aplicada, Universitat Politècnica de Catalunya, marques@fa.upc.edu

onset of convection was to a bulk mode rather than a wall mode (Ecke, Zhong & Knobloch, 1992; Goldstein, Knobloch, Mercader & Net, 1993). In numerically reproducing the experimental observations of Thompson *et al.* (2002), Rubio, Lopez & Marques (2008) showed that the oscillatory boundary layers resulting from the modulation greatly affect the Küppers–Lortz spatio-temporal chaos associated with the onset of bulk convection (Küppers & Lortz, 1969; Herrmann & Busse, 1993; Kuo & Cross, 1993; Knobloch, 1998; Bodenschatz, Pesch & Ahlers, 2000), leading to the experimentally observed spiral and target patterns, even for small amplitude modulations. The secondary flows associated with the oscillatory boundary layers were found to be strongest near the cylinder sidewall, and it is natural to ask how these boundary layers interact with the much simpler case of wall-localized convection found near onset at higher mean rotation rates.

Preliminary numerical experiments showed that modulations of the rotation rate could delay the onset of thermal convection to thermal forcing levels well beyond those required in the unmodulated case. Or, to put it another way, with modulated rotation the three-dimensional wall modes could be driven to an axisymmetric state with a greatly reduced heat flux, a behaviour we refer to as quenching. The focus of the present study is the examination of how the wall modes are quenched as a function of modulation amplitude and modulation frequency. For the most part, we hold the thermal forcing constant to see how a single initial wall mode state either persists or is driven to a state without thermal convection. This focused approach permits an extensive survey of modulation amplitudes and modulation frequencies and led to the discovery of a wide band of modulation frequencies which quenches thermal convection at even quite modest modulation amplitudes of less than 1% of the mean rotation rate. Particular attention is given to the interaction between the wall modes of convection and the modulation-driven boundary layers, whose nature

changes considerably at high background rotation rates. The modulation-driven secondary flow exists for all non-zero modulation amplitudes and grows in strength with increasing modulation amplitude and frequency. As such, it is surprising that the optimal modulation frequency for quenching thermal plumes is not associated with frequencies for which the secondary flow is strongest. In fact, at the highest frequencies considered the spatial structure of the thermal plumes remains intact for the range of modulation amplitudes considered. The structure of the mean component of the secondary flow is examined in detail and its interaction with the thermal plumes is discussed. The generation of a streaming flow driven by oscillatory viscous boundary layers is a common phenomenon in parametrically forced fluid dynamics, first elucidated by Schlichting (1932); also see the review article by Riley (2001). However, in those examples the streaming flow is normal to the direction of the oscillations. In our problem, the imposed oscillations are in the azimuthal direction and a meridional (normal to the azimuthal direction) streaming flow is also established, but so is a streaming flow in the azimuthal direction. Both streaming flows have important effects. The azimuthal streaming flow decreases the precession rate of the wall modes at high frequency, while the meridional streaming flow drives a non-trivial mean temperature perturbation at the frequencies where the quenching takes place.

The layout of the paper consists of a description of the governing equations, boundary and initial conditions, and the spectral method used to solve them in §2. A brief overview of wall mode convection in rotating cylinders is presented in §3 in order to provide a setting for the new results due to the harmonic modulation, presented in §4. Section 4 consists of a number of subsections; §4.1 presents the main motivating observation for the paper – the quenching of the wall modes with a small amplitude modulation at intermediate frequencies. Section §4.2 explores the physical mechanism responsible for the quenching – the action of the oscillatory boundary layers – in a

regime where the wall modes are not present. Finally, §4.3 examines the structure and behaviour of the modulated wall modes, the states that result from the competition between the wall-localized thermal convection and the modulation-driven flow in regimes where the thermal convection is not quenched.

4.2 Governing equations and numerical technique

Consider the flow in a rotating circular cylinder, with no-slip boundary conditions, of radius r_0 and depth d, with a modulated angular frequency $\omega(t^*) = \omega_0 + \omega_1 \sin(\omega_m t^*)$, where t^* is dimensional time. The endwalls are maintained at constant temperatures, $T_0 - \Delta T/2$ at the top and $T_0 + \Delta T/2$ at the bottom, and the sidewall is insulating. The Boussinesq approximation is implemented, treating all fluid properties as constant except for the density in the gravitational term, which varies linearly with temperature. The centrifugal buoyancy (Lopez *et al.*, 2006*b*; Marques *et al.*, 2007) is ignored in this study as the majority of related experiments in rotating convection have very small Froude number (typically $Fr = \omega_0^2 r_0/g < 0.025$, where g is the gravitational acceleration in the negative z-direction). Nevertheless, in any physical experiment $Fr \neq 0$ and so comparing the present results with experiments needs to be done with caution. The system is non-dimensionalized using d as the length scale, d^2/ν as the time scale (ν is the kinematic viscosity), $\nu^2\rho_0/d^2$ as the pressure scale (ρ_0 is the density at mean temperature T_0), and ΔT (the difference in temperature between the top and bottom) as the temperature scale. In a frame of reference rotating at the mean rotation rate ω_0, the non-dimensional governing equations are

$$(\partial_t + \mathbf{u}\cdot\nabla)\mathbf{u} = -\nabla p + \nabla^2\mathbf{u} + \frac{Ra}{\sigma}(\Theta - z)\mathbf{z} + 2\Omega_0\mathbf{u}\times\mathbf{z}, \tag{4.1}$$

$$(\partial_t + \mathbf{u}\cdot\nabla)\Theta = w + \sigma^{-1}\nabla^2\Theta, \qquad \nabla\cdot\mathbf{u} = 0, \tag{4.2}$$

where $\mathbf{u} = (u, v, w)$ is the velocity in cylindrical coordinates (r, θ, z), P is the dynamic pressure, $\mathbf{z}$ is the vertical unit vector in the z-direction and Θ is the temperature

deviation with respect to the conductive linear temperature profile; the relationship between Θ and the non-dimensional temperature T is given by

$$T = T_0/\Delta T - z + \Theta, \tag{4.3}$$

where $T_0/\Delta T - z$ is the conductive temperature profile.

There are six independent non-dimensional parameters:

Rayleigh number:	$Ra = \alpha g d^3 \Delta T/\kappa\nu$,
Coriolis number:	$\Omega_0 = \omega_0 d^2/\nu$,
Prandtl number:	$\sigma = \nu/\kappa$,
aspect ratio:	$\gamma = r_0/d$,
modulation amplitude:	$\Omega_1 = \omega_1 d^2/\nu$,
modulation frequency:	$\Omega_m = \omega_m d^2/\nu$,

where α is the coefficient of volume expansion, and κ is the thermal diffusivity. The boundary conditions (in a frame of reference rotating at the mean rotation rate ω_0) are:

$$\begin{aligned} r = \gamma: &\qquad \Theta_r = u = w = 0, v = \gamma\Omega(t) \\ z = \pm 0.5: &\qquad \Theta = 0,\ u = w = 0, v = r\Omega(t), \end{aligned}$$

where $\Omega(t) = \Omega_1 \sin(\Omega_m t)$ is the angular velocity of the cylinder in a reference frame rotating with the mean angular velocity Ω_0. To simplify the discussion, we introduce the relative modulation amplitude $A = \Omega_1/\Omega_0$ to allow for comparison between states with differing Ω_0. A will be used instead of Ω_1, except in the particular case when $\Omega_0 = 0$, as A is then not defined.

The governing equations and boundary conditions are invariant under arbitrary rotations through angle α about the axis, R_ϕ, whose action is

$$R_\phi(u, v, w, \Theta)(r, \theta, z, t) = (u, v, w, \Theta)(r, \theta + \phi, z, t). \tag{4.4}$$

They are also reflection-symmetric about the cylinder half-height. The action K_z of this so-called Boussinesq symmetry is

$$K_z(u, v, w, \Theta)(r, \theta, z, t) = (u, v, -w, -\Theta)(r, \theta, -z, t). \tag{4.5}$$

The symmetry group of the system is $G = SO(2) \times Z_2$, with $SO(2)$ generated by R_α and Z_2 by K_z.

The governing equations are solved using the second-order time-splitting of Hughes & Randriamampianina (1998), combined with a pseudo-spectral method for the spatial discretization, utilizing a Galerkin–Fourier expansion in the azimuthal coordinate θ and Chebyshev collocation in r and z. Following Orszag & Patera (1983), we have used the combinations $u_+ = u + iv$ and $u_- = u - iv$ in order to decouple the linear diffusion terms in the momentum equations. For each Fourier mode, the resulting Helmholtz equations for Θ, w, u_+ and u_- have been solved using a diagonalization technique in the two coordinates r and z. The coordinate singularity at the axis ($r = 0$) is treated following the prescription in Fornberg (1998), that guarantees the regularity conditions at the origin needed to solve the Helmholtz equations (Mercader, Net & Falqués, 1991).

The code has been validated on a number of convection problems in rotating cylinders (Lopez *et al.*, 2006*b*; Marques *et al.*, 2007; Lopez *et al.*, 2007; Rubio *et al.*, 2008), establishing resolution requirements over a wide range of parameters. For the cases considered in this paper, $n_r = 48$ and $n_z = 24$ Chebyshev modes in r and z, respectively, were employed. For cases where the solution is non-axisymmetric,

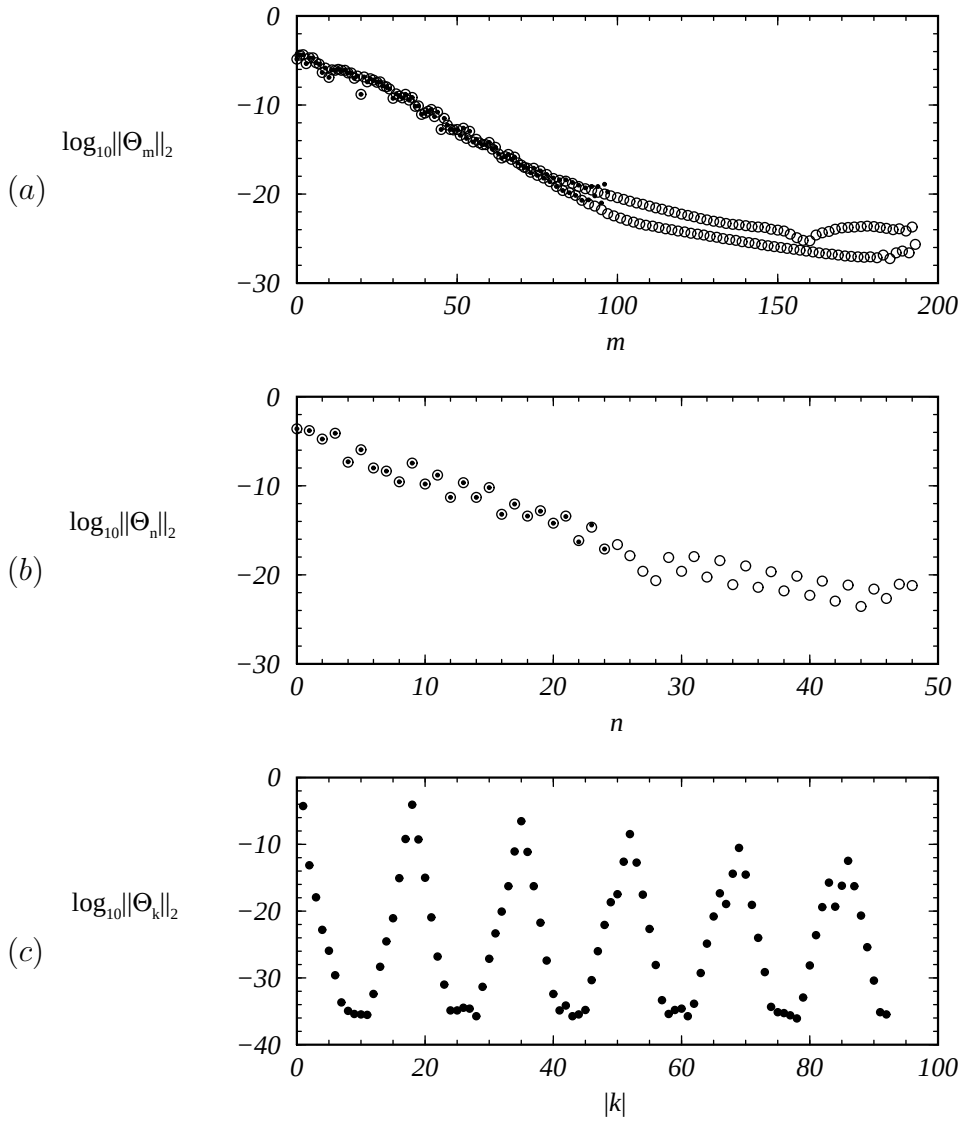

Figure 4.1: The L_2-norms of (a) Θ_m, (b) Θ_n, and (c) Θ_k for a modulated wall mode at $A = 0.0075$, $\Omega_m = 10^{1.5}$, with $Ra = 5 \times 10^4$ and $\Omega_0 = 625$. The open symbols correspond to solutions obtained using $(n_r, n_z, n_\theta) = (96, 48, 184)$, while the filled symbols correspond to solutions with $(n_r, n_z, n_\theta) = (48, 24, 184)$.

$n_\theta = 184$ Fourier modes in θ were used. The time discretization used $\delta t \leq 0.00015$ viscous time units, with no fewer than 300 δt per modulation period. Figure 4.1 shows the rate of spectral convergence of Θ for a typical modulated wall mode, with $A = 0.0075$, $\Omega_m = 10^{1.5}$ and $Ra = 5\times10^4$, computed with $(n_r, n_z, n_\theta) = (48, 24, 184)$ (filled symbols), and compared to a simulation with higher resolution using $(n_r, n_z, n_\theta) = (96, 48, 184)$ (open symbols). The temperature perturbation is expanded as

$$\Theta(r,\theta,z,t) = \sum_{m=0}^{2n_r+1}\sum_{n=0}^{n_z}\sum_{k=-n_\theta/2}^{n_\theta/2-1} \hat{v}_{mnk}(t)T_m(r/\gamma)T_n(2z)e^{ik\theta}. \tag{4.6}$$

Although the radial sum extends up to $2n_r + 1$, Fornberg's prescription guarantees that there are exactly n_r+1 degrees of freedom in the radial direction. To demonstrate the spectral convergence of the method, the temperature perturbation was separated into its radial, axial and azimuthal components:

$$\Theta_m(r,\theta,z,t) = \sum_{n=0}^{n_z}\sum_{k=-n_\theta/2}^{n_\theta/2-1} \hat{v}_{mnk}(t)T_m(r/\gamma)T_n(2z)e^{ik\theta}, \tag{4.7}$$

$$\Theta_n(r,\theta,z,t) = \sum_{m=0}^{2n_r+1}\sum_{k=-n_\theta/2}^{n_\theta/2-1} \hat{v}_{mnk}(t)T_m(r/\gamma)T_n(2z)e^{ik\theta}, \tag{4.8}$$

$$\Theta_k(r,\theta,z,t) = \sum_{m=0}^{2n_r+1}\sum_{n=0}^{n_z} \hat{v}_{mnk}(t)T_m(r/\gamma)T_n(2z)e^{ik\theta}. \tag{4.9}$$

The relative truncation error was estimated for the radial and axial Chebyshev expansions by dividing the largest L_2-norm component of the lower resolution solution by the smallest L_2-norm component of the same, where the L_2-norm is given by,

$$||\Theta||_2 = \left[\int_{-1/2}^{1/2}\int_0^{2\pi}\int_0^{\gamma} \Theta^2(r,\theta,z)r\,dr\,d\theta\,dz\right]^{1/2}. \tag{4.10}$$

In the azimuthal direction, the relative truncation error was estimated by considering the ratio of the peak of the first harmonic to that of the fifth harmonic. The relative truncation error for the solution shown in figure 4.1 is 10^{-15} in r, 10^{-13} in z, and 10^{-8} in θ.

In the present study, the aspect ratio $\gamma = 4$, Prandtl number $\sigma = 7$, and Coriolis number $\Omega_0 = 625$ are fixed to correspond to those in previous studies (Lopez, Rubio & Marques, 2006*b*; Lopez, Marques, Mercader & Batiste, 2007), and we consider variations in A and Ω_m for $Ra = 4 \times 10^4$ and 5×10^4.

4.3 Background on unmodulated wall modes

For the constant rotation problem in the limit of zero centrifugal force, the basic state consists of solid-body rotation with the conductive linear temperature profile,

$$(u, v, w, \Theta)(r, \theta, z, t) = (0, 0, 0, 0). \tag{4.11}$$

For small Ω_0 (between about 20 and 100, depending on the parameter regime), convection sets in as a bulk mode with Küppers–Lortz spatio-temporal chaos. For $\Omega_0 > 125$ and $\sigma = 6.4$, the onset of convection occurs as a wall mode, a convective mode local to the sidewall emerging as a result of the interplay between the Coriolis force and the sidewall (Zhong, Ecke & Steinberg, 1991; Goldstein, Knobloch, Mercader & Net, 1994). The onset of the wall mode breaks the continuous $SO(2)$ symmetry of the basic state; the wall modes are invariant to discrete rotations $R_{2\pi/m}$ where the azimuthal wavenumber m is the number of pairs of hot and cold plumes. Breaking the $SO(2)$ symmetry leads to a precession of the wall mode structure (Ecke *et al.*, 1992). The spatial structure does not vary in time, the solution is a rotating wave and hence a relative equilibrium in a frame of reference rotating at its precession frequency. The K_z reflection symmetry is also broken, but the wall modes are invariant under a half-wavelength rotation composed with a reflection, $R_{\pi/m}K_z$.

For $\Omega_0 = 625$, $\sigma = 7$ and $\gamma = 4$, the emergence of the wall mode has been studied in some detail (Lopez, Marques, Mercader & Batiste, 2007). Onset is via an Eckhaus–Benjamin–Feir instability in which the solution with $m = 18$ bifurcates first at $Ra = 42,286$, and a $m = 17$ mode bifurcates and becomes stable to long wave

Figure 4.2: Isosurfaces of Θ, at $\Theta = \pm 0.05$, for a $m = 17$ wall mode at $Ra = 5 \times 10^4$, $\Omega_0 = 625$ and $A = 0$. Movie 1, available in the online version, shows this solution over 7 viscous times at a rate of 0.84 viscous times per second.

perturbations at a slightly larger Ra. The onset of convection throughout the cell, i.e. the onset of bulk convection, occurs at about $Ra = 9.6 \times 10^4$, with some considerable influence from initial conditions (Marques & Lopez, 2008). For the majority of this study, a $m = 17$ wall mode at $Ra = 5 \times 10^4$ (shown in figure 4.2 and movie 1, available in the online version), was used as the initial condition since the dynamics of the modulated wall modes of various wave numbers were found to be qualitatively the same. The instantaneous precession rate of a rotating wave is given by

$$\Omega_p = \frac{d\phi}{dt} = \Omega_H / m, \tag{4.12}$$

where ϕ is the angular position of a point in the pattern and Ω_H is the Hopf frequency of the wall mode. For the case shown in figure 4.2, $\Omega_p = -0.2831$ (it is negative because the precession is retrograde).

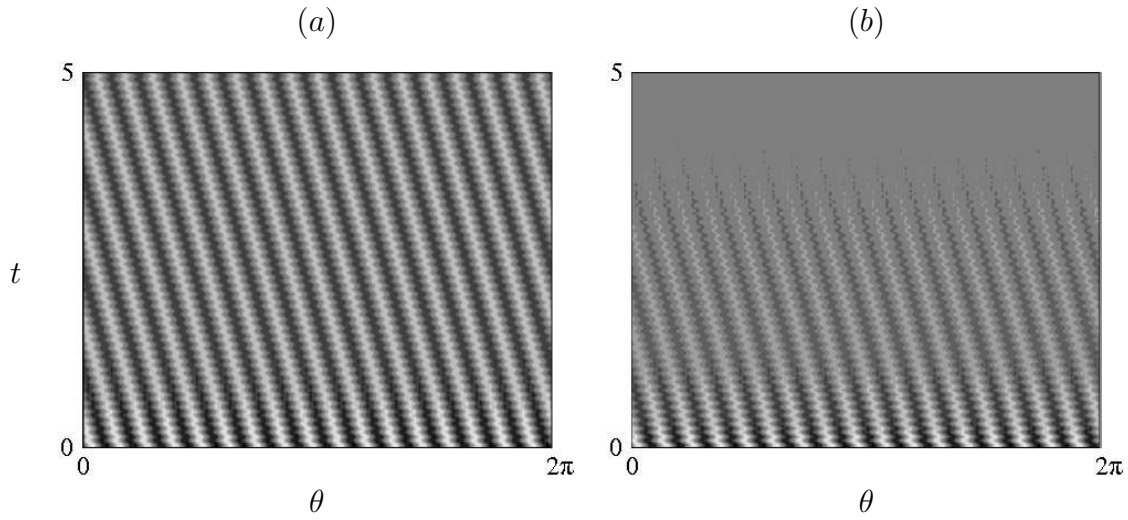

Figure 4.3: Space-time diagrams ($\theta \in [0, 2\pi)$ in the horizontal direction and 5 viscous times in the vertical direction) of $\Theta(r = \gamma, \theta, 0, t)$ for modulated wall modes at $Ra = 5 \times 10^4$, $\Omega_0 = 625$, $\Omega_m = 10^{1.75}$ with (a) $A = 0.0075$ and (b) $A = 0.01$. Movies 2 and 3, available in the online version show three-dimensional renderings of these two solutions over 5 viscous times at a rate of 0.112 viscous times per second, i.e. 1 modulation period per second.

4.4 Results

Wall mode quenching

When wall modes are subjected to modulated rotation, the convective plumes disappear for quite small amplitudes of modulation over a range of modulation frequencies. While at first glance one may expect resonances to be responsible, they are not. The quenching of the wall mode is not a result of resonance with the modulation-driven flow. The reason is that for there to be a resonance between the two flows, both the temporal frequencies and the spatial frequencies need to be in the same rational ratio (see the discussion in the appendix of Lopez & Marques, 2004). While the temporal frequencies could be tuned, the azimuthal wavenumbers are never resonant with them. The wall mode has $m \neq 0$ (here we focus on $m = 17$) and the modulation-driven flow

is axisymmetric with $m = 0$.

The space-time plots in figure 4.3 show the decay of transients for two small modulation amplitudes, $A = 0.0075$ and $A = 0.01$. Both evolutions were initiated with the wall mode shown in figure 4.2 at $Ra = 5 \times 10^4$, $\Omega_0 = 625$ and $\Omega_m = 10^{1.75}$. This value of Ω_m corresponds to a modulation period of $\tau = 2\pi/\Omega_m \approx 0.112$ viscous times, which is very small compared to the 22.19 viscous times for the unmodulated wall mode to precess 2π radians (the modulation can be seen as "wiggles" in the mean precession of the wall plumes in the figure). For a modulation amplitude of 0.75% of the background rotation rate ($A = 0.0075$), we see in figure 4.3(a) that the wall mode quickly adjusts to the modulated rotation rate and persists indefinitely, sloshing back and forth with the modulation period. The adjustment is seen as a reduction in contrast of the grey scales over the first viscous time in figure 4.3(a). Such states where the wall mode coexists with the secondary flow driven by the modulated rotation are referred to as modulated wall modes. These states have the same spatial symmetries as the unmodulated wall modes, however their spatial structure varies with time and they are no longer relative equilibria. For a slightly larger $A = 0.01$, we see from figure 4.3(b) that in about five viscous times, corresponding to about forty-five modulation periods, the wall mode has been quenched and thermal convection ceases. The final state is $\tau-$periodic (synchronous with the modulation) and invariant under both R_α and K_z; we refer to such states as the synchronous states. Movies 2 and 3 in the online version show three-dimensional renderings of the solutions in figures 4.3(a) and (b), respectively.

The quenching of a wall mode at some critical A and Ω_m is a $SO(2)\times Z_2$ symmetry-restoring Hopf bifurcation. A convenient measure to determine when this occurs is

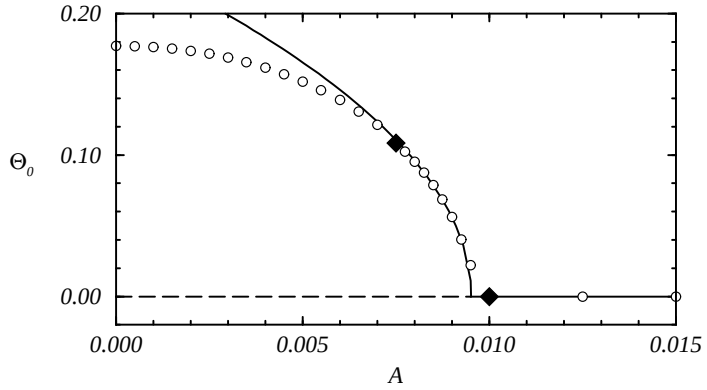

Figure 4.4: Variation of Θ_0 with A at $\Omega_m = 10^{1.75}$. Data points are shown as circles while the cases in figure 4.3(a) and (b) are shown as filled diamonds. A solid black curve shows a quadratic fit of the first five data points while horizontal dashed and solid lines show the values of A for which the synchronous state is unstable and stable, respectively.

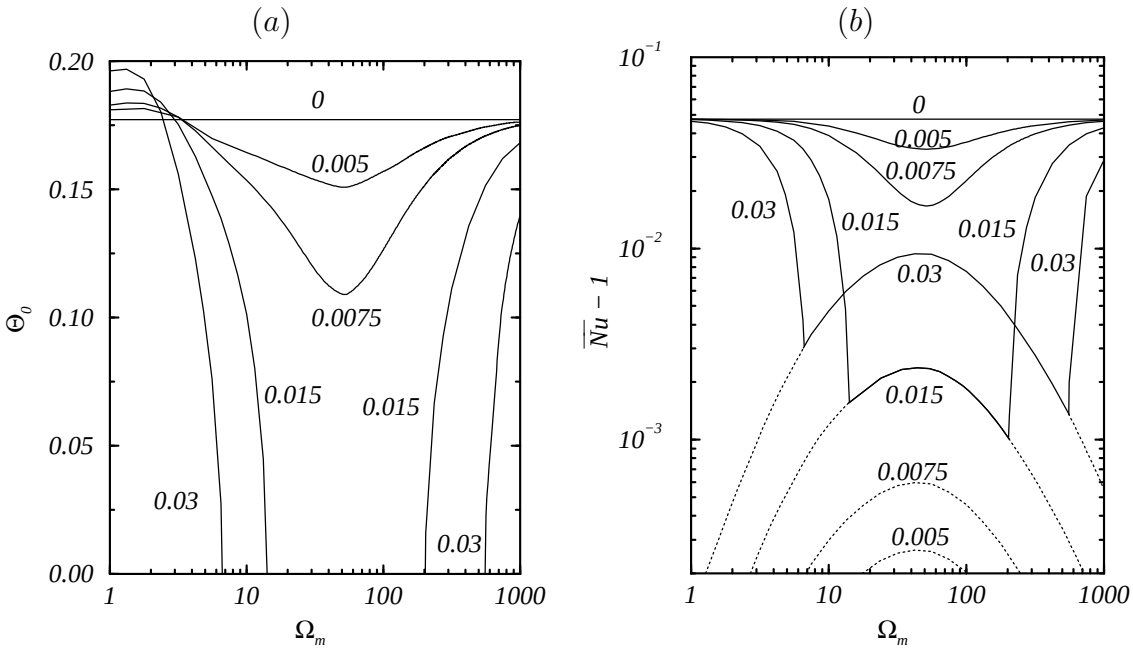

Figure 4.5: Variation with Ω_m of (a) Θ_0 and (b) $\overline{Nu} - 1$, at A as indicated, for modulated wall modes at $Ra = 5 \times 10^4$ and $\Omega_0 = 625$. The values of $\overline{Nu} - 1$ for the axisymmetric synchronous state are drawn as dotted lines in (b).

the maximum value of Θ at mid-height on the wall:

$$\Theta_{\max}(t) = \max_{\theta\in[0,2\pi)} |\Theta(r=\gamma,\theta,z=0,t)|. \tag{4.13}$$

Its value at the start of a modulation period, $\Theta_{\max}(n\tau)$, for n (number of modulation periods) large enough so that the transients have decayed, is constant and we shall denote it as Θ_0. For the synchronous states, when the wall modes have been quenched, $\Theta_{\max}(t) = 0$ and $\Theta_0 = 0$, while for modulated wall modes these quantities are not zero. Figure 4.4 shows the variation in Θ_0 for varying A at $\Omega_m = 10^{1.75}$. Clearly seen is the $\sqrt{A_c - A}$ scaling characteristic of a Hopf bifurcation while the measured Hopf frequencies, $\Omega_H(A)$, vary weakly between 4.7807 and 4.8447 for $\Theta_0 > 0$; $\Omega_H = 4.8127$ for the unmodulated case $A = 0$. Figure 4.5(a) shows how this local (in space and in time) measure of the temperature varies with Ω_m and A for $Ra = 5 \times 10^4$ and $\Omega_0 = 625$. There is a drop in Θ_0 for a range of frequencies centered about $\Omega_m = 10^{1.75}$ that expands with increasing A, and quenching ($\Theta_0 \to 0$) occurs for $A > 0.01$ in this range of frequencies. At low Ω_m, there is an enhancement in Θ_0 with increasing A, but this is an artifact of the phase of the modulation chosen to define Θ_0. While Θ_0 is definitive in characterizing quenching, a more global measure is also needed to assess the net effects of the modulations.

Such a global measure is the time-averaged heat flux across the layer. The heat flux vertically across the layer is characterized by the Nusselt number, the ratio between the heat transfer of the solution considered, and the heat transfer of the $A = 0$ conductive state, given by

$$Nu = -\langle \partial T/\partial z\rangle|_{z=0.5} = \langle 1 - \partial\Theta/\partial z\rangle|_{z=0.5}\,, \tag{4.14}$$

where $\langle\cdot\rangle = \int_0^\gamma \int_0^{2\pi} \cdot r\mathrm{d}r\mathrm{d}\theta$. Since the flow is time-dependent for $A > 0$, we consider

the Nusselt number averaged over the modulation period, τ:

$$\overline{Nu} = \frac{1}{\tau}\int_0^\tau Nu \; \mathrm{d}t. \tag{4.15}$$

Note that for $A = 0$, since the wall modes are rotating waves whose spatial structure simply precesses without change, their Nusselt number is constant.

Figure 4.5(b) shows that the mean heat flux associated with the modulated wall modes is diminished with increasing A. For the range of Ω_m for which the wall modes are quenched ($\Theta_0 \to 0$), the system is not convecting heat in the usual sense, however the synchronous state to which the modulated wall modes are quenched have $\overline{Nu} - 1 \neq 0$. This modulation-driven heat flux is considerably smaller than that in the absence of modulation with all other parameters being equal, as evidenced in figure 4.5(b). For values of Ω_m and A for which quenching does not occur, we have also computed the (unstable) synchronous state by restricting the simulations to the axisymmetric subspace, i.e. solving the axisymmetric governing equations. The corresponding $\overline{Nu} - 1$ values are drawn as dotted lines in figure 4.5(b). The points where the solid $\overline{Nu} - 1$ curves of the modulated wall modes meet these dotted curves (for the same value of A) correspond to symmetry-restoring Hopf bifurcations responsible for the quenching. For the range of Ω_m where quenching takes place, the heat flux $\overline{Nu} - 1$ peaks to non-trivial values. This enhanced heat flux is driven by the oscillatory boundary layers. This mechanism is explored in the following subsection.

Synchronous state

In order to better understand the interaction between the oscillating boundary layers and the wall-localized thermal plumes, it is useful to study the boundary layers in isolation from the wall modes in the synchronous state. Since the synchronous state is axisymmetric, it is convenient to describe it in terms of streamlines and vortex lines. In the laboratory frame, the velocity is $(u, v + r\Omega_0, w)$, and the meridional

components can be written in terms of the Stokes streamfunction, $u = -1/r\partial\psi/\partial z$ and $w = 1/r\partial\psi/\partial r$. The corresponding vorticity is

$$\Big(-\frac{1}{r}\frac{\partial(rv + r^2\Omega_0)}{\partial z}, -\frac{1}{r}\Big(\frac{\partial^2}{\partial r^2} - \frac{1}{r}\frac{\partial}{\partial r} + \frac{\partial^2}{\partial z^2}\Big)\psi, \frac{1}{r}\frac{\partial(rv + r^2\Omega_0)}{\partial r}\Big) \tag{4.16}$$

Contours of ψ in a meridional plane depict the streamlines, and likewise, contours of $rv + r^2\Omega_0$ depict the vortex lines. Note that since Ω_0 is a constant, the radial vorticity is simply $-\partial v/\partial z$. The only variables that change between the laboratory and the rotating reference frames are the azimuthal component of velocity (differs by $r\Omega_0$) and the vertical vorticity (differs by the constant term $2\Omega_0$).

In the unmodulated problem, for $Ra < Ra_c$ the fluid remains in solid-body rotation with vortex lines parallel to the rotation axis. For $A > 0$, the vortex lines are alternately displaced radially outward and inward in harmonic Ekman layers at the top and bottom of the cylinder as the cylinder accelerates and decelerates over the modulation period. Of course, the vortex lines are not bent purely in the radial direction, but also into the azimuthal direction (Davidson, 1989; Lopez, 1995), and this resultant azimuthal component of vorticity η drives a meridional circulation characterized by the streamfunction, $\eta = u_z - w_r = -\psi_{rr}/r + \psi_r/r^2 - \psi_{zz}/r$; see (4.16). Figure 4.6 shows the streamlines, vortex lines, azimuthal vorticity, and temperature perturbation of a periodic solution at $A = 0.05$, $\Omega_m = 10^{1.75}$, $Ra = 4 \times 10^4$ and $\Omega_0 = 625$ at two phases of the modulation period, corresponding to the maximum and minimum values of $\Omega(t)$. Movie 4 in the online version shows the solution in figure 4.6 over ten periods. In this case, Ra is well below critical for the onset of thermal convection, ensuring that the synchronous state, which lacks thermally driven convection, is stable. The $\tau/4$ phase of the modulation is the end of the acceleration phase, and the vortex line bending drives a secondary flow which centrifuges fluid in the harmonic Ekman layers radially outwards. This centrifuged fluid drives cold fluid

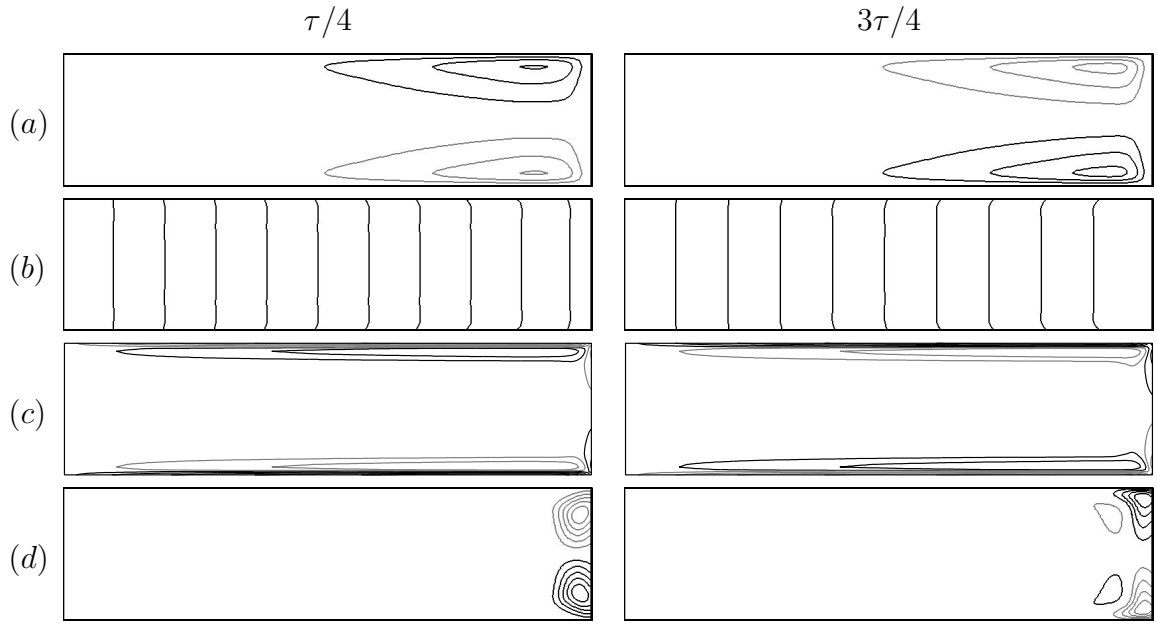

Figure 4.6: Contours in a meridional plane $r \in [0, \gamma]$, $z \in [-0.5, 0.5]$ of (a) ψ (streamlines), (b) $rv + r^2\Omega_0$ (vortex lines), (c) η (azimuthal vorticity), and (d) Θ (temperature perturbation), for the synchronous state at $A = 0.05$, $\Omega_m = 10^{1.75}$, $Ra = 4 \times 10^4$ and $\Omega_0 = 625$. Five positive (black) and five negative (grey) contours are linearly spaced for $\psi \in [-1.5, 1.5]$ and $\Theta \in [-0.1, 0.1]$, five positive and five negative contours are quadratically spaced for $\eta \in [-1000, 1000]$, while ten contours are quadratically spaced for $rv + r^2\Omega_0 \in [0, 1 \times 10^4]$. Movie 4, available in the online version, shows this solution over 1.12 viscous times (10 modulation periods) at a rate of 0.0186 viscous times per second (6 seconds per modulation period).

from the top layer and warm fluid from the bottom layer into the sidewall layer. The harmonic Ekman layers are seen as thin sheets of azimuthal vorticity at the top and bottom lids with weaker layers of oppositely signed vorticity just below and above, respectively. The $3\tau/4$ phase is the end of the deceleration phase; now the vortex lines bend in the reversed direction driving a secondary flow which draws fluid from near the sidewall radially inward in thin harmonic Ekman layers in which the sign of the azimuthal vorticity has changed since the acceleration phase. Fluid from the core moves towards the corners where the lids meet the sidewall to replace the fluid

drawn into the harmonic Ekman layers, making the top (bottom) corner relatively warmer (cooler).

Figure 4.7(a) shows vertical profiles of the azimuthal vorticity at $r = \gamma/2$. For $\Omega_m < 10^{2.5}$ the azimuthal vorticity profiles behave as a standing wave with no noticeable penetration of the azimuthal vorticity beyond $0.15d$ from the lid. The standing waves are predicted by the analysis of simple-harmonic Ekman flow (chapter 7, §3.5 of Yih, 1977), which considers the harmonic modulation of a rotating infinite disk, at vertical location $z^* = 0$ with length scale $\sqrt{\nu/\Omega_0}$, where Ω_0 is the mean rotation equal to the background rotation. Such a flow has an azimuthal velocity

$$v(z^*, t) = 0.5A\Omega_0 \Re\left[e^{-\beta_1 z^* + i\Omega_m t} + e^{-\beta_2 z^* + i\Omega_m t}\right], \tag{4.17}$$

where $\Re$ denotes the real part and β_1 and β_2 are the roots with positive real part of the characteristic polynomial that arises after the radial velocity is eliminated

$$y^4 - i2\Omega_m y^2 - (\Omega_m^2 - 4\Omega_0^2) = 0. \tag{4.18}$$

The arrows shown with the azimuthal vorticity in figure 4.7(a) show the characteristic scaling lengths, $\delta_{\beta_1} = \Re(\beta_1)^{-1}$ and $\delta_{\beta_2} = \Re(\beta_2)^{-1}$ for each Ω_m. When $\Omega_m < 2\Omega_0$, the solution is a pair of counter-propagating waves that are nearly balanced for small modulation frequencies. When $\Omega_m/\Omega_0 << 1$, Yih's solution can be approximated by

$$v(z^*, t) \approx A\Omega_0 e^{-\Omega_0^{-0.5} z^*} \cos(\Omega_m t) \cos(2\Omega_0^{0.5} z^*), \tag{4.19}$$

which is a standing wave. For $\Omega_m \geq 10^{2.5}$, the two theoretically predicted counter-propagating waves are no longer nearly balanced and the azimuthal vorticity near the top and bottom lids act as traveling waves. Figure 4.7(b) shows radial profiles of the relative axial vorticity, $v/r + v_r$, at the mid-height $z = 0$. For the range of modulation frequencies explored, the sidewall boundary layer behaves as a traveling

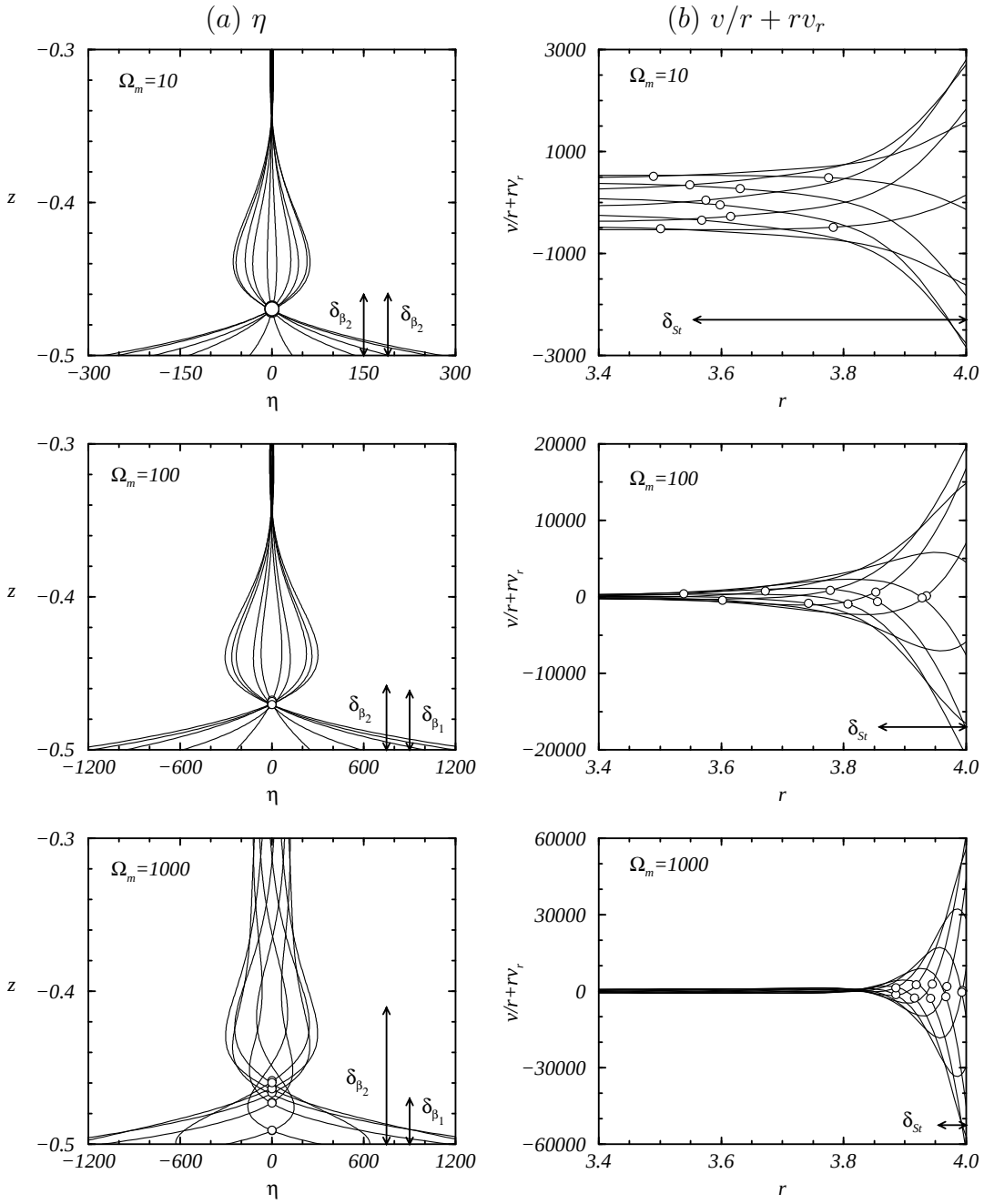

Figure 4.7: Profiles of η (azimuthal vorticity) and $v/r + rv_r$ (relative axial vorticity) for the synchronous states at $A = 0.05$, $Ra = 4\times10^4$, $\Omega_0 = 625$ and various Ω_m. Data is shown at $r = \gamma/2$ for $z \in [-.5, -.25]$ and $r \in [3.4, 4]$, respectively, over ten equally spaced phases of a modulation period. The circles show the boundary layer depth estimate for each time that is used in the calculation in figure 4.8. The arrows labeled δ_{β_1} and δ_{β_2} give the boundary layer depth estimates for Yih's harmonic Ekman layer analysis in the vertical azimuthal vorticity figures and the arrows labeled δ_{St} give the Stokes boundary layer depth estimate in the radial relative axial vorticity figures.

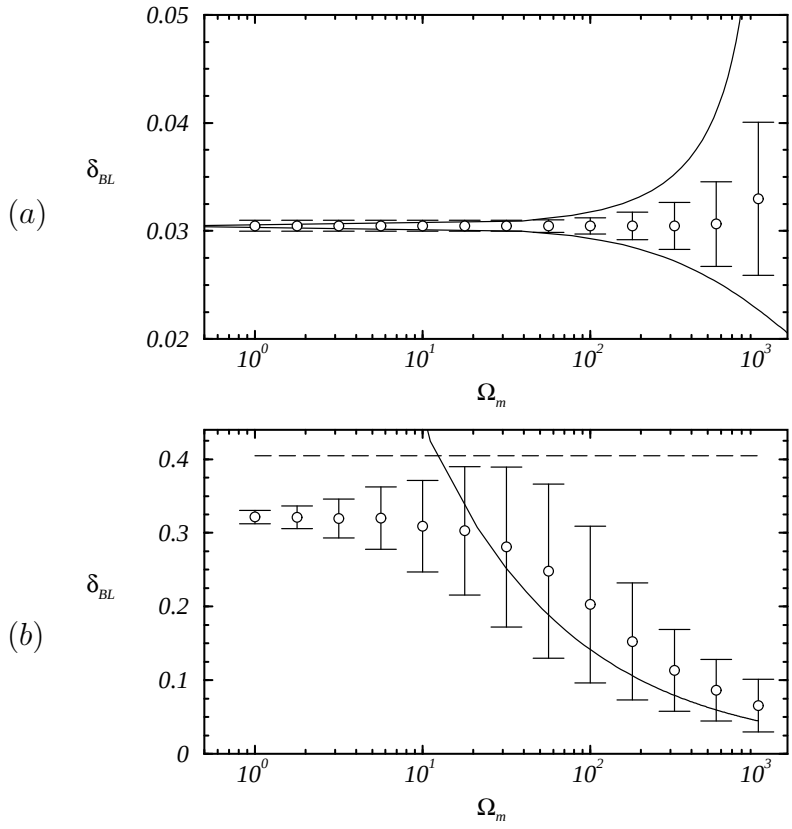

Figure 4.8: (a) Estimated top and bottom lids boundary layer depth, δ_{BL}, for synchronous states at $A = 0.05$, $Ra = 4 \times 10^4$, $\Omega_0 = 625$ and various Ω_m at $r = \gamma/2$ over a modulation period. δ_{β_1} and δ_{β_2}, the theoretical harmonic Ekman layer depth estimate given by Yih and scaled to the measurement at $\Omega_m = 1$ are shown as solid lines, forming a horn-shaped region. (b) Estimated sidewall boundary layer width measured at $z = 0$ for the same cases shown in (a). A solid line indicates the theoretical Stokes layer depth estimate and a dashed line indicates the width of a thermal plume in the unmodulated case. In both plots mean values are shown as empty circles with the standard deviation denoted by error bars.

wave similar to a Stokes layer, whose $\delta_{St} = \Omega_m^{-0.5}$ scaling depth is shown in the figure for each sidewall relative axial vorticity profile.

The depth of the boundary layer at the top and bottom lids was estimated by finding the first zero of the azimuthal vorticity (circles in figure 4.7a). The results are shown in figure 4.8(a) and are compared with the harmonic Ekman layer depths,

δ_{β_1} and δ_{β_2}, given by Yih (1977), which we have scaled to the mean boundary layer depth in our problem at $\Omega_m = 1$. The theoretical estimates of Yih capture the Ω_m dependence of our boundary layers on the top and bottom lids, including the onset and approximate magnitude of the traveling waves found at higher Ω_m. Measurements of the boundary layer thickness at the sidewall are more difficult as the far-field ($r = 0$) axial vorticity adjusts with the modulation. The sidewall boundary layer depth was estimated as the distance where the relative axial vorticity near the sidewall is 90% of its free stream value. For $\Omega_m < 10$ the mean boundary layer depth is approximately independent of Ω_m, whereas for larger Ω_m, it has the classical Stokes layer scaling of $\Omega_m^{-0.5}$. At frequencies near optimal for quenching wall modes, the variation of its depth over a period (characterized by the standard deviation, as indicated by the error bars in the figure) is largest, tapering off for larger and smaller Ω_m.

For the synchronous state, the instantaneous (u, v, w, Θ) scale linearly with A. Figure 4.9(a) illustrates this linear scaling by plotting the L_2-norms of $(u, v, w, \Theta)/A$ at a particular phase of the modulation period ($t_0 = \tau/2$), for $Ra = 4 \times 10^4$ and $\Omega_0 = 625$ over a range of Ω_m and several values of A. Similar linear scalings with A occur at other phases. For larger A the linear scaling deteriorates slightly; this is manifested as a phase shift in the instantaneous azimuthal velocity, v.

The time averages over a modulation period of (u, v, w, Θ) scale with A^2. Figure 4.9(b) illustrates this by plotting the L_2-norms of $(\overline{u}, \overline{v}, \overline{w}, \overline{\Theta})/A^2$, where

$$(\overline{u}, \overline{v}, \overline{w}, \overline{\Theta}) = \frac{1}{\tau} \int_0^\tau (u, v, w, \Theta)(r, \theta, z, t)\ \mathrm{d}t. \tag{4.20}$$

The difference between the linear scaling for the instantaneous fields and the quadratic scaling for the time-averages can be accounted for by considering the Fourier expansions of the variables in time. Since the synchronous axisymmetric state is time periodic with the same period as the forcing, $\tau = 2\pi/\Omega_m$, it can be Fourier expanded

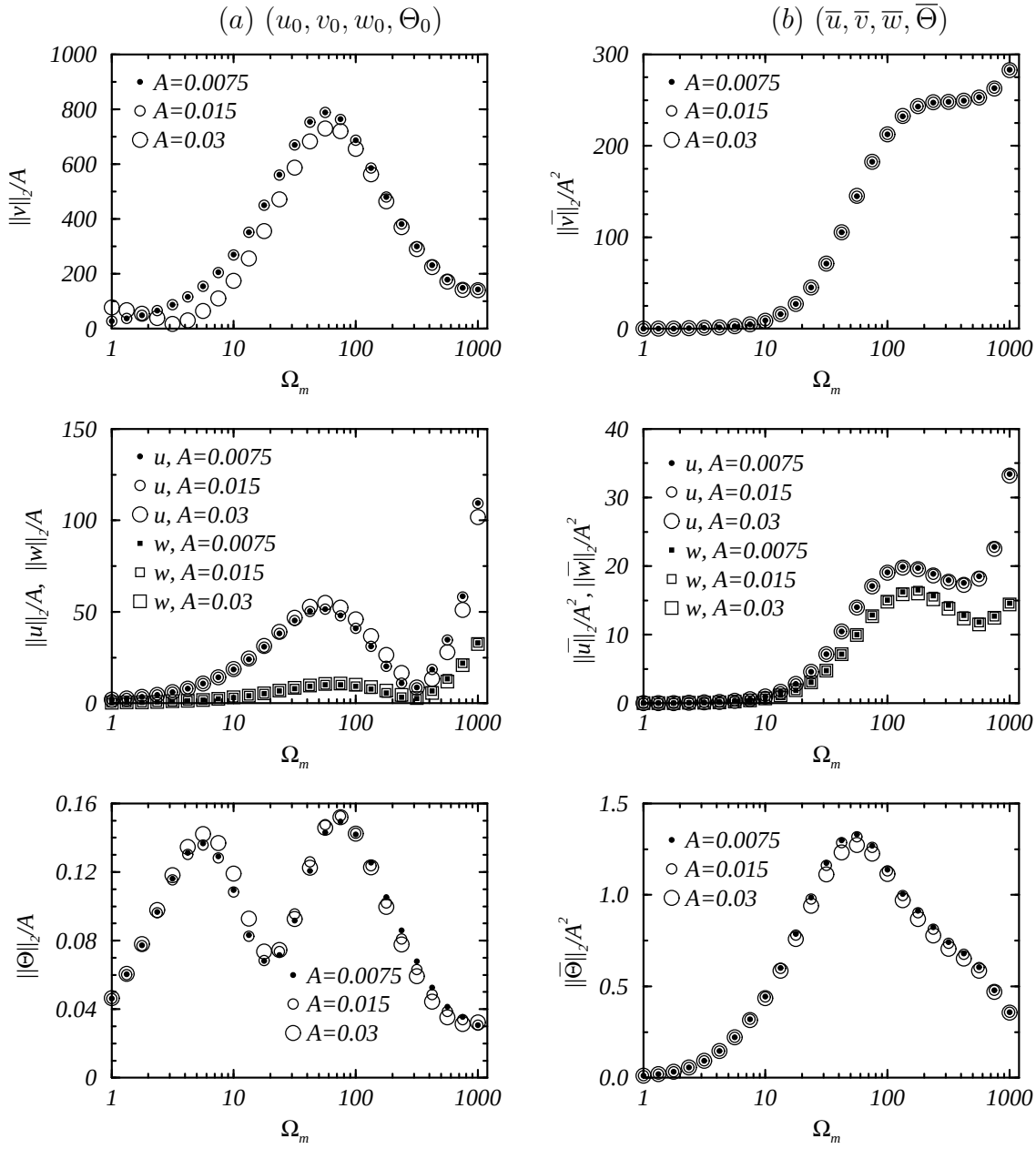

Figure 4.9: Variations with A and Ω_m of (a) the L_2-norms of $(u_0, v_0, w_0, \Theta_0)$ divided by A for $A = 0.0075, 0.015, 0.03$ and (b) the L_2-norms of the $(\overline{u}, \overline{v}, \overline{w}, \overline{\Theta})$ divided by A^2 for $A = 0.0075, 0.015, 0.03$, both taken for synchronous states with $Ra = 4 \times 10^4$, $\Omega_0 = 625$.

in time as (using v as an example)

$$v(r,z,t) = \sum_{n=-\infty}^{\infty} C_n(r,z)e^{in\Omega_m t}\,. \tag{4.21}$$

Substitution into the Navier–Stokes equations results in a coupled system of PDEs for the coefficients $C_n(r,z)$. The equation for C_n is linear, except for the advection terms which are quadratic and couple Fourier modes with different n. The external forcing appears only in the boundary conditions for the $n = 1$ mode. As a result, for small forcing amplitude A (so that higher order terms coming from the nonlinearities are smaller than the boundary forcing, which is linear in A), $C_1 \propto A$. This is the origin of the linear scaling of the instantaneous velocity with A. The source terms for the $n \neq 1$ temporal Fourier modes come exclusively from the quadratic advection terms, resulting in $C_0, C_2 \propto A^2$, $C_3 \propto A^3$ and so on (in fact, $C_n \propto A^n$ for $n \geq 1$, where A^n is the lowest order of A appearing in C_n). Upon taking time averages of a periodic quantity, such as v, only the zero Fourier mode survives, because

$$\int_0^\tau e^{in\Omega_m t}dt = 0, \quad \forall n \neq 0. \tag{4.22}$$

Therefore $\overline{v} \propto C_0 \propto A^2$, giving the observed quadratic scaling with A. In summary, instantaneous values are dominated by the $n = 1$ temporal Fourier mode, driven by the forcing, with amplitude proportional to A, while the time-averaged values contain only the $n = 0$ Fourier mode, driven by the quadratic advection terms, with amplitudes proportional to A^2.

The mean streaming flow characterized in figure 4.9(b) is driven by the modulations. It is negligible for $\Omega_m < 10$, and the mean meridional flow has a relative maximum near $\Omega_m = 100$. The L_2-norm of the mean azimuthal flow is an order of magnitude larger than that of the mean meridional flow, and all the mean velocity components are largest at the highest frequencies considered. The mean thermal

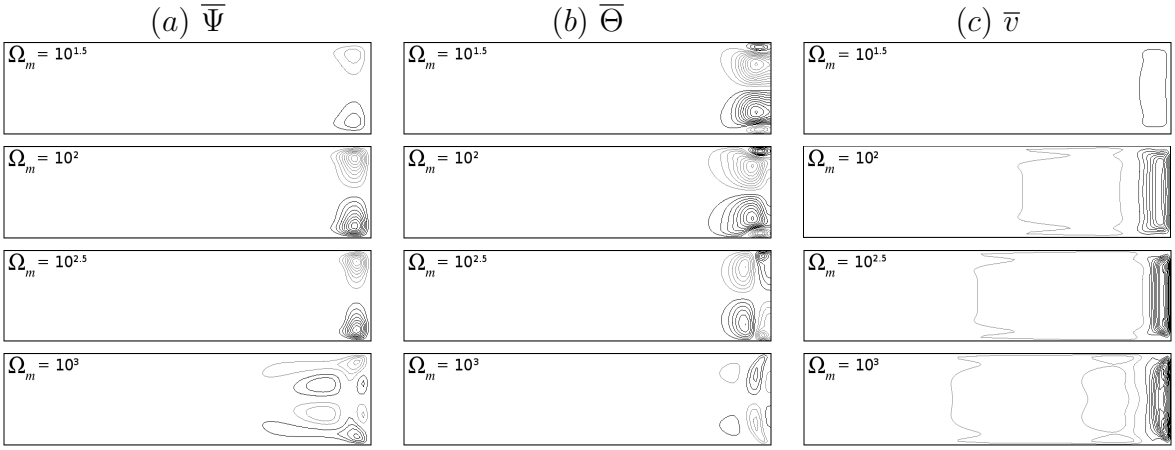

Figure 4.10: Contours of the meridional streaming flow, $\overline{\Psi}$, mean temperature perturbation, $\overline{\Theta}$, and azimuthal streaming flow, $\overline{v}$, for synchronous states at $A = 0.03$, $Ra = 4 \times 10^4$, $\Omega_0 = 625$ and various Ω_m. Ten positive (black) and ten negative (grey) contours are linearly spaced for $\overline{\Psi} \in [-0.03, 0.03]$, $\overline{\Theta} \in [-0.01, 0.01]$ and $\overline{v} \in [-1.5, 1.5]$, in a meridional plane $r \in [0, \gamma]$, $z \in [-0.5, 0.5]$.

perturbation is largest near the optimal quenching frequency of $\Omega_m = 10^{1.75}$ and gradually declines with increasing Ω_m. This is consistent with the behavior of $\overline{Nu} - 1$, the time-averaged Nusselt number, discussed in § 4.4, since

$$\overline{Nu} \; = < 1 - \partial\overline{\Theta}/\partial z >_{z=0.5} . \tag{4.23}$$

The structure of the mean streaming flow, which is axisymmetric, in a meridional plane at $A = 0.05$, $Ra = 4\times10^4$ and $\Omega_0 = 625$, for various Ω_m, is shown in figure 4.10. The streaming flow is strongest near the sidewall, occupying about the same volume as the thermal plumes of the wall mode at the higher $Ra = 5\times10^4$. The mean meridional flow, characterized by the mean streamfunction, is shown in figure 4.10(a). At the highest frequencies, the mean meridional flow penetrates into the interior. The structure of the mean thermal perturbation, $\overline{\Theta}$, is shown in figure 4.10(b). Figure 4.10(c) shows the mean azimuthal flow, $\overline{v}$, which is in the prograde direction, whereas the unmodulated wall mode precesses in the retrograde direction.

From the parametric studies of the wall mode quenching and of the structures of the boundary layers and the mean flow, three different frequency regimes clearly emerge. The *low frequency regime* corresponds to frequencies $\Omega_m \lessapprox 10^{0.5}$ for the $Ra = 4 \times 10^4$ and $\Omega_0 = 625$ case shown in detail in this section. In this regime, the harmonic Ekman layers at the top and bottom endwalls behave as standing waves. The sidewall boundary layer is thick, its depth varies little in time, and the mean streaming flow $(\overline{u}, \overline{v}, \overline{w}, \overline{\Theta})$ is very weak.

The *intermediate frequency regime*, where the quenching acts efficiently, corresponds to frequencies $10^{0.5} \lessapprox \Omega_m \lessapprox 10^{2.5}$ for the $Ra = 4 \times 10^4$ and $\Omega_0 = 625$ case. Here, the harmonic Ekman layers at the top and bottom endwalls continue to behave as standing waves, the sidewall boundary layer is also thick, but its depth varies considerably with time. The magnitude of the azimuthal mean velocity increases with frequency in this regime. The magnitudes of the mean meridional velocities have local maxima for Ω_m very close to the most efficient quenching frequency, and the magnitude of $\overline{\Theta}$ is also largest in this frequency range. This strongly suggests that the physical mechanism responsible for the quenching is associated with the strong meridional mean flow and the corresponding enhanced heat transport. This meridional mean flow is localized near the sidewall, where the thermal plumes of the wall modes also appear. The spatial structure of this mean flow is in sharp contrast to the structure of the thermal plumes of the wall modes. The mean flow is axisymmetric and reflection symmetric with respect to the horizontal mid-plane, and its vertical velocity and temperature perturbation change sign in the top and bottom halves of the cylinder, vanishing at mid-height. The wall mode thermal plumes are far from axisymmetric and have maximum vertical velocity at mid-height, and this changes sign from plume to plume in the azimuthal direction, with the cold plumes comprised of descending fluid and the hot plumes with rising fluid.

The *high frequency regime* corresponds to frequencies larger than about $\Omega_m \approx 10^{2.5}$ (for the $Ra = 4 \times 10^4$ and $\Omega_0 = 625$). In this regime, the harmonic Ekman layers behave as traveling waves and the sidewall boundary layer is thin and its depth varies little with time. The magnitudes of mean velocities are larger than in the intermediate frequency regime, while the mean temperature $\overline{\Theta}$ is smaller. The quenching mechanism ceases to work, very likely because the meridional mean flow is no longer concentrated at the sidewall boundary layer but penetrates into the bulk, and the induced heat transport decreases. The salient feature in this regime is the presence of a very strong azimuthal steady streaming, that drags the thermal plumes reducing their precession frequency.

We have defined the frequency ranges in the particular case $Ra = 4 \times 10^4$ and $\Omega_0 = 625$ discussed in detail in the paper. They can be defined in other parameter regimes in terms of the frequency at which the mean temperature $\overline{\Theta}$ reaches its maximum value, $\Omega_m^{\max}$ (see figure 4.10*b*). The intermediate frequency regime is centered around this $\Omega_m^{\max}$ frequency, and it extends approximately one order of magnitude below and above this value.

Modulated wall modes

For modulation frequencies and amplitudes where the wall modes are not quenched, the behavior of the resultant modulated wall modes are characterized by two regimes, the low and the high Ω_m regimes described above. For amplitudes A where there is no quenching for any Ω_m, there is a smooth transition between these two regimes. However, for large enough A (greater than about 1%), the two regimes are well separated by a spectral gap in Ω_m which grows with A (see figure 4.5).

Figures 4.11(a) and (b) show an overhead and perspective view of a modulated wall mode with $A = 0.0075$, $\Omega_m = 10^{1.75}$, $Ra = 5 \times 10^4$ and $\Omega_0 = 625$ at the

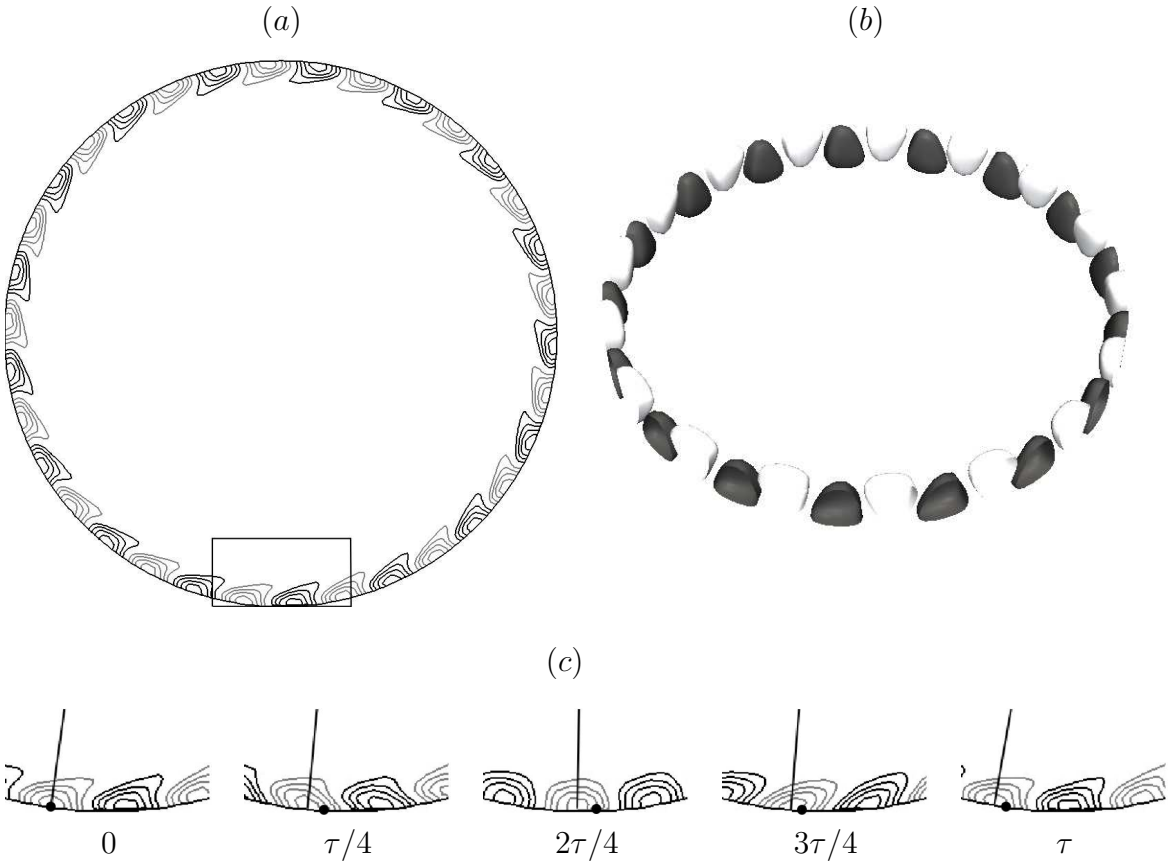

Figure 4.11: (a) Temperature perturbation Θ at the start of a modulation period for $A = 0.0075$, $\Omega_m = 10^{1.75}$, $Ra = 5 \times 10^4$ and $\Omega_0 = 625$; (a) shows contours at $z = 0$, five positive (black) and five negative (grey) in the range $\Theta \in [-0.125, 0.125]$, (b) shows a perspective view of isosurfaces at $\Theta = \pm 0.05$. (c) Close ups of the horizontal section delineated by the box in (a) over a modulation period τ; the black radial line in each frame indicates the center of a single cold plume over time and a black dot on the cylinder wall shows the position of a fixed point on the boundary.

beginning of a modulation period. While the wave number and overall shape of the plumes remains intact, Θ_0 is about half that of the unmodulated wall mode shown in figure 4.2(a). At this low modulation amplitude ($A = 0.0075$), the secondary flow driven by the oscillatory boundary layers co-exists with the wall-localized plumes. At $\Omega_m = 10^{1.75}$, the plumes do not precess significantly over the course of a modulation period. Figure 4.11(c) shows the temperature perturbation at mid-height $z = 0$ in a horizontal section near the sidewall (indicated by the box in figure 4.11a). The radial line in each panel of figure 4.11(c) indicates the angular location of an individual cold plume and the black dot on the cylinder wall indicates the modulated rotation of the cylinder.

In the low Ω_m regime (with periods much larger than the thermal adjustment time, d^2/κ) and low modulation amplitudes ($A < 0.01$), the wall mode adjusts quasi-statically between states with Coriolis numbers $\Omega_0(1 \pm A)$. The adjustment in the precession rate lags the change in the cylinder rotation by a small percentage of the modulation period. Figures 4.12(a–c) shows space-time diagrams of $\Theta(r = \gamma, \theta, z = 0, t)$ over 10 viscous times for low $\Omega_m = 10^{0.5}$ at various A. The plots are presented in the reference frame of the modulated cylinder, as the convective plumes are advected by the velocity fields in the sidewall boundary layer, complicating the use of the constant rotation frame for low modulation frequencies as the position of the cylinder can deviate by as much as $2A\Omega_0/\Omega_m$ radians from its original position in the reference frame rotating at the mean rotation rate. For low Ω_m, solutions with increasing A have significantly larger angular displacements, indicating that the azimuthal velocity near the sidewall is out of phase with the modulation. The convection is periodically enhanced during the acceleration phase and impeded during the deceleration phase of the modulation (seen as higher and lower contrasts in grey scale of the diagrams).

The high $\Omega_m = 10^3$ space-time diagrams are shown in figures 4.12(d–f). On the

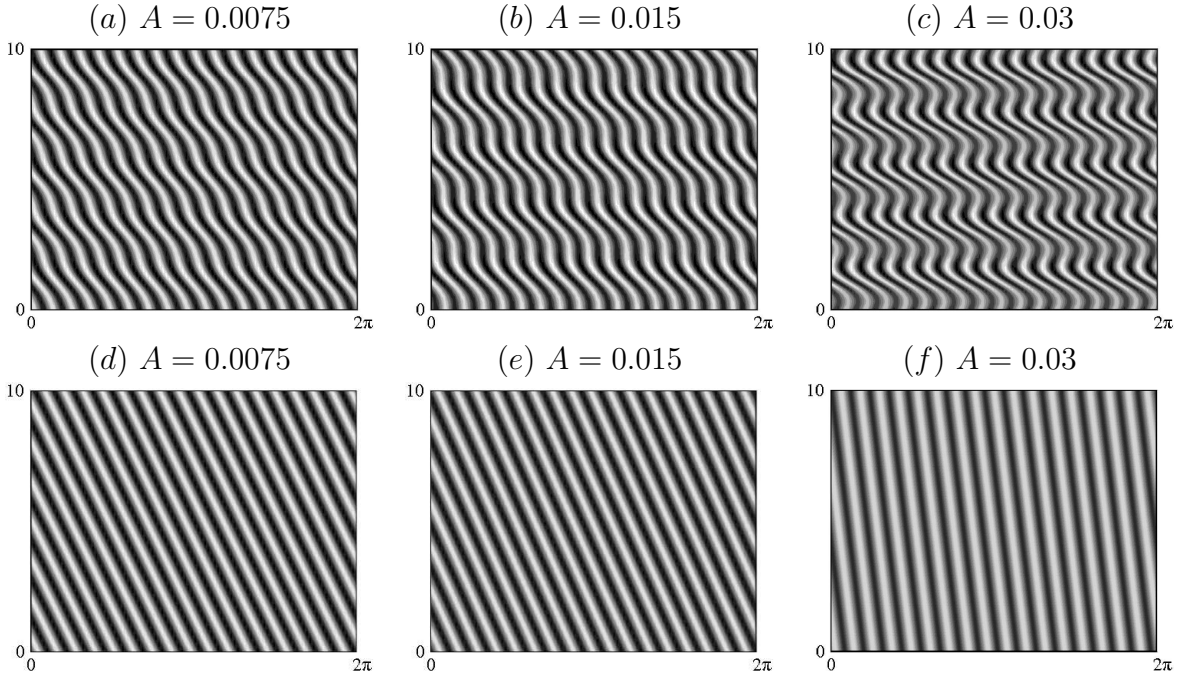

Figure 4.12: Space-time diagrams of modulated wall modes at $Ra = 5 \times 10^4$ and $\Omega_0 = 625$, showing $\Theta(r = \gamma, \theta, 0, t)$ with $\theta \in [0, 2\pi)$ (horizontal) in the reference frame of the modulated cylinder over ten viscous times (vertical), for various A in (a–c) the low frequency regime with $\Omega_m = 10^{0.5}$ and in (d–f) the high frequency regime with $\Omega_m = 10^3$. A little over five modulations periods are shown for $\Omega_m = 10^{0.5}$ and almost 1600 modulation periods are shown for $\Omega_m = 10^3$.

scale of the figures, the high frequency modulation is not visible; in the time shown (10 viscous times) there are about 1600 modulation periods. For $A = 0.0075$, the space-time diagram is virtually indistinguishable from that of the unmodulated wall mode; the mean precession is virtually the same as Ω_p. For large Ω_m, increasing A has the effect of slightly weakening the convection while substantially changing the pattern precession rate; the net precession at $A = 0.03$ has been slowed down considerably.

Figure 4.13 shows the angular position of the center of a plume over ten modulation periods for $A = 0.0075$, $A = 0.015$ and $A = 0.03$ with $\Omega_m = 10^3$, $Ra = 5 \times 10^4$

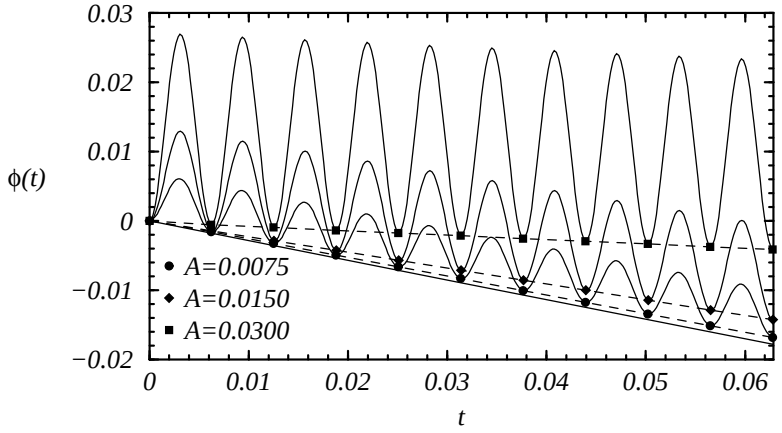

Figure 4.13: Angular position of the center of a plume over ten periods for A as indicated; the symbols correspond to the angular position of the plume at the end of each period. $\Omega_m = 10^3$, $Ra = 5 \times 10^4$ and $\Omega_0 = 625$. A black line indicates the angular position of the center of a plume for the unmodulated case at the same Ra and Ω. Dashed lines show $\overline{\Omega_p} t$ for each solution.

and $\Omega_0 = 625$. The plumes are sloshed back and forth by the modulation, and the amplitude of this sloshing motion increases linearly with A, as with the instantaneous velocity fields of the synchronous state. A solid black line gives the angular position of the center of a plume for the unmodulated case at the same Ra and Ω_0. The net precession of an individual plume over a modulation period can be quantified by $\overline{\Omega_p} = (\phi_f - \phi_i)/\tau$, where ϕ_i and ϕ_f are the initial and final angular positions of a plume over a modulation period τ; at $A = 0$, $\overline{\Omega_p} = \Omega_p$. The symbols in figure 4.13 correspond to the angular position of the plume at the end of each period. These symbols are on straight, dashed lines of slope $\overline{\Omega_p}$. The change in the net precession with increasing modulation amplitude A is quadratic, as is the mean velocity field of the synchronous state.

For $\Omega_m < 10^{1.75}$, $\overline{\Omega_p}$ is approximately equal to the precession rate of the unmodulated wall mode. However, for larger Ω_m, the mean precession rate slows, stops

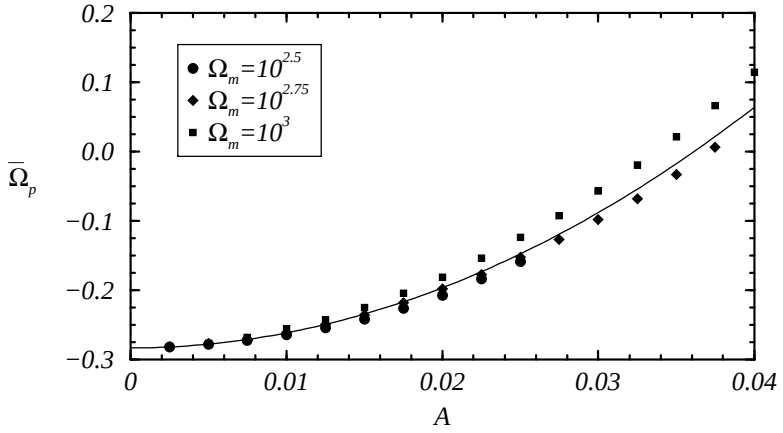

Figure 4.14: Variation of $\overline{\Omega_p}$ with A for Ω_m as indicated. The solid line shows the maximum mean angular velocity for synchronous states at $\Omega_m = 10^3$, $Ra = 4 \times 10^4$, $\Omega_m = 625$, translated by the precession frequency of the unmodulated wall mode Ω_p.

and reverses with increasing A; figure 4.14 gives the variation of $\overline{\Omega_p}$ with A for three different values of Ω_m. The contribution of the mean azimuthal streaming flow (figure 4.10) in advecting the thermal plumes at high Ω_m is quantified by the solid line in figure 4.14. This line corresponds to the maximum mean angular velocity, $||\overline{v}/r||_\infty$, of the synchronous state at $\Omega_m = 10^3$, $Ra = 4 \times 10^4$, $\Omega_0 = 625$ plus the retrograde (negative) precession frequency of the unmodulated wall mode Ω_p. The variation in $\overline{\Omega_p}$ with A is mostly accounted for by the angular velocity associated with the azimuthal streaming flow induced by the high frequency modulations.

4.5 Conclusions

We have considered rotating Rayleigh-Bénard convection in a regime where the rotation (characterized by the Coriolis number Ω_0) is sufficiently large that the onset of thermal convection, as the Raleigh number Ra is increased, is to a wall mode consisting of a pattern of hot and cold plumes, localized in the cylinder sidewall boundary layer, that precesses retrograde to the background rotation. These wall modes have

been subjected to harmonic modulations of the rotation rate of very small amplitude A and over a wide range of modulation frequencies Ω_m. The modulation gives rise to oscillatory boundary layers on the top, bottom and side endwalls of the cylinder which drive a large scale axisymmetric oscillatory flow, and for medium and high frequencies they also drive a mean streaming flow, both of which are strongest at the cylinder sidewall, precisely where the wall mode plumes are manifest. The nonlinear interactions between the modulation driven axisymmetric flows and the wall modes have been explored in detail.

The dynamics of the onset of thermal convection in the modulated problem as Ra is increased are qualitatively the same as in the unmodulated case, however the basic state is now a limit cycle synchronous with the modulation instead of the trivial state of solid-body rotation with a linear temperature profile in z, and the onset of thermal convection is to modulated wall modes at a Hopf bifurcation from the non-trivial basic state. A striking result of the imposed modulations over a wide range of frequencies, even for very small amplitudes, is the delay in the onset of the wall modes to much higher Ra, or for a given Ra, the complete quenching of the wall modes as the modulation amplitude A is increased. This delay of the onset of the wall modes is not a resonance effect, but rather a nonlinear interaction between the oscillatory boundary layers, which are inherently very stable against three-dimensional disturbances, and the wall modes, which are inherently three-dimensional. The lack of resonances when modulating rotating waves follows from the general theory that Hopf bifurcations from rotating waves do not manifest frequency-locking due to the rotational symmetry in the problem (Rand, 1982; Krupa, 1990). We have observed and analyzed the same absence of resonances in harmonically modulated Taylor–Couette flow (Avila, Marques, Lopez & Meseguer, 2007*a*).

The use of oscillatory Stokes boundary layers in the control of hydrodynamic insta-

bilities has a long history (Davis, 1976). They are particularly efficient in inhibiting and quenching three-dimensional instabilities, even when the applied amplitude is very small. We have observed this in diverse flows, including Taylor–Couette (Marques & Lopez, 1997, 2000; Avila *et al.*, 2007*a*), vortex breakdown (Lopez *et al.*, 2008), rotating convection (Rubio *et al.*, 2008), and the present flow provides yet another example. The well-defined structure of the wall modes has allowed us in this problem to explore in detail the interactions between the three-dimensional rotating thermal convection flow and the axisymmetric modulation-driven flow.

The nonlinear interaction between the oscillatory boundary layers and the wall modes is characterized by three different frequency regimes. The low Ω_m regime consists of a quasi-static adjustment to wall modes corresponding to the instantaneous value of the background rotation $\Omega(t) = \Omega_0[1 + A\sin(\Omega_m t)]$. In the high Ω_m regime, the thermal plumes associated with the wall mode remain intact despite the much stronger oscillatory and mean flows. However, the strong azimuthal streaming flow, whose strength increases with A and Ω_m, greatly affects the motion of the wall modes, resulting in the thermal plumes processing in the prograde direction at the largest values of A and Ω_m explored, as shown in figure 4.14.

For intermediate Ω_m, the action of the oscillatory boundary layers optimally quench the three-dimensional aspects of the flow. This quenching occurs as a symmetry-restoring Hopf bifurcation in which the non-axisymmetric component of the solution associated with thermal convection disappears. There is a large band of modulation frequencies for which the onset of wall-localized thermal convection is delayed by at least 18% for modulation amplitudes as small as 1% of the background rotation rate. The physical mechanism by which this delay occurs is characterized by the time-averaged Nusselt number of the synchronous state, and by extension the strength of the mean thermal perturbation. The effect of the secondary modulation-driven flow

on the thermal field is most pronounced for frequencies near $\Omega_m = 10^{1.75}$, even though the oscillatory and mean velocity are considerably stronger at larger Ω_m for a fixed A. However, the meridional component of the mean streaming flow peaks in strength in the intermediate Ω_m regime, and is seen to be responsible for the quenching. As the strong secondary flow driven by the oscillatory boundary layers is a consequence of the finite geometry of the enclosed cylinder, we have the result of suppressing one confinement effect (wall-localized convection) with another (secondary flow due to the action of the oscillatory boundary layers).

Chapter 5

Onset of Küppers-Lortz-like dynamics in finite rotating thermal convection

Chapters 3 and 4 studied rotating Rayleigh-Bénard convection subject to small amplitude modulations of the rotation rate, exploring notions on how the interaction between oscillatory boundary layers and convection controls the morphology and heat transport of the flow in two different regions in parameter space. The final chapter addresses the problem of convection rotating at a constant rate in order to study closely the development of spatio-temporal chaos immediately beyond onset. It was found that there are two different paths that lead to Küppers-Lortz-like dynamics, one in which the centrifugal force is included (as is necessarily the case for all laboratory experiments) and another in which the centrifugal force is neglected (as is common in theoretical studies on the problem). The two resulting paths to complexity are explored and detailed in this chapter, which has been submitted as Rubio *et al.* (2009*b*) and is a joint work with Juan M. Lopez[1] and Francisco Marques[2]. The media cited in this chapter can be found at $http://mathpost.la.asu.edu/\sim rubio/JFM\_RLM08\_kl\_media/jfm\_RLM08.html$.

5.1 Introduction

Rotating convection has long been a paradigm problem in which to study the emergence of spatio-temporal chaos as such states are observed to appear supercritically with the onset of convection when the fluid layer is rotating at a sufficiently fast angular velocity. These chaotic states found in laboratory and numerical experiments (e.g., see the reviews by Knobloch, 1998; Bodenschatz, Pesch & Ahlers, 2000) are associated with the theoretical predictions of Küppers & Lortz (1969) and Küppers

[1]Department of Mathematics and Statistics, Arizona State University, lopez@asu.edu
[2]Departament de Física Aplicada, Universitat Politècnica de Catalunya, marques@fa.upc.edu

(1970) (KL) who explored the linear stability of straight rolls in a horizontally infinite rotating layer with respect to other straight roll patterns oriented at different angles. They found that for rotation rates above a critical threshold, no steady-state roll patterns were stable, as they lose stability to another set of straight rolls oriented at an angle of about 59 degrees to the first set. Laboratory experiments (of course conducted in finite containers), have shown complexity in both space and time in the guise of patches of re-orienting rolls immediately above onset for rotation rates above the critical rate predicted by Küppers & Lortz, although the mechanism for the onset of spatio-temporal complexity observed in experiments is qualitatively different to that suggested from the infinite layer results (Bodenschatz *et al.*, 1992; Hu *et al.*, 1998). There has been a general expectation that a supercritical bifurcation from the spatially uniform conduction state leads directly to KL-type spatio-temporal convective chaos, and hence that it may be amenable to weakly nonlinear theory (Heikes & Busse, 1980*a*,*b*; Niemela & Donnelly, 1986; Zhong, Ecke & Steinberg, 1991; Tu & Cross, 1992; Rodríguez, Pérez-García, Bestehorn, Fantz & Friedrich, 1992; Cross, Meiron & Tu, 1994; Ponty, Passot & Sulem, 1997; Hu, Ecke & Ahlers, 1997; Hu, Pesch, Ahlers & Ecke, 1998; Cox & Matthews, 2000; Bajaj, Ahlers & Pesch, 2002; Becker & Ahlers, 2006*a*,*b*; Jayaraman, Scheel, Greenside & Fisher, 2006). While this form of spatio-temporal dynamics is inherently associated with the rotation of the system, its analysis has largely been restricted to considerations of the interplay between the Coriolis force and gravitational buoyancy, neglecting the effects of centrifugal accelerations.

It has long been understood that any rotating stratified fluid in a container must exhibit a centrifugally-driven large scale circulation (LSC) (Koschmieder, 1967; Barcilon & Pedlosky, 1967; Rossby, 1969; Brummell, Hart & Lopez, 2000). When the centrifugal acceleration is weak compared to that of gravity, the centrifugally-driven

LSC is negligible compared to the flow driven by gravitational buoyancy for thermal forcing only slightly beyond critical, and the effects of centrifugal force are usually neglected in theoretical treatments and in interpretations of laboratory experiments. However, since the emergence of convection is supercritical, very near onset the small but finite amplitude centrifugally-driven LSC is dominant in organizing the flow. As noted by Rossby (1969): "When the apparatus is rotated, a radial acceleration, which increases with radius, is established.... However, since this radial acceleration destroys the horizontal uniformity, which is a basic assumption in the Bénard convection problem, it is essential that its influence be minimized. Obviously the radial acceleration cannot be eliminated entirely."

There have been previous studies of the impact of centrifugal buoyancy on rotating convection, but the nonlinearity of the problem had restricted the scope of the investigations. Since the basic state is no longer the trivial conduction state, it needs to be determined from a nonlinear simulation of the governing equations. Substantial insight into the problem came from axisymmetric considerations, but the use of the fast rotation limit (to simplify the problem in the asymptotic regime) reduced the applicability of the results, in particular with regards to laboratory experiments (Homsy & Hudson, 1969, 1971; Torrest & Hudson, 1974; Hart, 2000). Whereas most of those efforts were addressing the question of under what conditions does centrifugal buoyancy needed to be accounted for, Koschmieder (1993) took the view that: "Actually of more interest is the question of what is the smallest acceleration ratio [gravitational to centrifugal] at which the centrifugal circulation in an unstably stratified rotating fluid layer can be neglected." In this paper, we address a different issue; we wish to gain a deeper understanding of the onset of thermal convection in an enclosed rotating cylinder, particularly in parameter regimes typically accessed experimentally where KL dynamics are observed near onset and the ratio of centrifu-

gal to gravitational acceleration is small and hence centrifugal buoyancy effects have typically been neglected.

Recently, there has been an interest in studying the effects of centrifugal force with an emphasis on reconciling the results from reduced models with laboratory observations and numerical simulations of the Navier–Stokes–Boussinesq equations (Becker *et al.*, 2006), although it has been noted that incorporating the centrifugal force into a reduced partial differential equations model framework (e.g. Swift-Hohenberg or Ginzburg-Landau models) is difficult if not impossible due to the fact that the additional term makes the Navier-Stokes equations inhomogeneous (Scheel, 2007).

Our earlier studies have shown that even a relatively weak centrifugal force can have a substantial impact on the dynamics of axisymmetric rotating convection, where we restricted the simulations to be axisymmetric (Lopez, Rubio & Marques, 2006*b*). However, onset of three-dimensional instabilities occurs at lower parameter values, and so those results did not address the onset of complicated dynamics in the system. More recently, Lopez & Marques (2009) showed that for cylinders of radius-to-height aspect ratios of order one, the dynamics are governed by a complicated tangle of codimension-two bifurcation points and that the onset of three-dimensional flow is substantially simplified as the relative strength of the centrifugal buoyancy is increased. However, the extensive KL-like dynamics were not evident in such low aspect-ratio cylinders. In this paper, we address these issues in cylinders of aspect-ratios of order ten, where KL-dynamics near onset is prevalent for the rotation rate considered.

In §5.2, the governing equations and the numerical techniques to solve them are discussed. Section §5.3 contains four subsections detailing the linear stability analysis and nonlinear saturation of rotating convection, both neglecting and accounting for the centrifugal force. A discussion of the evidence for the centrifugally-driven large

scale circulation in existing laboratory studies is presented in §5.4, followed by the implications of our numerical study, including a discussion of the role played by the spectral gaps in pattern formation, in §5.5.

5.2 Governing equations and numerical technique

Consider the flow in a circular cylinder, with no-slip boundary conditions, of radius r_0 and depth d, rotating with an angular frequency ω. The endwalls are maintained at constant temperatures, $T_0 - \Delta T/2$ at the top and $T_0 + \Delta T/2$ at the bottom, with an insulating sidewall. The Boussinesq approximation is implemented, treating all fluid properties as constant except for a linear variation of density with temperature in the gravitational and centrifugal buoyancy terms. The system is non-dimensionalized using d as the length scale, d^2/ν as the time scale (ν is the kinematic viscosity), $\nu^2\rho_0/d^2$ as the pressure scale (ρ_0 is the density at mean temperature T_0), and ΔT (the difference in temperature between the top and bottom) as the temperature scale. In a frame of reference rotating at rate ω, the non-dimensional governing equations are

$$(\partial_t + \mathbf{u}\cdot\nabla)\mathbf{u} = -\nabla p + \nabla^2\mathbf{u} + \frac{Ra}{\sigma}(\Theta - z)\mathbf{z} + 2\Omega\mathbf{u}\times\mathbf{z} - \frac{RaFr}{\sigma\gamma}(\Theta - z)r, \qquad (5.1)$$

$$(\partial_t + \mathbf{u}\cdot\nabla)\Theta = w + \sigma^{-1}\nabla^2\Theta, \qquad \nabla\cdot\mathbf{u} = 0, \qquad (5.2)$$

where $\mathbf{u} = (u, v, w)$ is the velocity in cylindrical coordinates (r, θ, z), P is the dynamic pressure, $\mathbf{r}$ is the radial unit vector in the r-direction, $\mathbf{z}$ is the vertical unit vector in the z-direction and Θ is the temperature deviation with respect to the conductive linear temperature profile; the relationship between Θ and the non-dimensional temperature T is given by

$$T = T_0/\Delta T - z + \Theta, \qquad (5.3)$$

where $T_0/\Delta T - z$ is the conductive temperature profile.

There are five independent non-dimensional parameters:

$$\begin{aligned}
&\text{Rayleigh number:} && Ra = \alpha g d^3 \Delta T / \kappa\nu, \\
&\text{Coriolis number:} && \Omega = \omega d^2/\nu, \\
&\text{Prandtl number:} && \sigma = \nu/\kappa, \\
&\text{aspect ratio:} && \gamma = r_0/d, \\
&\text{Froude number:} && Fr = \omega^2 r_0/g,
\end{aligned}$$

where α is the coefficient of volume expansion, κ is the thermal diffusivity and g is the acceleration due to gravity. The boundary conditions (in a frame of reference rotating at rate ω) are:

$$\begin{aligned}
r = \gamma : &\qquad \Theta_r = u = v = w = 0 \\
z = \pm 0.5 : &\qquad \Theta = 0,\ u = v = w = 0.
\end{aligned}$$

The governing equations are solved using the second-order time-splitting of Hughes & Randriamampianina (1998), combined with a pseudo-spectral method for the spatial discretization, utilizing a Galerkin–Fourier expansion in the azimuthal coordinate θ and Chebyshev collocation in r and z. Following Orszag & Patera (1983), we have used the combinations $u_+ = u + iv$ and $u_- = u - iv$ in order to decouple the linear diffusion terms in the momentum equations. For each Fourier mode, the resulting Helmholtz equations for Θ, w, u_+ and u_- have been solved using a diagonalization technique in the two coordinates r and z. The coordinate singularity at the axis ($r = 0$) is treated following the prescription in Fornberg (1998), that guarantees the regularity conditions at the origin needed to solve the Helmholtz equations (Mercader, Net & Falqués, 1991).

The code has been validated on a number of convection problems in rotating cylinders (Lopez, Rubio & Marques, 2006*b*; Marques, Mercader, Batiste & Lopez, 2007;

Lopez, Marques, Mercader & Batiste, 2007; Rubio, Lopez & Marques, 2008, 2009*a*; Lopez & Marques, 2009), establishing resolution requirements over a wide range of parameters. For the cases considered in this paper, $n_r = 64$ and $n_z = 24$ Chebyshev modes in r and z, respectively, were employed except where noted otherwise. For cases where the solution is non-axisymmetric, $n_\theta = 184$ Fourier modes in θ were used. The time discretization used $\delta t \leq 0.0225$ viscous time units. For the majority of the simulations, the Coriolis number $\Omega = 19.7$, Prandtl number $\sigma = 4.5$ and aspect ratio $\gamma = 11.8$ are fixed to correspond to those in relevant experiments (Thompson, Bajaj & Ahlers, 2002), and we consider variations in Ra for Froude number $Fr = 0$ and 8.82×10^{-3} to illustrate the differences between the route to complexity in the idealized case neglecting centrifugal buoyancy and that seen in laboratory experiments with small but finite centrifugal acceleration. Even for $0 < Fr \ll 1$, the centrifugal buoyancy may not be neglected *a priori* compared to gravitational buoyancy since the two act in orthogonal directions (r and z, respectively).

The linear stability analysis, discussed in §5.3, 5.3 and 5.4, was performed via direct numerical stability analysis. First, a steady axisymmetric basic state is computed at some point in parameter space, and its stability is determined by introducing small random perturbations into all azimuthal Fourier modes. For sufficiently small perturbations, the nonlinear couplings between Fourier modes are negligible (below round-off numerical noise) and the growth rates (real parts of the eigenvalues) and structure of the eigenfunctions corresponding to the fastest growing perturbation at each Fourier mode emerge from time evolution. This is tantamount to a matrix-free power method in which the actions of the Jacobian matrices for the perturbations are given by time integration of the Navier-Stokes-Boussinesq equations with the aforementioned initial conditions. Using this method, a direct comparison between stability analysis of the $Fr = 0$ case, whose basic state is the trivial conduction state,

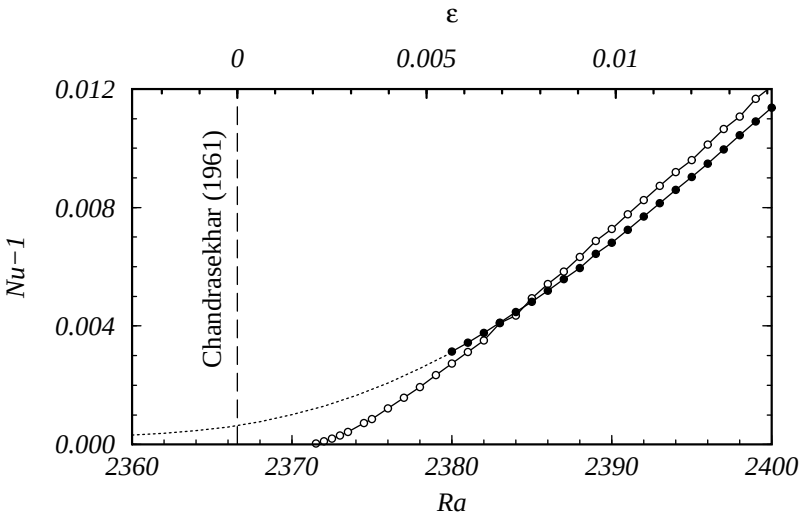

Figure 5.1: Average Nusselt number variation with Ra (and ϵ) for $Fr = 0$ (open circles) and $Fr = 8.82 \times 10^{-3}$ (filled circles), for fixed $\Omega = 19.7$, $\sigma = 4.5$ and $\gamma = 11.8$. The dotted curve shows $Nu - 1$ for the axisymmetric base state with $Fr = 8.82 \times 10^{-3}$ when it is stable to three-dimensional perturbations. The dashed vertical line shows the Chandrasekhar (1961) estimate for onset of convection for $\Omega = 19.7$ in an unbounded layer.

and the $Fr = 8.82 \times 10^{-3}$ case, whose nontrivial basic state must be computed in the axisymmetric subspace, can be made. Furthermore, it is very efficient as the exponential growth or decay of the perturbations is established in a relatively short evolution time (there is no need to evolve the disturbances until they saturate nonlinearly), and by using estimates of the real parts of the eigenvalues from these growth/decay rates for a small number of points in parameter space in the neighborhood of a bifurcation point, linear interpolation of the rates to zero provides a very good estimate of the bifurcation point. Also, the same technique is used to study the linear stability of three-dimensional rotating waves that have been computed in appropriate Fourier subspaces.

5.3 Results

The heat transfer properties of a solution are characterized by the Nusselt number, the ratio between the heat transfer of the solution considered and the heat transfer of the conductive state, both through the top lid. It is given by

$$Nu = -\frac{1}{\pi\gamma^2}\int_{r=0}^{r=\gamma}\int_{\theta=0}^{\theta=2\pi}\frac{\partial T}{\partial z}\Big|_{z=0.5} r\,\mathrm{d}r\,\mathrm{d}\theta\,. \tag{5.4}$$

Figure 5.1 shows the time-averaged Nusselt number as a function of Ra for fully saturated simulations at $\Omega = 19.7$, $\gamma = 11.8$ and $\sigma = 4.5$, both neglecting and incorporating centrifugal force, $Fr = 0$ and $Fr = 8.82 \times 10^{-3}$, respectively. When the centrifugal force is neglected, the average Nusselt number grows supercritically from unity. With the centrifugal force accounted for, the solution is axisymmetric with a Nusselt number greater than unity for $0 < Ra < 2380$. These axisymmetric patterns, described in §5.3, grow smoothly in amplitude near the critical Ra given by Chandrasekhar (1961) resulting in a rounding of the Nusselt number curve. At $Ra = 2380$, this axisymmetric state loses stability to three-dimensional perturbations.

Fr=0 linear stability analysis

The linear stability analysis of the conduction state (neglecting centrifugal buoyancy) was first performed, using a complete basis for the perturbations and allowing for Hopf bifurcations, by Goldstein *et al.* (1993), who showed that there are two types of convective modes, the wall modes consisting of a uniformly precessing wave made up of pairs of hot and cold plumes localized radially near the sidewall, and the bulk modes consisting of convective motions in the interior of the cylinder. When the cylinder is rotating sufficiently fast, wall modes are the first modes to bifurcate from the conduction state as the temperature across the cylinder is increased while the bulk modes are the primary bifurcation modes for slower rotation speeds where KL

dynamics are observed near onset in experiments. It is in this regime where the bulk modes are the primary convective instability that we focus on in this paper. Goldstein *et al.* (1993) observed that the bulk mode eigenfunctions are localized about the rotation axis and that eigenfunctions with even azimuthal wave numbers are invariant to $R_\pi \cdot K$, whereas those with odd azimuthal wave numbers are invariant to R_π. The actions of these symmetries on the velocity and temperature are

$$R_\pi(u, v, w, \Theta)(r, \theta, z, t) = (u, v, w, \Theta)(r, \theta + \pi, z, t), \tag{5.5}$$

$$K(u, v, w, \Theta)(r, \theta, z, t) = (u, v, -w, -\Theta)(r, \theta, -z, t). \tag{5.6}$$

Goldstein *et al.* (1993) also found that small variations in the parameters (Ra, Ω, σ and γ) change which bulk mode is first to bifurcate from the conduction state, and so with small adjustments in the parameters it is relatively easy to find high-codimension points where a number of different bulk modes bifurcate simultaneously. The question naturally arises as to how do these high-codimension bifurcations affect the nonlinear dynamics near onset. Even though this behavior occurs very near onset, due to mode interactions it is highly nonlinear and we shall see that it is not readily amenable to weakly nonlinear treatments.

Figure 5.2(a) shows the marginal stability curves for Fourier modes with azimuthal wavenumbers $m \in [0, 10]$. The complicated interweaving of the curves is hidden by their proximity and all eleven curves appear essentially as a single thick line. In order to disentangle the curves, the same data is re-plotted in figure 5.2(b) in terms of $\epsilon = (Ra - Ra_c(\Omega))/Ra_c(\Omega)$, where $Ra_c(\Omega)$ is the critical Ra at which the conduction state loses stability for a laterally infinite rotating fluid layer (Chandrasekhar, 1961). We also find that for a given Ω, a number of modes of one parity (m odd or even) bifurcate from the conduction state at lower ϵ than any modes of the other parity do, and that which parity is first to bifurcate varies with Ω.

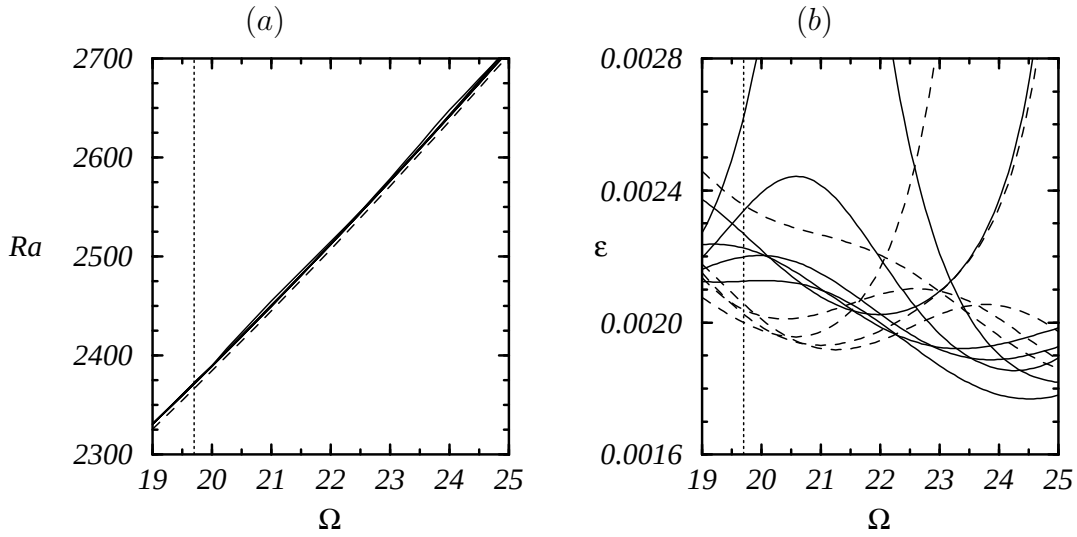

Figure 5.2: (a) Marginal stability curves (solid lines) for the eigenvectors corresponding to Fourier modes 0 to 10 of the linear stability analysis of rotating convection with $\sigma = 4.5$, $\gamma = 11.8$ and $Fr = 0$. A dotted vertical line indicates $\Omega = 19.7$ and a dashed line gives Chandrasekhar's estimate for the onset of convection in an infinite layer. (b) The same data as in (a) given in terms of $\epsilon = (Ra - Ra_c(\Omega))/Ra_c(\Omega)$, where $Ra_c(\Omega)$ is given by Chandrasekhar's estimate for the onset of convection. Even (odd) modes are shown as solid (dashed) lines. The dotted vertical line is at $\Omega = 19.7$.

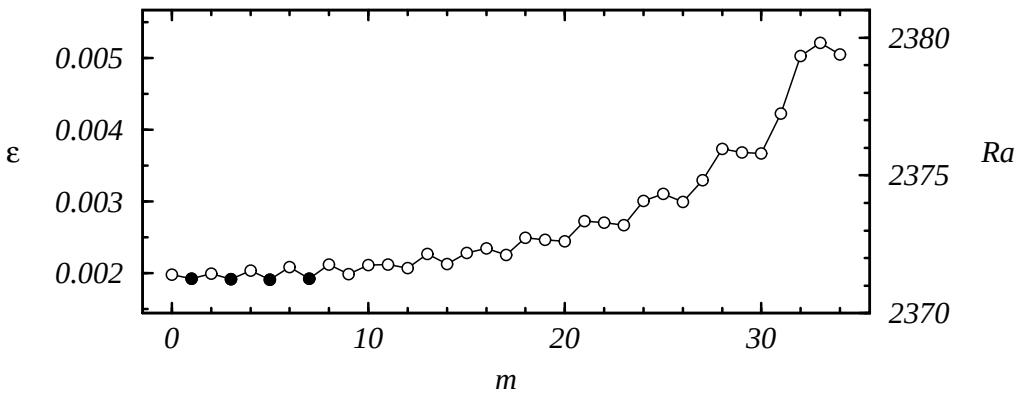

Figure 5.3: Critical thermal driving required for linear stability for eigenvectors corresponding to Fourier modes 0 to 34 at $\Omega = 19.7$ for $\sigma = 4.5$, $\gamma = 11.8$ and $Fr = 0$. The first four modes to bifurcate from the conduction state, in order, are $m = 5$, 3, 7, and 1, and are shown as filled circles.

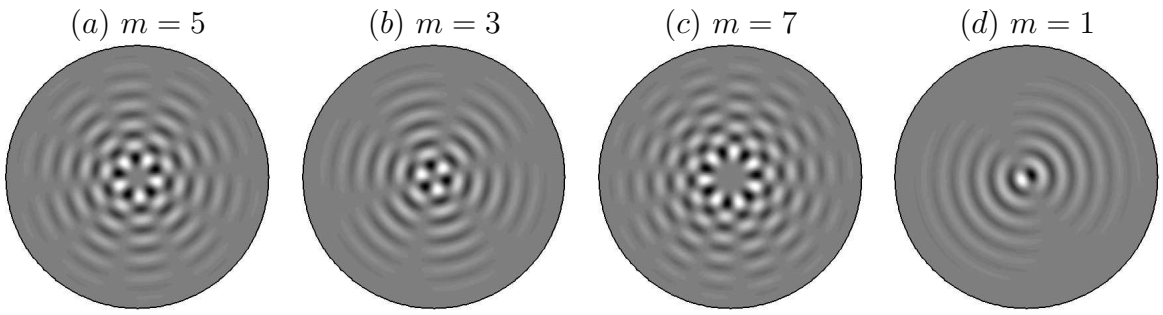

Figure 5.4: Snapshots of the first four eigenmodes to bifurcate from the conduction state as Ra is increased from 2371.2 to 2371.7, for $\Omega = 19.7$, $\sigma = 4.5$, $\gamma = 11.8$ and $Fr = 0$; their azimuthal wavenumbers are indicated.

Figure 5.3 shows the marginal stability curves for Fourier modes with $m \in [0, 34]$ and $\Omega = 19.7$, $\sigma = 4.5$, $\gamma = 11.8$ and $Fr = 0$. For these parameters, our linear stability analysis of the $Fr = 0$ case shows that the $m = 5$ perturbation is the first to bifurcate at $Ra \approx 2371.2$ as Ra is increased, followed rapidly by a number of other odd modes, and then by a set of even modes. The first ten modes bifurcate from the conduction state by $Ra \approx 2371.7$, a variation of about 0.02% in Ra.

Figure 5.4 shows the structure of the first four eigenmodes to bifurcate from the conduction state with increasing Ra. All four eigenmodes precess slowly and closely resemble the bulk modes found in Goldstein *et al.* (1993), with the convection concentrated about the axis, diminishing rapidly with increasing radius. When these are evolved nonlinearly, the saturated solutions, whether computed in the full three-dimensional space or in a subspace corresponding to the representative Fourier mode of the perturbation, are quite different in their spatial and temporal structure from the small amplitude perturbations of the linear stability analysis. Although the spectrum is discrete due to the finite confined geometry of the problem, the very small gaps in the spectrum make the application of weakly nonlinear dynamical systems approaches problematic. Since there are several distinct modes with very similar growth rates

near onset, one cannot *a priori* assume that the mode which first bifurcates will saturate nonlinearly without influence from nearby decaying modes. The whole concept of a low-dimensional center manifold describing the weakly nonlinear dynamics near onset becomes questionable due to the tight spectral gaps. With several near-critical modes, in principle, a high-dimensional center manifold theory could be developed. When there are only two modes near critical, codimension-two dynamics have been successfully described and compared with experiments and fully nonlinear simulations in a number of fluids problems (e.g. Barkley, Tuckerman & Golubitsky, 2000; Marques, Lopez & Shen, 2002; Lewis & Nagata, 2003; Lopez, Cui & Lim, 2006*a*; Avila, Belisle, Lopez, Marques & Saric, 2008), and there are examples of codimension-three double Hopf bifurcations as well (Marques, Gelfgat & Lopez, 2003), but with several such modes, the center manifold description becomes unwieldly and impractical.

Fr =0 secondary instabilities

When solutions at $\Omega = 19.7$, $\sigma = 4.5$, $\gamma = 11.8$ and $Fr = 0$ with Ra just above that required for linear instability of the conduction state are allowed to saturate, exceedingly long transient times are encountered. Snapshots of the nonlinearly saturated temperature perturbation Θ at $Ra = 2372$, 2373 and 2374 are shown in figures 5.5(a), (b) and (c), respectively. These solutions were time integrated to over $158,000$ viscous times, corresponding to over 22 days in equivalent laboratory experiments. All these solutions are very different from the pure eigenmodes shown in figure 5.4. At $Ra = 2372$, a square lattice pattern centered and localized about the axis of rotation slowly precesses in the retrograde direction, exhibiting a barely noticeable degree of roll switching (movie 1 available in the online version shows this evolution). It is difficult to say whether this solution has evolved beyond its initial transient and determining the characteristics of this potentially quasiperiodic state would require a

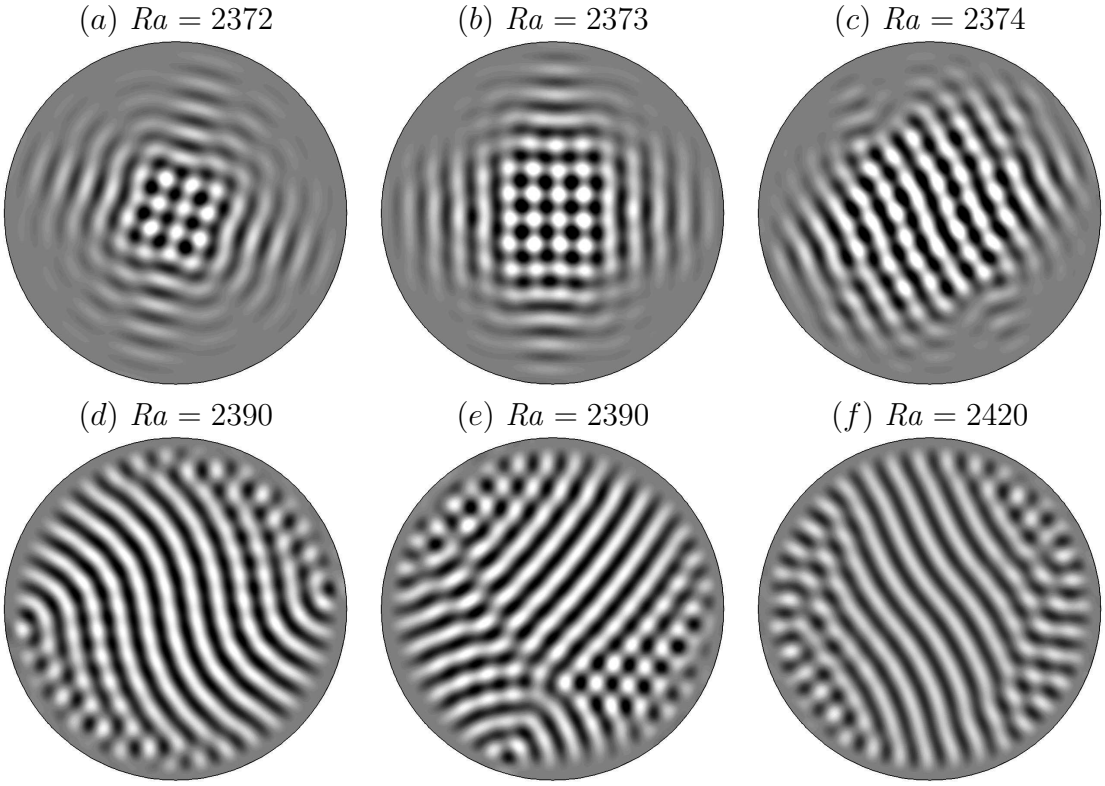

Figure 5.5: Snap-shots of the temperature perturbation Θ at mid-height $z = 0$ for $\Omega = 19.7$, $\sigma = 4.5$, $\gamma = 11.8$, $Fr = 0$, and indicated Ra, with color levels of $\Theta \in [-5\epsilon, 5\epsilon]$ (black to white).

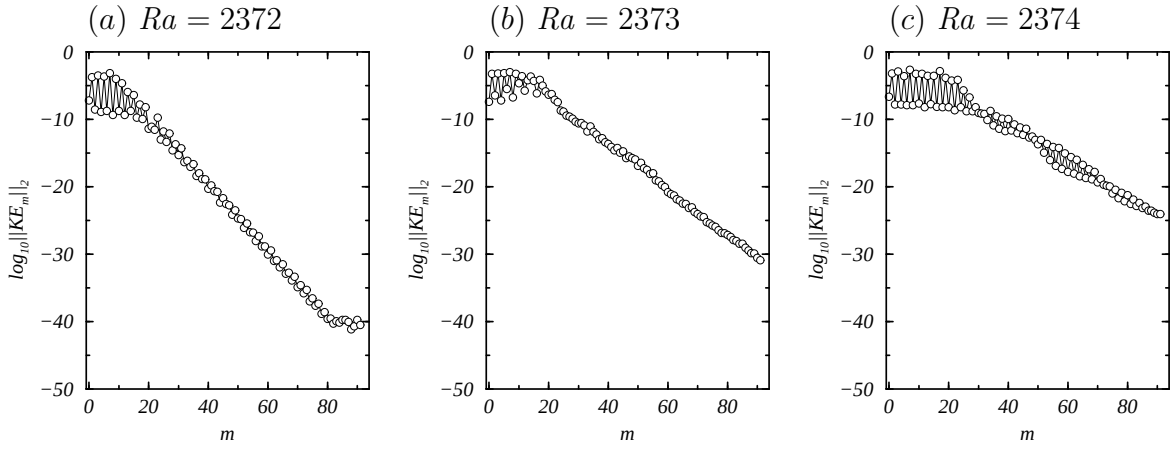

Figure 5.6: L2-norm of the time-averaged kinetic energy associated with Fourier modes $m \in [0, 91]$ for simulations with $\Omega = 19.7$, $\sigma = 4.5$, $\gamma = 11.8$, $Fr = 0$ and Ra as indicated. Time-averaging was done over 60,000 viscous times for each solution.

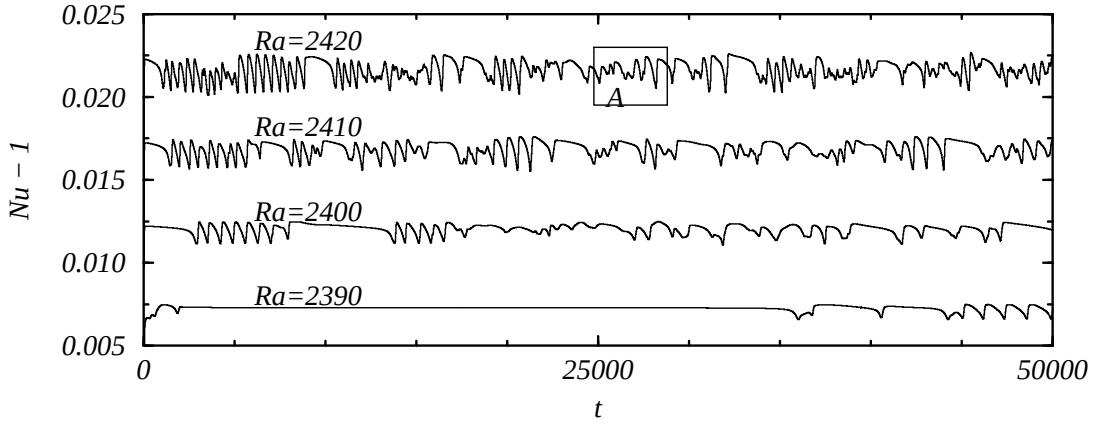

Figure 5.7: Time-series of $Nu - 1$ at $Fr = 0$, $\Omega = 19.7$, $\sigma = 4.5$ and $\gamma = 11.8$, for Ra as indicated.

time integration well beyond the $158,000$ viscous times already computed. We also note that a Fourier decomposition of this state shows that it has significant power in at least six Fourier modes $m \in [0, 91]$, as can be seen in figure $5.6(a)$ which shows the L2-norm of the kinetic energy associated with each Fourier mode of the saturated solutions shown as figure 5.5 (a), (b) and (c), where the L2-norm of a scalar function, f, is given by,

$$||f||_2 = \left[\int_{-1/2}^{1/2} \int_0^{2\pi} \int_0^{\gamma} f^2(r, \theta, z) r dr d\theta dz \right]^{1/2}. \tag{5.7}$$

At slightly higher $Ra = 2373$, the square lattice fills the fluid layer to a larger radius and roll switching within the confines of the square lattice is clearly seen in movie 2. By $Ra = 2374$, the pattern fills the entire cell and a seemingly quasiperiodic roll-switching state is observed (see movie 3). The growing extent of the square lattice for $Ra = 2373$ and 2374 is necessarily accompanied by an increase in amplitude of the higher Fourier modes required to resolve the square pattern at increasing radius, as can be seen in figures $5.6(b)$ and (c). At higher $Ra \in [2386, 2392]$, s-shaped roll

patterns slowly precess for long times before more complicated behavior in space and time sets in. This can be seen in the $Ra = 2390$ time series shown in figure 5.7, where the roll pattern shown in figure 5.5(d) persisted for over $25,000$ viscous times before its R_π-rotational symmetry was lost, resulting in states such as those in figure 5.5(e) with lines of defects gliding through the layer. Solutions at higher Ra exhibited global roll-switching early in their time integrations, but all took on more complicated temporal structure at later times as indicated by the $Ra = 2400$, 2410 and 2420 time series shown in figure 5.7. For both types of patterns, with either long stretches of quasi-steady behavior or global roll-switching, onset of complex time behavior is associated with a breaking of the R_π symmetry with lines of defects propagating relatively quickly across the cylinder in arbitrary directions.

Qualitative features of patterns such as figure 5.5(f), including defects originating at the sidewall and gliding through the fluid layer leading to patches of re-orienting rolls, have been reported in simulations of the Swift–Hohenberg equations in finite cylinders (Fantz *et al.*, 1992). However, we are not aware of any reports of the localized square patterns shown in figures 5.5(a, b) from simulations of reduced equation models of rotating convection. Localized square patterns in rotating convection have been observed experimentally (Bajaj *et al.*, 1998), but they have presented something of an enigma (Ahlers, 2006) when trying to reconcile them with theory based on the assumption of horizontal periodicity. Theoretical treatments of square periodic lattices have shown them to be unstable, and yet laboratory experiments and numerical simulations of the Navier–Stokes–Boussinesq equations in confined rotating cylinders (neglecting centrifugal buoyancy) have found states in which localized square patterns in the interior coexist with wall-localized plumes near the onset of bulk convection (Bajaj *et al.*, 1998; Sánchez-Álvarez *et al.*, 2005; Marques & Lopez, 2008). However, localized square patterns without the prior presence of wall-localized plumes had not

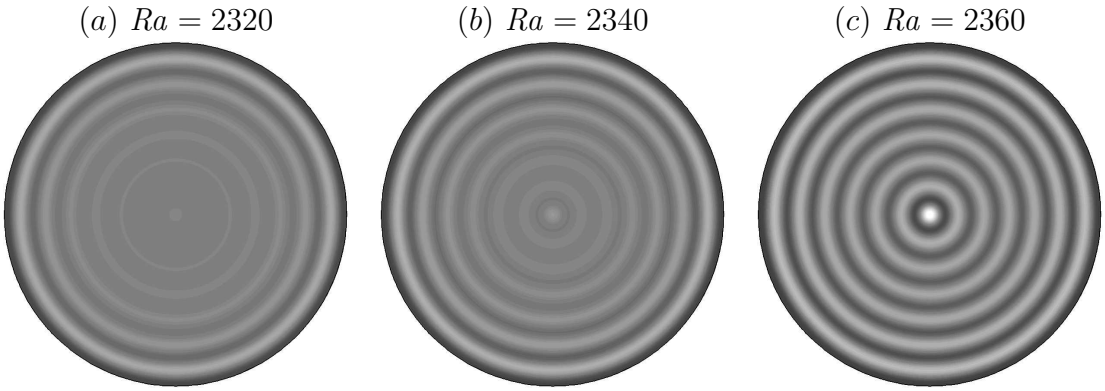

Figure 5.8: Temperature perturbation Θ at $z = 0$ for $\Omega = 19.7$, $\sigma = 4.5$, $\gamma = 11.8$, $Fr = 8.82 \times 10^{-3}$, and Ra as indicated. Five positive (light) and five negative (dark) color levels are shown for $\Theta \in [-0.02, 0.02]$.

been previously reported in either laboratory experiments or numerical simulations. Of course, it is not clear whether there is any correspondence between the square tessellations in horizontally periodic problems and the patterns with locally four-fold symmetry found in laterally confined rotating convection. In our opinion, the two patterns are unrelated. The square patterns localized about the axis near onset appear to be a nonlinear combination of the first several Fourier eigenmodes to bifurcate from the conduction state (the first four eigenmodes are shown in figure 5.4).

Fr =0.00882 linear stability analysis

When centrifugal force is not neglected, any nonzero Ra will result in a large scale circulation in the fluid layer. However, for Fr small and Ra sufficiently above that required for three-dimensional convection, this fluid motion is quite weak compared to the gravitational buoyancy-driven flow, and often can be ignored. In theoretical models of rotating convection in infinite or periodic layers, centrifugal buoyancy must be ignored as it varies with the radial distance from the axis of rotation, violating the underlying assumptions of either horizontal translation invariance or periodicity; the

location of the axis of rotation becomes distinguished and the centrifugal buoyancy becomes unbounded at large distances from the rotation axis. Numerical simulations neglecting centrifugal force can agree quite well with laboratory experiments provided that the parameter regime explored is sufficiently beyond onset of gravitational buoyancy-driven convection, depending on the ratio of centrifugal to gravitational accelerations. However, the finite amplitude centrifugally-driven LSC is necessarily the dominant flow very near the supercritical onset of gravitational buoyancy-driven convection. For $\Omega = 19.7$, $\sigma = 4.5$, $\gamma = 11.8$ and $Fr = 8.82 \times 10^{-3}$ (corresponding to the actual centrifugal force observed in similar laboratory experiments) this LSC is a target pattern that varies with parameters. Some examples are shown in figure 5.8. For small Ra, circular concentric rolls form at the periphery of the cylinder, strengthening and developing new rolls into the interior with increasing Ra, until near the onset of three-dimensional convection where a target pattern fills the entire cylinder. The same development of the centrifugally-driven LSC has been reported by Daniels (1980) from consideration of a simplified rotating convection problem with stress-free boundary conditions and restricted to steady axisymmetric flow using a perturbation analysis, as well as in the laboratory experiments of Koschmieder (1967, 1993).

For $Ra \in [2370, 2394]$, target patterns were computed in the axisymmetric subspace and then their stability was determined by subjecting them to random perturbations in Θ with L2-norm of order 10^{-10} across all Fourier modes. The linear stability analysis consisted of monitoring the exponential growth and decay of the amplitude of the perturbations associated with each Fourier mode. While the perturbations have L2-norm of order 10^{-10}, the nonlinear coupling between them is of the order of 10^{-20}, ensuring that the nonlinear time evolution behaves as a direct linear stability analysis plus an error ten orders of magnitude smaller than any of the relevant quantities. Time integration is tantamount to a generalization of the

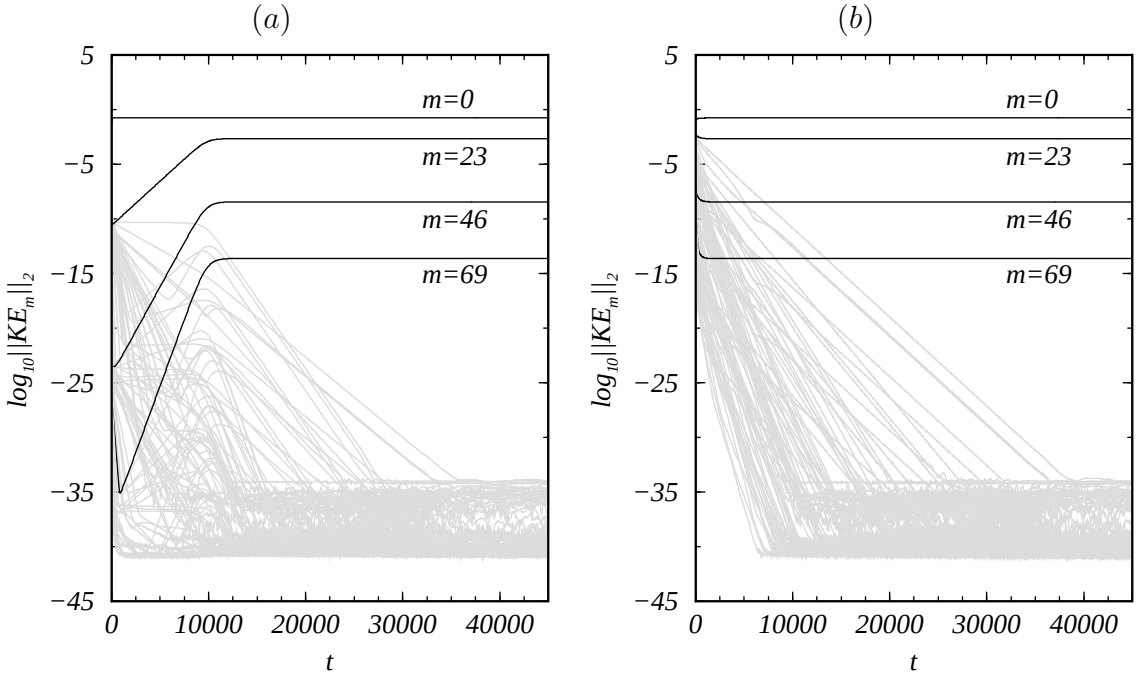

Figure 5.9: Time series of the L2-norm of the kinetic energy associated with each Fourier mode for simulations with $Ra = 2380$, $\Omega = 19.7$, $\sigma = 4.5$, $\gamma = 11.8$ and $Fr = 8.82 \times 10^{-3}$. (a) Saturation from below; the initial condition was an axisymmetric target pattern with a random perturbation of order 10^{-10} across all Fourier modes. (b) Decay from above; the initial condition was a fully developed solution with $Ra = 2400$ as shown in figure 5.13(c). In both cases the modal energies with $m = 0$, 23, 43, and 69 are shown as black lines and all other modal energies are shown as gray lines.

power method for finding eigenvalues with largest positive real part. After temporal evolution of a few viscous adjustment times, we find that for each Fourier mode the eigenfunction associated with the eigenvalue with largest real part clearly emerges. A typical time series resulting from this process is shown in the first few thousand viscous times of figure 5.9(a), which shows the linear growth and decay of perturbations associated with Fourier modes $m \in [1, 92]$ followed by the nonlinear saturation of an $m = 23$ rotating wave (described in detail in the following section). The results of the linear stability analysis are shown in figures 5.10 and 5.11, consisting of the critical

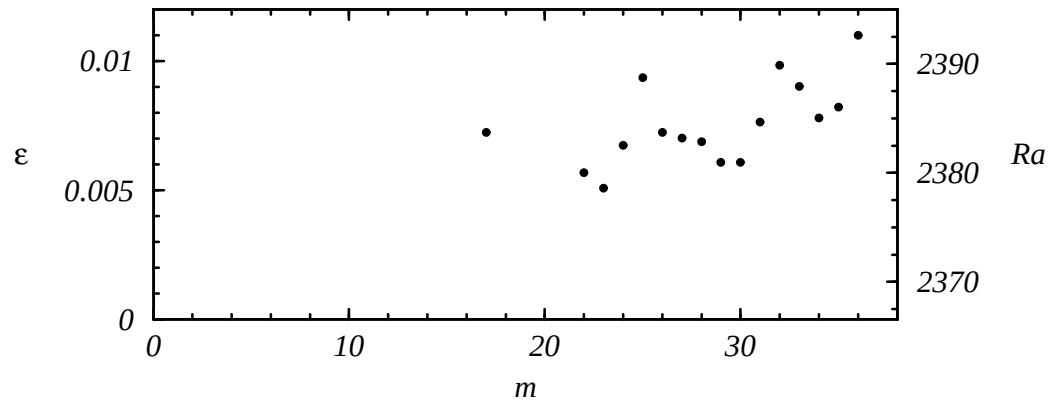

Figure 5.10: Critical Ra for disturbances with azimuthal wavenumber m at $\Omega = 19.7$, $\sigma = 4.5$, $\gamma = 11.8$ and $Fr = 8.82 \times 10^{-3}$.

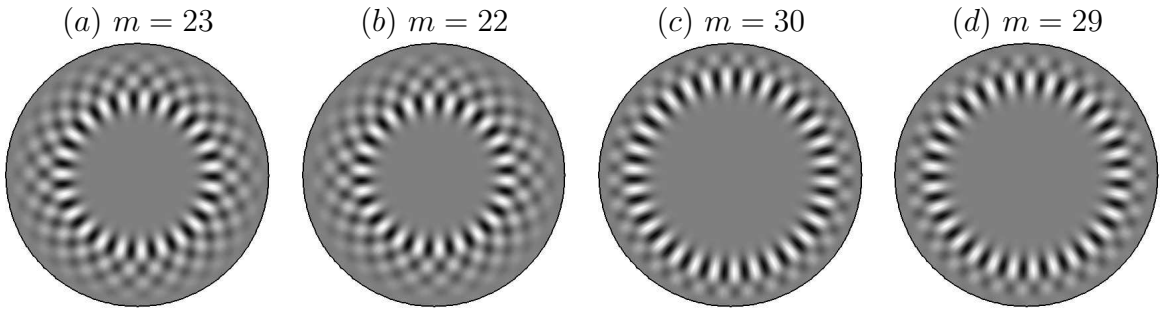

Figure 5.11: Snapshots of the four eigenmodes with fastest growth rate to bifurcate from the axisymmetric basic state at $Ra = 2380$, $\Omega = 19.7$, $\sigma = 4.5$, $\gamma = 11.8$ and $Fr = 8.82 \times 10^{-3}$.

Ra values for $\Omega = 19.7$, $\sigma = 4.5$, $\gamma = 11.8$ and $Fr = 8.82 \times 10^{-3}$ and the eigenfunctions corresponding to the first four non-axisymmetric perturbations to bifurcate from the basic state as Ra is increased. The first non-axisymmetric perturbation to bifurcate is the $m = 23$ perturbation shown in figure 5.11 at $Ra = 2378.6$, followed by the $m = 22$ perturbation at $Ra = 2380.02$. The critical Ra is determined from computing the growth rates from time series such as figure 5.9(a) at a few different Ra bracketing the zero growth rate value and then estimating the critical Ra using linear interpolation to zero growth rate.

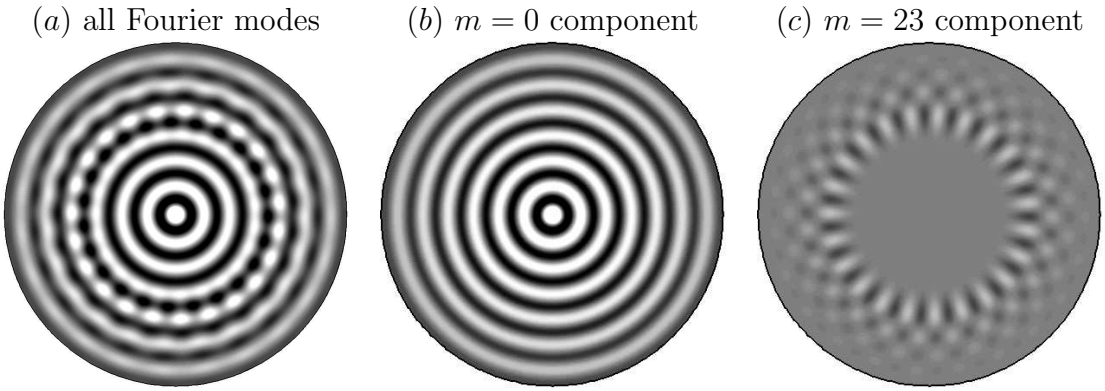

Figure 5.12: Temperature perturbation Θ at $z = 0$ for $Ra = 2380$, $\Omega = 19.7$, $\sigma = 4.5$, $\gamma = 11.8$ and $Fr = 8.82 \times 10^{-3}$; (a) shows the complete solution, (b) shows its axisymmetric component, and (c) shows its $m = 23$ component. Five positive (light) and five negative (dark) color levels are shown for $\Theta \in [-5\epsilon, 5\epsilon]$.

Unlike the $Fr = 0$ case, when Fr is set to that of the analogous laboratory experiments, a single Fourier mode solution emerging from a Hopf bifurcation is observed immediately at the onset of three-dimensional convection. For the parameter space explored, an $m = 23$ rotating wave was observed; a snap-shot of the nonlinear saturated solution is shown in figure 5.12(a). The time-series of this evolution (figure 5.9a) shows that the $m = 23$ rotating wave fully saturates in about 12,000 viscous times. Very near the Hopf bifurcation, the saturated solution is essentially a superposition of the axisymmetric basic state and a scalar multiple of the $m = 23$ eigenmode. Figure 5.12(b) is the axisymmetric $m = 0$ component of the nonlinear saturated rotating wave shown in part a, which is essentially the underlying LSC, and part c is the $m = 23$ Fourier component of the rotating wave which essentially has the same structure as the $m = 23$ Hopf eigenmode shown in figure 5.11(a).

Fr =0.00882 secondary instabilities

Near $Ra = 2382$, the $m = 23$ rotating wave described above loses stability to an $m = 6$ Fourier mode perturbation in a supercritical secondary Hopf bifurcation (this

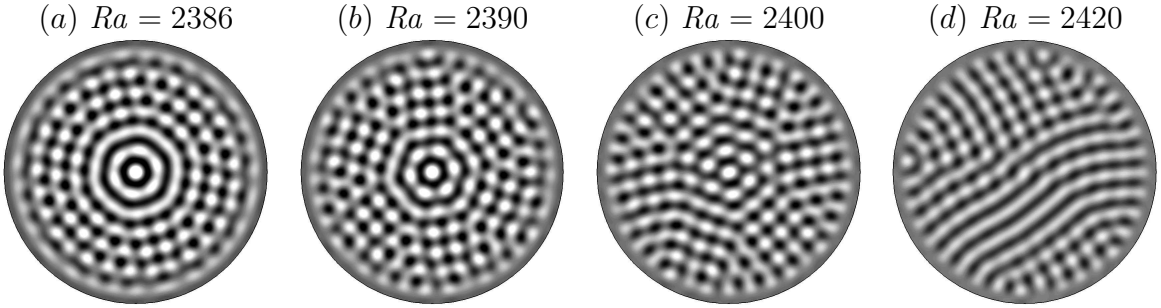

Figure 5.13: Temperature perturbation Θ at $z = 0$ for $\Omega = 19.7$, $\sigma = 4.5$, $\gamma = 11.8$, $Fr = 8.82 \times 10^{-3}$ and indicated Ra, with color levels of $\Theta \in [-5\epsilon, 5\epsilon]$ (black to white).

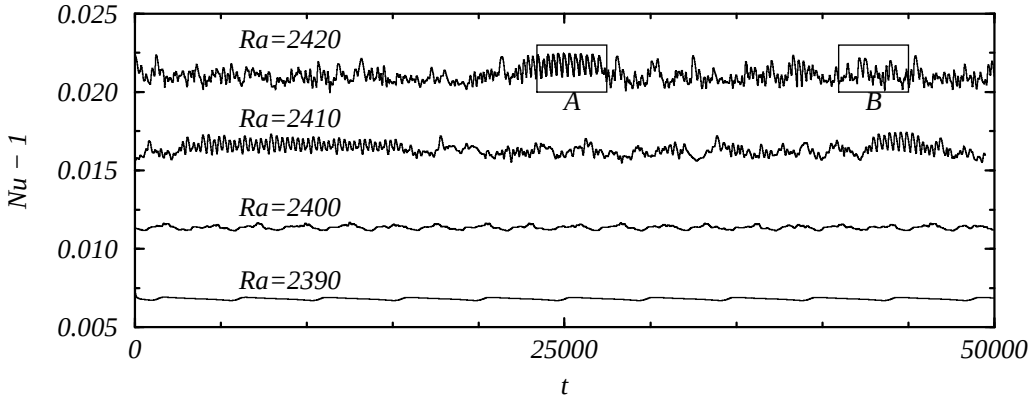

Figure 5.14: Time-series of $Nu - 1$ at $\Omega = 19.7$, $\sigma = 4.5$, $\gamma = 11.8$, $Fr = 8.82 \times 10^{-3}$ and Ra as indicated.

was determined using the direct numerical stability analysis using the $m = 23$ rotating wave as the basic state). Temporal evolution to the nonlinear saturated state results in a hexagonal pattern localized about the axis of rotation, giving a mixed mode modulated rotating wave with $m = 23$ and $m = 6$.

Increasing Ra slightly from 2382 to 2386, the modulated rotating wave solution exhibits a ratcheting behaviour, similar to that observed by Gorman *et al.* (1996) and analyzed by Golubitsky, LeBlanc & Melbourne (2000) in circular flames. A snap-shot is shown in figure 5.13(a). All aspects of the dynamics are not the same as

in the flame experiment which has $O(2)$ symmetry in azimuth, whereas the rotating convection problem only has $SO(2)$ symmetry in azimuth (see Crawford & Knobloch, 1991; Knobloch, 1994, 1996, for discussions of the dynamic consequences of these two symmetries, particularly in the context of hydrodynamic instabilities), but the ratcheting is very similar. A snapshot of the ratcheting state is shown in figure 5.13(b), but the spatio-temporal nature of this state at $Ra = 2390$ is better appreciated from movie 4 (available in the online version).

By $Ra = 2400$, roll-switching behaviour is observed on top of the underlying ratcheting hexagonal lattice found at the slightly lower Ra. A snapshot of one such solution is shown in figure 5.13(c) and movie 5 (available online) illustrates the dynamics. With increasing Ra, the dynamics resemble the KL-like dynamics described by experimentalists, where roll-switching domain chaos is observed. A snapshot of a typical solution is shown in figure 5.13(d). However, the time series for this state shows excursions to states exhibiting simpler temporal behavior, as highlighted in the box labelled A in figure 5.14 for $Ra = 2420$ (movie 6 shows the temporal evolution of this state over the time indicated by box A). Movie 7 shows the more typical dynamic behavior of this flow state over the time marked by box B in figure 5.14. For comparison, the flow state with all the same parameters, except for $Fr = 0$, is shown in movie 8; it corresponds to time evolution over the period shown by box A in figure 5.7. At $Ra = 2420$, the spatio-temporal characteristics are almost indistinguishable between the $Fr = 0$ and the $Fr = 8.82 \times 10^{-3}$ solutions, except that in the $Fr \neq 0$ case, the axis $r = 0$ remains a distinguished point and the pattern shows intermittent circular organization at the axis.

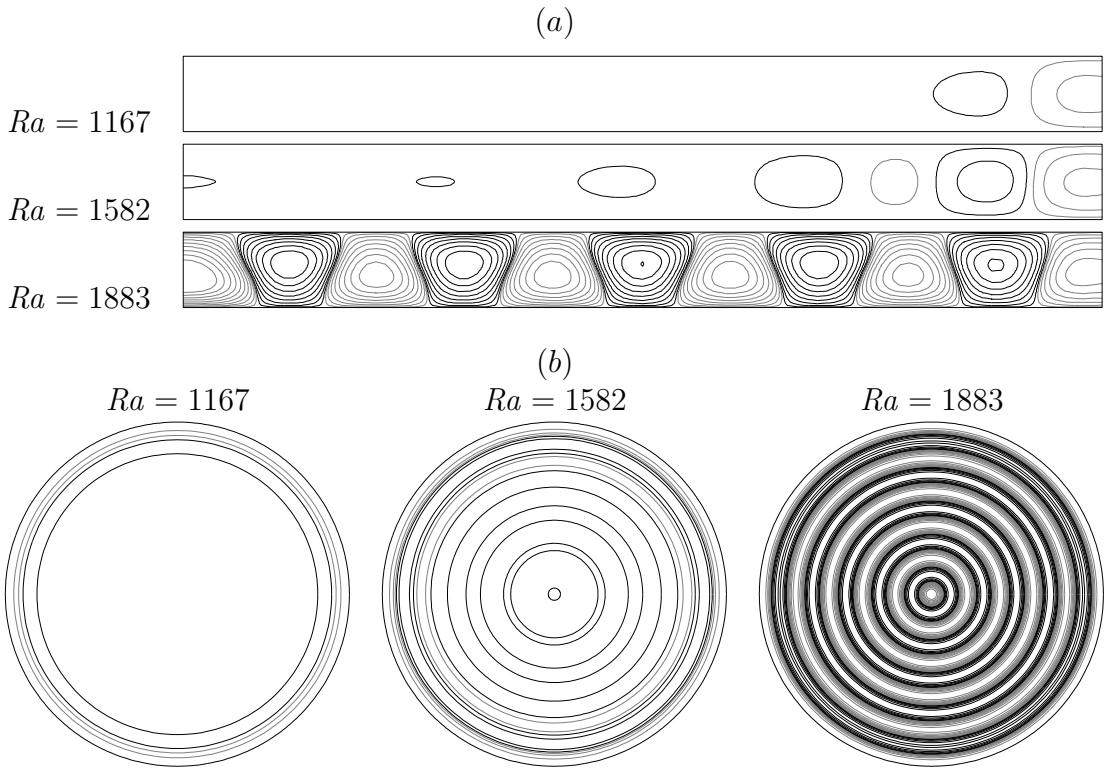

Figure 5.15: Contours of Θ for numerical simulations following Koschmieder (1967) with $\Omega = 1.48$, $\sigma = 877$, $\gamma = 10.3$ and $Fr = 0.025$. (a) Meridional planes $r \in [0, \gamma]$, $z \in [-1/2, 1/2]$ of solutions with indicated Ra. (b) Contours of Θ in a horizontal plane with $z = 0$ for the cases shown in (a). Ten positive (black) and negative (gray) contours are spaced quadratically for $\Theta \in [-0.2, 0.2]$.

5.4 Experimental evidence of the centrifugally-driven large scale circulation

So far, our discussion has been focused on parameter regimes of typical laboratory experiments in which the Coriolis force was dominant over the centrifugal force, and we have seen that if the centrifugal force, although small, is not neglected, the large scale circulation (LSC) smoothly evolves into a target pattern near the onset of gravitational buoyancy-driven convection. Such a development has been described from a series of laboratory experiments reported by Koschmieder (1967) in which the parameter regime was carefully selected so as to have the centrifugal buoyancy dominant

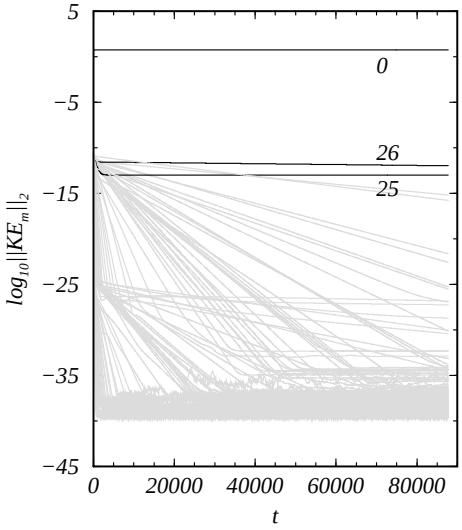

Figure 5.16: Time series of the L2-norm of the kinetic energy associated with each Fourier mode for a simulation with $Ra = 1883$, $\Omega = 1.48$, $\sigma = 877$, $\gamma = 10.3$ and $Fr = 0.025$. The initial condition was an axisymmetric target pattern with a random perturbation of order 10^{-10} across all Fourier modes. The modal energies with $m = 25$ and 26 are shown as black lines and all other modal energies are shown as gray lines.

over Coriolis. The patterns he observed are consistent with the axisymmetric flow solutions of Torrest & Hudson (1974) and Daniels (1980), even though the experimental apparatus used for the study had substantial issues in controlling the thermal boundary conditions at the sidewall which resulted in the stabilization of otherwise unstable axisymmetric patterns in the non-rotating case. Despite the sidewall issues, the rationale for the emergence of the target patterns being due to the centrifugally-driven LSC (Koschmieder, 1993) is consistent with the idealized results of Torrest & Hudson (1974) and Daniels (1980). To further explore this, we have conducted a number of simulations in the parameter regime investigated by Koschmieder (1967), with insulating sidewall boundary condition, and have found excellent agreement with his observations. A sample of those simulations are given in figure 5.15. We have translated his dimensional parameters into our non-dimensional parameters, and the

cases in the figure correspond to a moderate Froude number sequence. The parameters are aspect-ratio $\gamma = 10.3$, slow rotation with Coriolis number $\Omega = 1.48$, very high Prandtl number $\sigma = 877$, and Froude number $Fr = 0.025$ (about three time larger than that of the results presented in the previous section). The three Ra cases shown in the figure correspond to those in figures 8, 9 and 10 of Koschmieder (1967), and show the same development of the target pattern with increasing Ra, and in particular the same number of concentric rolls. We have also conducted a direct numerical linear stability analysis of the $Ra = 1883$ case and found that this solution is stable to three-dimensional perturbations, although perturbations with Fourier modes $m = 25$ and 26 have nearly zero decay rates. The $m = 25$ perturbation is decaying exponentially with a decay constant of -4.2357×10^{-7} per viscous time and the $m = 26$ has a decay constant of -4.7873×10^{-6} per viscous time; see figure 5.16. In a photo of a similar case with $\Omega = 2.96$ and $Fr = 0.1$ in Koschmieder (1967), a high wavenumber perturbation is evident, much like the $m = 23$ waviness we describe in figure 5.12(a).

There is also evidence of the centrifugal buoyancy in the more typical parameter regimes explored experimentally where Coriolis dominates over centrifugal force, but due to the presence of other effects, it has been difficult to unambiguously identify this with centrifugal buoyancy without detailed simulations. Bajaj *et al.* (2002) report the intermittent observation of target patterns near onset, and even beyond onset where the dynamics are KL-like, the origin is also intermittently distinguished, much as we observe in movies 6 and 7, whereas for the same parameters but with $Fr = 0$, movie 8 does not show any distinguished feature at $r = 0$.

An interesting exercise looking at long time averages of KL-type dynamics was conducted by Ning *et al.* (1993), although their intent at the time was not motivated by considerations of the centrifugal buoyancy. In a regime displaying KL-like dynamics (together with a wall mode), they took very long time sequences of shadow graph

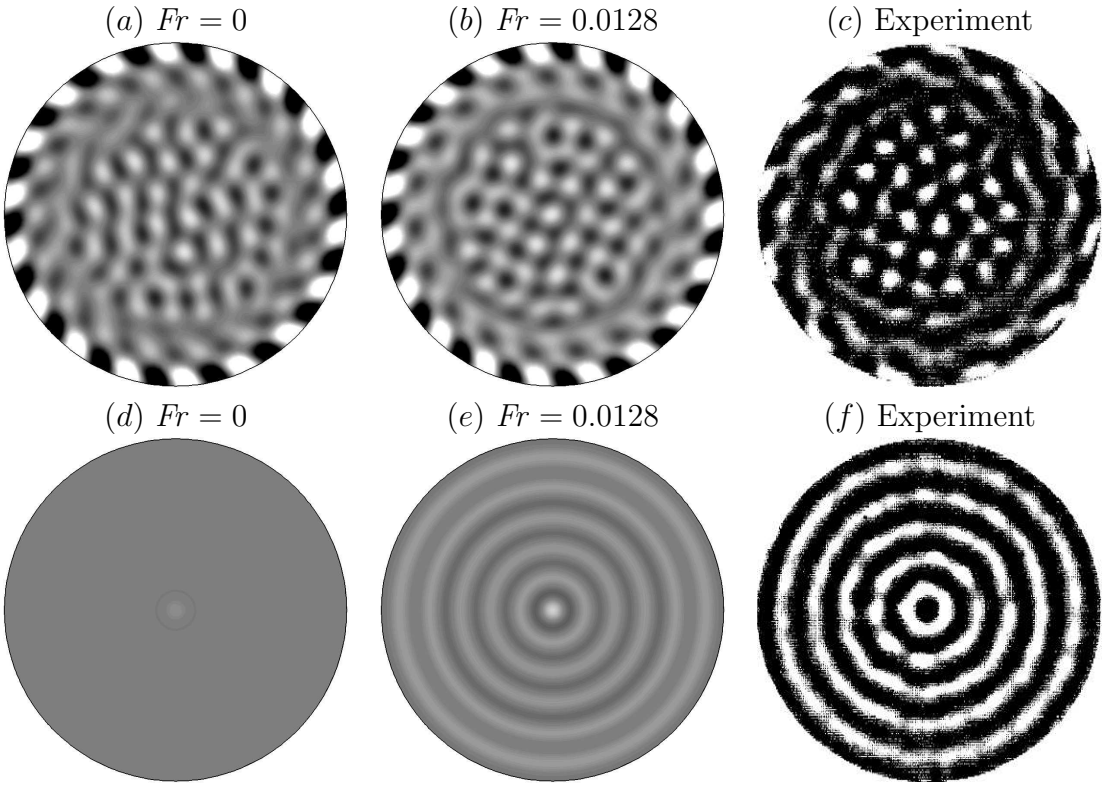

Figure 5.17: Rotating convection in a cylinder with $Ra = 2.08 \times 10^5$ ($\epsilon = 0.053$), $\Omega = 1090$, $\sigma = 6.4$, $\gamma = 2.5$ and $Fr = 0$ or $Fr = 0.0128$; (a)–(c) are snap-shots of a KL-like state with a precessing wall mode, and (d)–(e) are the corresponding long-time averages. The experimental results are from Ning *et al.* (1993). A grid resolution of $n_r = 64$, $n_z = 32$ and $n_\theta = 220$ was used in the simulations.

images and time averaged them. As the flow state is not periodic, very long time averages were needed, and these converged to a target pattern. This was consistent with what one would expect in a circular container, that the time average should have the same symmetry as the container, but what perhaps was not appreciated at the time was the spatial structure of the time-averaged pattern; it has the same structure as the (unstable) axisymmetric LSC at that point in parameter space. To show this, we have computed the same case with the corresponding values of the parameters ($Ra = 2.08 \times 10^5$, $\gamma = 2.5$, $\Omega = 1090$, $\sigma = 6.4$ and $Fr = 0.0128$, where Ra was cal-

culated by considering the given reduced Rayleigh number, $\epsilon = 0.053$, and assuming Ra_c given by Chandrasekhar's estimate for the onset of bulk convection) as well as with $Fr = 0$, and determined the long-time averages of these (taking longer time averages until they converged). For these calculations $n_r = 64$ and $n_z = 32$ Chebyshev modes were used in r and z, respectively, and $n_\theta = 220$ Fourier modes were used in θ. The results, along with the experimental results are shown in figure 5.17. It is clear that the $Fr \neq 0$ average is the LSC and it agrees with the long-time average from the experiment, whilst the $Fr = 0$ average is the conduction state which is horizontally featureless. So, by taking long-time averages, Ning *et al.* (1993) provided experimental evidence of the centrifugally-driven LSC in a Coriolis dominated parameter regime. We note that the azimuthal wavenumber of the wall mode component of the flow differs between the experiment and our simulation, but this is not surprising as in the high Ω regime there is a very large multiplicity of stable states due to a wide Eckhaus–Benjamin–Feir band, and which state is obtained is very sensitive to initial conditions (Lopez *et al.*, 2007; Marques & Lopez, 2008).

5.5 Conclusions

A detailed analysis of the onset of the Küppers–Lortz dynamics in a finite rotating cylinder has been conducted, and particular attention has been placed on the effect of the centrifugal buoyancy in parameter regimes corresponding to typical experimental setups where the Coriolis force dominates over the centrifugal force. In order to assess the importance of the centrifugal buoyancy, we have first analyzed the Froude number $Fr = 0$ case where centrifugal effects are neglected, and then compared it with small $Fr \neq 0$ solutions corresponding to actual values of the Froude number in laboratory experiments.

In both the $Fr = 0$ and $Fr \neq 0$ cases, the first instability of the base flow is a Hopf

bifurcation breaking the azimuthal symmetry with an eigenmode that corresponds to a rotating wave, as predicted by dynamical systems theory. However, in the $Fr = 0$ case, a large packet of eigenvalues bifurcate in a very narrow range of parameters. In terms of a reduced Rayleigh number $\epsilon = (Ra - Ra_c(\Omega))/Ra_c(\Omega)$, the first ten eigenvalues bifurcate in an ϵ range of 2×10^{-4}, well below the experimental uncertainties in the parameter values. Even more important is the fact that the bifurcated solutions saturate into states consisting of localized square patterns, completely different from the individual structure of the bifurcating eigenmodes. These two facts make analyses based on reduced partial differential equations models or even normal forms/center manifold reductions inappropriate. The analysis presented here, based on direct numerical simulation of the Navier–Stokes–Boussinesq equations, although costly from a numerical point of view due to the proximity to the bifurcation point and the corresponding extremely long transients, is free from the above mentioned difficulties of the reduced models. This direct analysis has shed light on the nature of the localized square patterns, which had been previously observed in experiments near onset as well as in other numerical simulations, that the reduced models are unable to explain. These patterns are associated with a tight packet of several eigenvalues bifurcating almost simultaneously, and correspond to saturated states involving significant contributions from all the eigenmodes in the packet. The localized square patterns can be clearly observed in an ϵ range of about 2×10^{-3}, one order of magnitude larger than the interval in which the spectral packet bifurcates. For larger ϵ values, it evolves to more complex patterns which increasingly resemble Küppers–Lortz dynamics as ϵ increases beyond about 8×10^{-3}. This complex scenario at the onset of convection, involving a broad band of eigenmodes, is what transpires when centrifugal buoyancy is ignored by taking $Fr = 0$.

For non-zero Froude numbers, even as small as $Fr \lesssim 0.01$, corresponding to typical

experimental values, a completely different transition scenario is observed. The base state is no longer the conductive state, but an axisymmetric target pattern. The onset of three-dimensional convection is delayed up to $\epsilon = 2 \times 10^{-3}$, and the spectral gap between the different bifurcating eigenvalues is larger: the distance between the two first bifurcating eigenvalues is now 7×10^{-4}, more than three time the size of the range of the first 10 bifurcating eigenvalues in the $Fr = 0$ case. As a result, the bifurcating eigenmode saturates nonlinearly to a state with the same structure as the eigenmode, and subsequent changes in the nonlinear solutions correspond to secondary bifurcations. Here, the normal form approach is applicable and useful, although its region of validity is narrow. With increasing ϵ, a succession of different complex states emerge, resulting in Küppers–Lortz dynamics for ϵ greater than about 2×10^{-2}.

The main conclusions of this analysis are the following. First, for values of Fr that have usually been considered small enough to neglect centrifugal effects, there are important changes in the dynamics sufficiently close to the bifurcation point when the terms involving Fr are retained in the equations. Second, the Küppers–Lortz dynamics does not set in as a direct transition from the base state to spatio-temporal complexity in finite systems. Instead, it is the result of a complex process involving cascades of bifurcations that take place in a very narrow parameter range. Third, even taking $Fr = 0$, these complex processes cannot be analyzed using reduced partial differential equations models, and direct numerical simulation of the Navier–Stokes–Boussinesq equations cannot be avoided. Incorporating $Fr \neq 0$, in which case reduced models cannot be derived, broadens the spectral gaps between the bifurcating modes and does allow for a bifurcation theoretic treatment. In the particular case we examined in detail in this paper, we find that as the Rayleigh number is increased, the axisymmetric large scale circulation smoothly evolves into an axisymmetric target

pattern which first becomes unstable at a Hopf bifurcation to an $m = 23$ rotating wave, which on further increasing Ra undergoes a secondary Hopf bifurcation to a modulated rotating wave with wavenumbers $m = 23$ and $m = 6$. The oscillations in this modulated rotating wave become increasingly non-uniform, displaying ratcheting characteristics and evolving towards Küppers–Lortz dynamics with further increases in Ra. So, in some sense, the $Fr \neq 0$ problem fits the familiar transition to temporal chaos following a small number of Hopf bifurcations (Ruelle & Takens, 1971), but for a spatio-temporal chaos involving symmetry-breaking Hopf bifurcations.

Chapter 6

Conclusions

There has long been a general interest in understanding the development of spatio-temporal complexity in dynamical systems and the means by which this complexity can be controlled. Rotating Rayleigh-Bénard convection has been of particular interest in this context as the additional complications arising from the rotational terms produce many nonintuitive phenomena, ranging from the unexpected emergence of wall-localized convection at onset in the higher rotation regime to the observation of spatio-temporal chaos seemingly immediately above onset in the case of more moderate rotation rates. The work in this thesis was motivated by a desire to understand phenomena that had yielded their substance to neither laboratory experiments nor theoretical treatments. To gain understanding into these flows a combination of direct numerical simulations and equivariant bifurcation analysis was used. Special focus was placed on understanding how large scale circulations brought forth by modulated rotation and centrifugal force change the nature of convective flows as the nonlinear nature of these large scale circulations makes the theoretical treatment of these flows intractable.

After discussing the history and several salient aspects of the rotating Rayleigh-Bénard problem in chapter 1 and describing our numerical methodology in chapter 2, the previously unexplained emergence of rotating waves in laboratory experiments of modulated rotating convection(Thompson *et al.*, 2002) is investigated. These results were published as Rubio *et al.* (2008). By use of direct numerical simulations in which axisymmetry was enforced it was possible to describe the structure of the oscillatory boundary layers and the development of axisymmetric convection from

the modulated basic state as a Z_2-breaking pitchfork bifurcation which results in two symmetry-related branches of solutions, differentiated by the presence of a hot or cold core. With increasing thermal driving these two branches merge via a SNIC (Saddle Node on an Invariant Circle) bifurcation leading to the radially inward travelling waves seen in the experiments. These quasiperiodic solutions live on a Z_2 reflection symmetric two-torii and their Poincaré sections are correspondingly on Z_2 reflection symmetric circles and thus the SNIC bifurcation is symmetry-restoring.

Chapter 4 continues the study of convection with modulated rotation now focusing on the simplest three-dimensional structures in rotating convection, the wall-modes that emerge at onset when the rate of rotation is sufficiently large. The effect of small amplitude harmonic modulation of the rotation rate over a wide range of frequencies was studied. For any non-zero modulation amplitude the modulated basic state evinced a large scale circulation driven by the modulated boundary layers. This circulation became particular pronounced at higher modulation frequencies for which acoustic streaming was observed, particularly in the azimuthal direction. When the thermal driving was sufficient for the wall-modes to manifest the azimuthal acoustic streaming had the effect of advecting the thermal plumes and changing their net precession from retrograde to prograde. More interestingly, it was found that over a broad band of frequencies modulations with amplitude of roughly 1% that of the background rotation were sufficient to quench the wall mode resulting in a return to a modulated basic state at thermal driving up to 18% beyond that necessary for wall mode convection in the non-modulated case. This wall-mode quenching is not a resonance-effect (Rand, 1982; Krupa, 1990) but rather a nonlinear interaction between the wall modes and the oscillatory boundary layers.

Chapter 5 concerns the onset of rotating convection in a parameter regime notable for the emergence of spatio-temporal complexity seemingly immediately at onset. A

program of laborious direct numerical simulations was carried out, each corresponding to a number of weeks of laboratory time, in order to study the behavior of the system very near onset after the very long transients had decayed. Two cases were considered, one neglecting centrifugal force (as is often done in theoretical models) and the other incorporating centrifugal force (as must necessarily be the case for laboratory experiments). It was found that in the $Fr = 0$ case a large packet of eigenvalues bifurcate in a very narrow range of parameters, the first ten in a range of $\epsilon = (Ra - Ra_c)/Ra_c$ of 2×10^{-4}. These bifurcated solutions saturate into states consisting of localized, slowly switching square patterns which bear no resemblance to any single bifurcated eigenmode. With increasing Ra these square patterns exhibit faster roll-switching which increasingly resembles Küppers-Lortz dynamics as ϵ increases beyond about 8×10^{-3}. When incorporating a small centrifugal force corresponding to that commonly found in laboratory experiments using water the dynamical picture is completely different. The quiescent basic state that exists when centrifugal force is neglected is replaced by an axisymmetric large scale circulation which develops into an axisymmetric target pattern as Ra approaches the critical value predicted by the infinite layer analysis (Chandrasekhar, 1961). In this case the spectral gap between the first two eigenmodes is more than three times that of the gap between the first ten in the case with $Fr = 0$, resulting in a saturated solution with the same structure as the eigenmode. This saturated solution further bifurcates to a hexagonal mixed-mode solution which exhibits a slow ratcheting behavior that had not been yet observed in rotating convection. With increasing ϵ this slowly ratcheting solution displays roll-switching behavior on a much faster time scale than the slow ratcheting. As ϵ nears 0.02 the ratcheting hexagonal lattice fades and a roll-switching solution with Küppers-Lortz-like dynamics is observed. However, the time average of the $Fr > 0$ roll-switching solution is an axisymmetric target pattern

with the same wave number and structure as that of the basic state just before the onset of three-dimensional convection. Similar results had been found in laboratory experiments for which time-averages of rotating convection near onset were taken although the resulting target patterns had been attributed to the geometry of the container. Reproducing numerically these results with and without centrifugal force it was shown that these findings were the result of the large scale circulation driven by centrifugal force coexisting with the convective rolls and that when centrifugal force is neglected the time averaged solutions corresponds to the quiescent $Fr = 0$ basic state.

Overall, the research presented in this thesis has settled several outstanding issues in rotating convection (the origin of travelling waves in modulated rotating convection, the development of Küppers-Lortz-like dynamics immediately above onset) and has presented several novel phenomenon not presented elsewhere (quenching of wall-localized convection via small amplitude modulations of the rotation rate, states exhibiting roll-switching within a ratcheting framework).

6.1 Future outlook

Having explored the nature of the spatio-temporal complexity found at the onset of convection effort is now focused on understanding rapidly rotating convection in the highly disordered regimes that eventually lead to hard thermal turbulence at thermal driving several hundred times that required for wall-mode convection. As before our approach is to use well-resolved direct numerical simulations of the full Navier-Stokes equations resulting in complex flows like those shown in figure 6.1. Pictured are isosurfaces of the temperature perturbation, Θ, and of helicity, $\mathbf{u} \cdot \omega$, where $\omega = \nabla \times \mathbf{u}$. Helicity is an important quantity in fluid dynamics since in the limit of zero viscosity it is conserved. In addition to characterizing helical structures

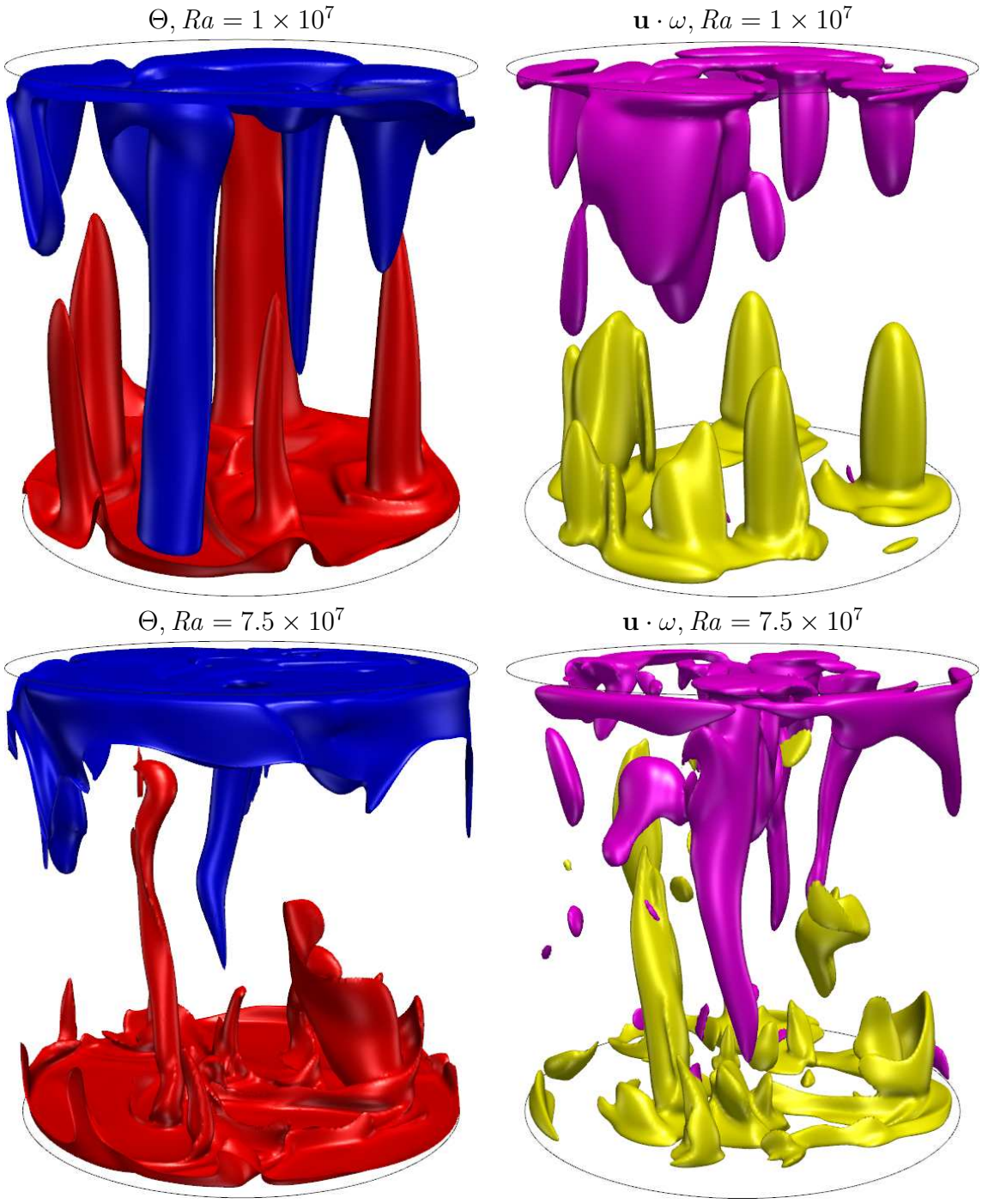

Figure 6.1: 3D renders of isosurfaces of the temperature perturbation, Θ, and helicity, $\mathbf{u} \cdot \omega$ for cases with given Ra, $\Omega = 4800$, $\sigma = 5.81$, $\gamma = 0.5$ and $Fr = 0$. $\Theta = \pm 0.15$ with the 0.15 isosurface is red and the -0.15 isosurface is blue. For $Ra = 1 \times 10^7$ the helicity isosurfaces are at 1.72×10^5 (yellow) and -1.72×10^5 (magenta). For $Ra = 7.5 \times 10^7$ are at 2.96×10^6 (yellow) and -2.96×10^6 (magenta).

helicity plays a key role in magnetohydrodynamics, small-scale intermittancy, TKE (turbulent kinetic energy) dissipation processes and the evolution of flow coherent structures. The role of helicity clearly changes with increasing thermal driving. In the figure it can be seen that at lower Ra the sign of helicity changes over the vertical extant columnar plumes, producing a picture not unlike the hexagonal planform of Veronis (1959). As the thermal driving is increased by a factor of 7.5 the correlation between the thermal perturbation and helicity has changed noticeably and the two fields are correlated over the entirety of the fluid layer. Our current research is in understanding the changing role of helicity with increased thermal driving and how the helicity affects the coherence of the plume structures in the regimes leading up to hard thermal turbulence.

BIBLIOGRAPHY

Abshagen, J., Lopez, J. M., Marques, F. & Pfister, G. 2005*a* Mode competition of rotating waves in reflection-symmetric Taylor-Couette flow. *J. Fluid Mech.* **540**, 269–299.

Abshagen, J., Lopez, J. M., Marques, F. & Pfister, G. 2005*b* Symmetry breaking via global bifurcations of modulated rotating waves in hydrodynamics. *Phys. Rev. Lett.* **94**, 074101.

Ahlers, G. 2006 Experiments with Rayleigh-Bénard convection. In *Dynamics of Spatio-Temporal Cellular Structures: Henri Bénard Centenary Review* (ed. I. Mutabazi, J. E. Wesfreid & E. Guyon), , vol. 207, pp. 67–94. Springer.

Avila, M., Belisle, M. J., Lopez, J. M., Marques, F. & Saric, W. S. 2008 Mode competition in modulated Taylor-Couette flow. *J. Fluid Mech.* **601**, 381–406.

Avila, M., Marques, F., Lopez, J. M. & Meseguer, A. 2007*a* Stability control and catastrophic transition in a forced Taylor–Couette system. *J. Fluid Mech.* **590**, 471–496.

Avila, M., Marques, F., Lopez, J. M. & Meseguer, A. 2007*b* Stability control and catastrophic transition in a forced Taylor-Couette system. *J. Fluid Mech.* **590**, 471–496.

Bajaj, K. M. S., Ahlers, G. & Pesch, W. 2002 Rayleigh-Bénrad convection with rotation at small Prandtl numbers. *Phys. Rev. E* **65**, 056309.

Bajaj, K. M. S., Liu, J., Naberhuis, B. & Ahlers, G. 1998 Square patterns in Rayleigh-Bénard convection with rotation about a vertical axis. *Phys. Rev. Lett.* **81**, 806–809.

Barcilon, V. & Pedlosky, J. 1967 On the steady motions produced by a stable stratification in a rapidly rotating fluid. *J. Fluid Mech.* **29**, 673–690.

Barkley, D., Tuckerman, L. S. & Golubitsky, M. 2000 Bifurcation theory for three-dimensional flow in the wake of a circular cylinder. *Phys. Rev. E* **61**, 5247–5252.

Batchelor, G. K. 1967 *An Introduction to Fluid Dynamics*. Cambridge University Press.

Becker, N. & Ahlers, G. 2006*a* Domain chaos puzzle and the calculation of the structure factor and its half-width. *Phys. Rev. E* **73**, 046209.

Becker, N. & Ahlers, G. 2006*b* Local wave director analysis of domain chaos in Rayleigh-Bénard convection. *J. Stat. Mech.* **2006**, P12002.

Becker, N., Scheel, J. D., Cross, M. C. & Ahlers, G. 2006 Effect of the centrifugal force on domain chaos in Rayleigh-Bénard convection. *Phys. Rev. E* **73**, 066309.

Bénard, H. 1900 Les tourbillons cellulaires dans une nappe liquide. *Rev. Gén. Sciences Pure Appl.* **11**, 1261–1271,1309–1328.

Bénard, H. 1901 Les tourbillons cellulaires dans une nappe liquide transportant de la chaleur par convection en régime permanent. *Ann. Chim. Phys.* **23**, 62–144.

Bhattacharjee, J. K. 1990 Convective instability in a rotating fluid layer under modulation of the rotating rate. *Phys. Rev. A* **41**, 5491–5494.

Bodenschatz, E., Cannell, D. S., de Bruyn, J. R., Ecke, R., Hu, Y.-C., Lerman, K. & Ahlers, G. 1992 Experiments on three systems with non-variational aspects. *Physica D* **61**, 77–93.

Bodenschatz, E., Pesch, W. & Ahlers, G. 2000 Recent developments in Rayleigh-Bénard convection. *Ann. Rev. Fluid Mech.* **32**, 709–778.

Boubnov, B. & Golitsyn, G. 1995 *Convection in Rotating Fluids*. Kluwer Academic Press.

Brummell, N., Hart, J. E. & Lopez, J. M. 2000 On the flow induced by centrifugal buoyancy in a differentially-heated rotating cylinder. *Theor. Comput. Fluid Dyn.* **14**, 39–54.

Chandrasekhar, S. 1961 *Hydrodynamic and Hydromagnetic Stability*. Oxford University Press.

Cox, S. M. & Matthews, P. C. 2000 Instability of rotating convection. *J. Fluid Mech.* **403**, 153–172.

Crawford, J. D. & Knobloch, E. 1991 Symmetry and symmetry-breaking bifurcations in fluid dynamics. *Ann. Rev. Fluid Mech.* **23**, 341–387.

Cross, M. C., Meiron, D. & Tu, Y. 1994 Chaotic domains: A numerical investigation. *Chaos* **4**, 607–619.

Daniels, P. G. 1980 The effect of centrifugal acceleration on axisymmetric convection in a shallow rotating cylinder or annulus. *J. Fluid Mech.* **99**, 65–84.

Davidson, P. A. 1989 The interaction between swirling and recirculating velocity components in unsteady, inviscid flow. *J. Fluid Mech.* **209**, 35–55.

Davis, S. H. 1976 The stability of time-periodic flows. *Ann. Rev. Fluid Mech.* **8**, 57–74.

Ecke, R. E., Zhong, F. & Knobloch, E. 1992 Hopf-bifurcation with broken reflection symmetry in rotating Rayleigh-Bénard convection. *Europhys. Lett.* **19**, 177–182.

Fantz, M., Friedrich, R., Bestehorn, M. & Haken, H. 1992 Pattern formation in rotating Bénard convection. *Physica D* **61**, 147–154.

Fornberg, B. 1998 *A Practical Guide to Pseudospectral Methods*. Cambridge University Press.

Goldstein, H. F., Knobloch, E., Mercader, I. & Net, M. 1993 Convection in a rotating cylinder. Part 1. Linear theory for moderate Prandtl numbers. *J. Fluid Mech.* **248**, 583–604.

Goldstein, H. F., Knobloch, E., Mercader, I. & Net, M. 1994 Convection in a rotating cylinder. Part 2. Linear theory for low Prandtl numbers. *J. Fluid Mech.* **262**, 293–324.

Golubitsky, M., LeBlanc, V. G. & Melbourne, I. 2000 Hopf bifurcation from rotating waves and patterns in physical space. *J. Nonlinear Sci.* **10**, 69–101.

Gorman, M., el Hamdi, M., Pearson, B. & Robbins, K. A. 1996 Ratcheting motion of concentric rings in cellular flames. *Phys. Rev. Lett.* **76**, 228–231.

Gresho, P. & Sani, R. 1987 On pressure boundary conditions for the incompressible navier–stokes equations. *IJNMF* **7**, 1111–1145.

Hart, J. E. 2000 On the influence of centrifugal buoyancy on rotating convection. *J. Fluid Mech.* **403**, 133–151.

Heikes, K. E. & Busse, F. H. 1980*a* Convection in a rotating layer: A simple case of turbulence. *Science* **208**, 173–175.

Heikes, K. E. & Busse, F. H. 1980*b* Weakly nonlinear turbulence in a rotating convection layer. *Annals N. Y. Acad. Sci.* **357**, 28–36.

Herrmann, J. & Busse, F. H. 1993 Asymptotic theory of wall-attached convection in a rotating fluid layer. *J. Fluid Mech.* **255**, 183–194.

Homsy, G. M. & Hudson, J. L. 1969 Centrifugally driven thermal convection in a rotating cylinder. *J. Fluid Mech.* **35**, 33–52.

Homsy, G. M. & Hudson, J. L. 1971 Centrifugal convection and its effect on the asymptotic stability of a bounded rotating fluid heated from below. *J. Fluid Mech.* **48**, 605–624.

Hu, Y., Ecke, R. E. & Ahlers, G. 1997 Convection under rotation for Prandtl numbers near 1: Linear stability, wave-number selection, and pattern dynamics. *Phys. Rev. E* **55**, 6928–6949.

Hu, Y., Pesch, W., Ahlers, G. & Ecke, R. E. 1998 Convection under rotation for Prandtl numbers near 1: Küppers-Lortz instability. *Phys. Rev. E* **58**, 5821–5833.

Hughes, S. & Randriamampianina, A. 1998 An improved projection scheme applied to pseudospectral methods for the incompressible Navier-Stokes equations. *Int. J. Numer. Meth. Fluids* **28**, 501–521.

Ingersoll, A. & Pollard, D. 1982 Motion in the interiors and atmospheres of Jupiter and Saturn: scale analysis, anelastic equations, barotropic stability criterion. *Icarus* **52**, 62–80.

Jayaraman, A., Scheel, J. D., Greenside, H. S. & Fisher, P. F. 2006 Characterization of the domain chaos convection state by the largest Lyapunov exponent. *Phys. Rev. E* **74**, 016209.

Jeffreys, H. 1926 The stability of a layer of fluid heated from below. *Phil. Mag.* **2**, 833–844.

Jeffreys, H. 1928 Some cases of instability in fluid motion. *PRSA* **118**, 195–208.

Kerczek, C. v. & Davis, S. H. 1974 Linear stability theory of oscillatory Stokes layers. *J. Fluid Mech.* **62**, 753–773.

Knobloch, E. 1994 Bifurcations in rotating systems. In *Lectures on Solar and Planetary Dynamos* (ed. M. R. E. Proctor & A. D. Gilbert), pp. 331–372. Cambridge University Press.

Knobloch, E. 1996 Symmetry and instability in rotating hydrodynamic and magnetohydrodynamic flows. *Phys. Fluids* **8**, 1446–1454.

Knobloch, E. 1998 Rotating convection: Recent developments. *Int. J. Eng. Sci.* **36**, 1421–1450.

Koschmieder, E. L. 1967 On convection on a uniformly heated rotating plane. *Beitr. Physik. Atmos.* **40**, 216–225.

Koschmieder, E. L. 1993 *Bénard Cells and Taylor Vortices*. Cambridge University Press.

Krupa, M. 1990 Bifurcations of relative equilibria. *SIAM J. Math. Anal.* **21**, 1453–1486.

Kuo, E. Y. & Cross, M. C. 1993 Traveling-wave wall states in rotating Rayleigh-Bénard convection. *Phys. Rev. E* **47**, R2245–R2248.

Küppers, G. 1970 The stability of steady finite amplitude convection in a rotating fluid layer. *Phys. Lett. A* **32**, 7–8.

Küppers, G. & Lortz, D. 1969 Transition from laminar convection to thermal turbulence in a rotating fluid layer. *J. Fluid Mech.* **35**, 609–620.

Kuznetsov, Y. A. 2004 *Elements of Applied Bifurcation Theory*, 3rd edn. Springer.

Lewis, G. M. & Nagata, W. 2003 Double Hopf bifurcations in the differentially heated rotating annulus. *SIAM J. Appl. Math.* **63**, 1029–1055.

Lopez, J. M. 1995 Unsteady swirling flow in an enclosed cylinder with reflectional symmetry. *Phys. Fluids* **7**, 2700–2714.

Lopez, J. M., Cui, Y. D. & Lim, T. T. 2006*a* An experimental and numerical investigation of the competition between axisymmetric time-periodic modes in an enclosed swirling flow. *Phys. Fluids* **18**, 104106.

Lopez, J. M., Cui, Y. D., Marques, F. & Lim, T. T. 2008 Quenching of vortex breakdown oscillations via harmonic modulation. *J. Fluid Mech.* **599**, 441–464.

Lopez, J. M. & Marques, F. 2004 Mode competition between rotating waves in a swirling flow with reflection symmetry. *J. Fluid Mech.* **507**, 265–288.

Lopez, J. M. & Marques, F. 2009 Centrifugal effects in rotating convection: nonlinear dynamics. *J. Fluid Mech.* **628**, 269–297.

Lopez, J. M., Marques, F., Mercader, I. & Batiste, O. 2007 Onset of convection in a moderate aspect-ratio rotating cylinder: Eckhaus-Benjamin-Feir instability. *J. Fluid Mech.* **590**, 187–208.

Lopez, J. M., Rubio, A. & Marques, F. 2006*b* Traveling circular waves in axisymmetric rotating convection. *J. Fluid Mech.* **569**, 331–348.

Low, A. 1929 On the criterion for stability of a layer of viscous fluid heated from below. *PRSA* **125**, 180–195.

Marques, F., Gelfgat, A. Y. & Lopez, J. M. 2003 A tangent double Hopf bifurcation in a differentially rotating cylinder flow. *Phys. Rev. E* **68**, 016310.

Marques, F. & Lopez, J. M. 1997 Taylor-Couette flow with axial oscillations of the inner cylinder: Floquet analysis of the basic flow. *J. Fluid Mech.* **348**, 153–175.

Marques, F. & Lopez, J. M. 2000 Spatial and temporal resonances in a periodically forced extended system. *Physica D* **136**, 340–352.

Marques, F. & Lopez, J. M. 2008 Influence of wall modes on the onset of bulk convection in a rotating cylinder. *Phys. Fluids* **20**, 024109.

Marques, F., Lopez, J. M. & Shen, J. 2002 Mode interactions in an enclosed swirling flow: a double Hopf bifurcation between azimuthal wavenumbers 0 and 2. *J. Fluid Mech.* **455**, 263–281.

Marques, F., Mercader, I., Batiste, O. & Lopez, J. M. 2007 Centrifugal effects in rotating convection: axisymmetric states and three-dimensional instabilities. *J. Fluid Mech.* **580**, 303–318.

Mercader, I., Net, M. & Falqués, A. 1991 Spectral methods for high order equations. *Comp. Meth. Appl. Mech. & Engng* **91**, 1245–1251.

Niemela, J. J. & Donnelly, R. J. 1986 Direct transition to turbulence in rotating Bénard convection. *Phys. Rev. Lett.* **57**, 2524–2527.

Niemela, J. J., Smith, M. R. & Donnelly, R. J. 1991 Convective instability with time-varying rotation. *Phys. Rev. A.* **44**, 8406–8409.

Ning, L., Hu, Y., Ecke, R. & Ahlers, G. 1993 Spatial and temporal averages in chaotic patterns. *Phys. Rev. Lett.* **71**, 2216–2219.

Orszag, S. A. & Patera, A. T. 1983 Secondary instability of wall-bounded shear flows. *J. Fluid Mech.* **128**, 347–385.

Pellew, A. & Southwell, R. 1940 On maintained convective motions in a fluid heated from below. *PRSA* **176**, 312–343.

Ponty, Y., Passot, T. & Sulem, P. L. 1997 Pattern dynamics in rotating convection at finite Prandtl number. *Phys. Rev. E* **56**, 4162–4178.

Proudman, J. 1916 On the motion of solids in a liquid possessing vorticity. *PRSA* **92**, 408–424.

Rand, D. 1982 Dynamics and symmetry. Predictions for modulated waves in rotating fluids. *Arch. Ration. Mech. An.* **79**, 1–37.

Rayleigh, L. 1916 On convection currents in a horizontal fluid layer of fluid when the higher temperature is on the under side. *Phil. Mag.* **32**, 529–546.

Rhines, P. 1986 Vorticity dynamics of the oceanic general circulation. *Ann. Rev. Fluid Mech.* **18**, 433–497.

Riley, N. 2001 Steady streaming. *Ann. Rev. Fluid Mech.* **33**, 43–65.

Rodríguez, J. M., Pérez-García, C., Bestehorn, M., Fantz, M. & Friedrich, R. 1992 Pattern formation in convection of rotating fluids with broken vertical symmetry. *Phys. Rev. A* **46**, 4729–4735.

Roppo, M. N., Davis, S. H. & Rosenblat, S. 1984 Bénard convection with time-periodic heating. *Phys. Fluids* **27**, 796–803.

Rossby, H. T. 1969 A study of Benard convection with and without rotation. *J. Fluid Mech.* **36**, 309–335.

Roxin, A. & Riecke, H. 2002 Rotating convection in an anisotropic system. *Phys. Rev. E* **65**, 046219.

Rubio, A., Lopez, J. M. & Marques, F. 2008 Modulated rotating convection: radially traveling concentric rolls. *J. Fluid Mech.* **608**, 357–378.

Rubio, A., Lopez, J. M. & Marques, F. 2009*a* Interacting oscillatory boundary layers and wall modes in modulated rotating convection. *J. Fluid Mech.* **625**, 75–96.

Rubio, A., Lopez, J. M. & Marques, F. 2009*b* Onset of küppers-lortz-like dynamics in finite rotating convection. *J. Fluid Mech.* Submitted.

Ruelle, D. & Takens, F. 1971 On the nature of turbulence. *Commun. Math. Phys.* **20**, 167.

Sánchez-Álvarez, J. J., Serre, E., Crespo del Arco, E. & Busse, F. H. 2005 Square patterns in rotating Rayleigh-Bénard convection. *Phys. Rev. E* **72**, 036307.

Scheel, J. D. 2007 The amplitude equation for rotating Rayleigh-Bénard convection. *Phys. Fluids* **19**, 104105.

Scheel, J. D. & Cross, M. C. 2005 Scaling laws for rotating Rayleigh-Bénard convection. *Phys. Rev. E* **72**, 056315.

Schlichting, H. 1932 Berechnung ebener periodischer Grenzschichtströmungen. *Phys. Z.* **33**, 327–335.

Schmidt, R. & Milverton, S. 1935 On the instability of a fluid when heated from below. *PRSA* **152**, 586–594.

Sinha, M., Kevrekidis, I. G. & Smits, A. J. 2006 Experimental study of a neimark sacker bifurcation in axially forced taylor couette flow. *J. Fluid Mech.* **558**, 1–32.

Stokes, G. G. 1851 On the effect of the internal friction of fluids on the motion of pendulums. *Trans. Camb. Phil. Soc.* **9**, 8.

Taylor, G. 1917 Motion of solids in fluids when the flow is not irrotational. *PRSA* **93**, 99–113.

Taylor, G. 1922 The motion of a sphere in a rotating fluid. *PRSA* **102**, 180–189.

Taylor, G. 1923 Experiments on the motion of solid bodies in rotating fluids. *PRSA* **104**, 213–228.

Thompson, K. L., Bajaj, K. M. S. & Ahlers, G. 2002 Traveling concentric-roll patterns in Rayleigh-Bénard convection with modulated rotation. *Phys. Rev. E* **65**, 04618.

Torrest, M. A. & Hudson, J. L. 1974 The effect of centrifugal convection on the stability of a rotating fluid heated from below. *Appl. Sci. Res.* **29**, 273–289.

Tu, Y. & Cross, M. C. 1992 Chaotic domain structure in rotating convection. *Phys. Rev. Lett.* **69**, 2515–2518.

Tuckerman, L. S. & Barkley, D. 1988 Global bifurcation to traveling waves in axisymmetric convection. *Phys. Rev. Lett.* **61**, 408–411.

Veronis, G. 1959 Cellular convection with finite amplitude in a rotating fluid. *J. Fluid Mech.* **5**, 401–435.

Weisberg, A. Y., Kevrekidis, I. G. & Smits, A. J. 1997 Delaying transition in Taylor–Couette flow with axial motion of the inner cylinder. *J. Fluid Mech.* **348**, 141–151.

Yih, C.-S. 1977 *Fluid Mechanics*. West River Press: Ann Arbor, Michigan.

Zhong, F., Ecke, R. E. & Steinberg, V. 1991 Asymmetric modes and the transition to vortex structures in rotating Rayleigh-Bénard convection. *Phys. Rev. Lett.* **67**, 2473–2476.

Zurbuchen, T. 2007 A new view of the coupling of the Sun and heliosphere. *Ann. Rev. Astronomy & Astrophys.* **45**, 297–338.